

1
NASA Technical Memorandum 74045

DO NOT DESTROY
RETURN TO LIBRARY

74045
NASA-179-14045

Heat Transfer Distributions Induced by Elevon Deflections on Swept Wings and Adjacent Surfaces at Mach 6

Charles B. Johnson and Louis G. Kaufman II

AUGUST 1978

31 AUG 1978
MCDONNELL DOUGLAS
RESEARCH & ENGINEERING LIBRARY
ST. LOUIS

NASA

M 78-16559

NASA Technical Memorandum 74045

Heat Transfer Distributions Induced by Elevon Deflections on Swept Wings and Adjacent Surfaces at Mach 6

Charles B. Johnson
Langley Research Center
Hampton, Virginia

and

Louis G. Kaufman II
Grumman Aerospace Corporation
Bethpage, New York



National Aeronautics
and Space Administration

**Scientific and Technical
Information Office**

1978

SUMMARY

Surface heat transfer distributions are presented for regions where three-dimensional separated flow effects are prominent on a model representative of a fuselage-wing-elevon portion of a hypersonic aircraft. The basic model is composed of a sharp leading-edge flat-plate wing (0° , 50° , or 70° sweepback) with a trailing-edge elevon (0° , 10° , 20° , or 30° ramps). The model has attachable center bodies and tip fins. Data were obtained using the phase change coating (paint) technique in the Langley 20-inch Mach 6 tunnel for a free-stream Reynolds number of about 17×10^6 based on the wing root chord. The data reveal considerably larger regions of elevon-induced thermal loads on adjacent surfaces than would be suggested by standard strip, boundary-layer analyses. For comparable flow conditions, the data may be used to guide analyses of wing sweep, elevon deflection angle, center body, and tip fin effects on portions of hypersonic aircraft similar to the wing-elevon model used in this experiment.

INTRODUCTION

Thermal loads on the surfaces of high speed aircraft can be altered greatly when shock waves impinge on the boundary-layer flows on these surfaces. Such interaction frequently causes boundary-layer separation. The resulting surface heat transfer distributions are far different from those anticipated if the viscous interaction between the shock wave and the boundary layer does not occur. These interactions are widely recognized as an important problem area in the design of high speed aircraft and have prompted many investigations of shock-induced separated flows (refs. 1 and 2). The investigations have resulted in an understanding of some features of two-dimensional separated flows, but there are still many unanswered questions pertaining to three-dimensional flow separation (ref. 3). The problem has eluded theoretical solutions because of its complexity, but because of its great practical importance, it has attracted considerable attention (refs. 1 to 4). An improved understanding of three-dimensional flow separation is needed for the efficient design of high speed vehicles such as the space shuttle and advanced supersonic transports.

The particular problem addressed by this report is flow separation caused by elevon deflections on high speed aircraft. Even small elevon deflections cause shock waves that can impinge on adjacent fuselage and tip fin surfaces. The interaction of the shock wave with the boundary layers on these surfaces can result in extensive regions of separated flow and induce substantial pressure and thermal loads on the surfaces (refs. 3, 5, and 6). These increased loads can compromise an aircraft design. Although these effects are of vital importance to high speed aircraft design, there are very few experimental data of general applicability to three-dimensional separated flows and no satisfactory analytical methods for predicting the interaction effects (refs. 7 to 9).

The character of the boundary layer is one of the most important factors influencing interactions between the shock wave and the boundary layer (ref. 10).

Wind tunnel models of complete configurations frequently have laminar or transitional boundary layers unlike the actual flight configurations which have predominately turbulent boundary-layer flows over their surfaces. This discrepancy, caused by the limitations of hypersonic wind tunnels on model size, makes questionable the validity of extrapolating small scale model data to full scale flight vehicles.

An experimental program was designed to obtain much needed empirical data applicable to elevon-induced separation on high speed vehicles. Instead of a complete configuration, a simple "wing-elevon" model was used to simulate the wing and aft fuselage portion of a "typical" hypersonic vehicle. (See fig. 1 and refs. 11 to 14.) The chord of the semispan wing-elevon model could be made several times larger than the wing chord for a model of a complete configuration (for the same wind tunnel). Thus, more detailed data could be obtained in the interaction flow region. Further, chord length Reynolds numbers comparable to those anticipated for flight vehicles could be achieved, so the boundary layer would be predominately turbulent, similar to that on the flight vehicle.

Fundamental shapes (flat plate and cylindrical surfaces) were chosen to make the data as generally applicable as possible and to increase the usefulness of the data in guiding theoretical analyses of interaction flow regions with a minimum of extraneous effects. Sharp leading-edge flat-plate wings with leading-edge sweep angles of 0° , 50° , and 70° were tested at a 0° angle of attack. Regions of boundary-layer transition on these wings are parallel to the sharp leading edges (ref. 15). For the 70° swept wing, the boundary layer at the elevon hinge line location will be turbulent on the inboard portion of the wing (near the root chord) and transitional or laminar on the outboard portion (near the wing tip) (refs. 16 and 17). Because the character of the boundary layer strongly affects flow separation (ref. 10), wing sweep effects can strongly influence separation ahead of an elevon. In addition to wing sweep and elevon deflection angle effects, attachable inboard bodies and tip fins were used to provide data for determining the effects of adjacent fuselage surfaces and tip fins on the heat transfer distributions.

Experiments were conducted in the Langley 20-inch Mach 6 tunnel for root chord Reynolds numbers of approximately 17×10^6 . Pressure and heat transfer distributions, as well as oil flow and schlieren photographic data, were obtained for many model configurations. The pressure distributions and photographic data obtained using the pressure instrumented model are presented in reference 18. The heat transfer distributions and pertinent photographic data are presented in this paper.

SYMBOLS

All values are given in SI units with the exception of table I where both SI and U.S. Customary Units are given. Measurements were made in U.S. Customary Units.

c	specific heat capacity of silicone rubber portions of model, J/kg-K
g	width of gap between end plate and inboard edge of elevon, cm (fig. 2)
H.L.	hinge line
h	heat transfer coefficient, W/m ² -K
k	thermal conductivity of silicone rubber portions of model, W/m-K
M	Mach number
p	pressure, Pa
R _C	Reynolds number based on free-stream conditions and length (64.14 cm) of wing root chord
T	temperature, K
t	time, sec
x	streamwise distance measured along surface of wing and elevon from wing apex (wing leading edge for unswept wing), cm (fig. 2) (X in figures)
y	spanwise distance measured outboard from inboard edge of the elevon, cm (fig. 2) (Y in figures)
z	distance measured on end plate upward from wing surface, cm (fig. 2) (Z in figures)
ε	elevon deflection angle, deg
Λ	wing sweep angle, deg
ρ	density of silicone rubber portions of model, kg/m ³

Subscripts:

aw	adiabatic wall
i	initial
pc	phase change of paint coating
t	stagnation conditions of free-stream tunnel flow
∞	free-stream flow conditions

EXPERIMENTAL PROCEDURES

Model

Outlines of a typical hypersonic flight configuration and the wing-elevon model used for the subject tests are sketched in figure 1. The semispan model is designed to simulate the aft fuselage and wing portion of the flight configuration. Flat plate wings with machined-sharp leading edges swept 0° , 50° , and 70° were fabricated (fig. 2). The wings have a partial span trailing-edge elevon that can be set at 0° , 10° , 20° , or 30° (flow compression) deflection angles. The elevon is sealed to the wing surface to prevent any air flow between the wing and elevon.

The model has an end plate (shown in fig. 2) and a cylindrical body (fig. 3) that can be attached to the inboard (root) portions of the wings to simulate an aft fuselage section. Thus, data may be obtained in the absence of inboard body effects simulating the lower wing surface of the flight configuration outlined in figure 1. Alternatively, data may be obtained with effective inboard end plating simulating the upper wing surface, by attaching either the end plate or cylindrical body to the wing.

The model also has tip fins and plates (fig. 4) that can be attached to the outboard portions of the wings. There are both large and small tip fins and plates simulating those on the upper and lower wing surfaces of the flight configuration outlined in figure 1. The tip fins are toed-in whereas the tip plates are aligned with the free-stream flow direction. When either the large or the small tip plate is attached to the wing surface, the tip plate is sealed to the elevon to prevent air flow between the tip plate and elevon.

To make investigations of the effects of air flow between an elevon and aft fuselage section possible, the end plate is attachable in different spanwise positions on the inboard portions of the wings. The resulting gaps between the elevon and end plate can be varied from 0 (end plate sealed to elevon) to 1.27 cm (fig. 2).

A photograph of one of the wing-elevon model configurations is shown in figure 5. The cylindrical body and large tip fin are attached to the 70° wing, and the elevon is deflected 20° . As indicated by the dotted lines in figures 2 and 3 and evidenced in figure 5 by the lighter areas, the aft portions of the model (in the vicinity of the elevon) are comprised of 0.64-cm-thick inserts of silicone rubber. The inserts on the fins, plates, body, wing, and elevon encompass the interaction flow region and are composed of a nonconductive material ideal for the use of the phase change paint technique (refs. 19 to 23) for obtaining heat transfer data.

Apparatus and Test Conditions

The experiments were conducted in the Langley 20-inch Mach 6 tunnel, a blowdown wind tunnel with a square test section (see appendix of ref. 24). The model configurations were strut-mounted to an injection system located beneath the tunnel test section. Nominal values of the tunnel flow stagnation pressure

and temperature used for these experiments are shown in table I together with the free-stream pressure, free-stream Mach number, and free-stream Reynolds number based on the wing root chord of 64.14 cm.

TABLE I.- TUNNEL FLOW CONDITIONS

P_t , Pa (psia) 3 562 000 (517)
P_∞ , Pa (psia) 2256 (0.327)
T_t , K ($^{\circ}$ R) 537 (967)
M_∞ 6
R_C 17.41×10^6

Motion-picture cameras were mounted next to viewing ports above and on one side of the test section in order to provide planform and profile motion pictures of the oil flow and progression of the region of melted paint on the model. The cameras use 35-mm film and, for these experiments, were set to take "double frames" at the rate of 10 per sec.

The model configurations tested are indicated in table II. The wing sweep angle is Λ and the elevon deflection angle is ϵ . "Inboard" refers to the root chord portion of the wing; "outboard" refers to the wing tip region. As table II indicates, the tip fins and the cylindrical body (figs. 3 to 5) were attached only to the 70° wing.

TABLE II.- MODEL CONFIGURATIONS

[$\epsilon = 0^\circ, 10^\circ, 20^\circ$, and 30° for all configurations]

Λ , deg	Inboard attachment	Outboard attachments
0	None End plate	None, small tip plate, large tip plate None, ^a large tip plate
50	None End plate	None None
70	None End plate Cylinder	None, small tip plate, small tip fin None, ^a large tip plate ^a None, large tip plate, large tip fin

^aDifferent end plate - elevon gap sizes for these configurations.

Test Procedures and Data Reduction

The oil flow technique was used to ascertain the surface flow pattern. The model surfaces were prerubbed with silicone oil (Dow Corning Fluid 550). A random pattern of oil drops of varying sizes was then splattered on the model surfaces using a mixture of 10 ml of the same oil, 10 ml of titanium dioxide, and 1 ml of oleic acid. The model was injected into the established tunnel flow, the oil flow was observed with a TV camera, and top and side motion pictures of the oil flow were taken until the flow pattern was firmly established and there was no further apparent oil droplet movement.

Aerodynamic heat transfer coefficient distributions were obtained by the phase change coating (paint) technique described in reference 19. This technique provides continuous heat transfer coefficient distributions over the model surfaces and does not require instrumented models. A thin coating of a paint that changes phase (melts) at a known temperature is sprayed on the model. The model is then injected into the tunnel flow. The model surface temperature rises as a result of aerodynamic heating, and the coating melts on portions of the surface when the phase change temperature is attained. Photographing the model with motion-picture cameras at a known framing rate determines the location of the phase change line as a function of time; this information permits the local heat transfer coefficient to be computed (refs. 19 and 20).

Sample frames from the planform and profile motion pictures showing the regression of the phase change coating are shown in figure 6 for the 70° wing with the cylindrical body, 30° elevon, and large tip fin. The regions of melted paint are delineated by dashed lines to aid interpretation of the films. In interpreting such films, care must be taken to distinguish between shadows (such as the one cast by the tip fin on the wing surface) and regions of melted paint. The forward portion of the cylindrical body is steel; this portion is well upstream of the region of interest (figs. 3 and 6(b)).

A general form of the solution of the transient one-dimensional heat conduction equation may be expressed as

$$\frac{h\sqrt{t_{pc}}}{\sqrt{\rho ck}} = f\left(\frac{T_{pc} - T_i}{T_{aw} - T_i}\right) \quad (1)$$

where t_{pc} is the time at which the phase change occurs, ρck is the product of thermophysical properties of the model surface material, and f is a transcendental function of the phase change temperature T_{pc} , the surface initial temperature T_i , and the adiabatic wall temperature T_{aw} . The function f has been plotted by Jones and Hunt and is available in reference 19.

In order to obtain reliable values of h using this technique, the phase change time t_{pc} should be large compared with the model injection time and small compared with the thermal diffusion time of the model material. The second criterion was met during all of the subject test runs. However, because

of very high local heating rates, local melting of the paint frequently occurred before the model reached the tunnel flow center line (0.3 sec is required for the model to pass through the tunnel wall shear flow and reach the center line). In these cases, the phase change paint technique is valuable for ascertaining the precise location of high local heating rates, but the uncertainty in the quantitative value calculated for h may be as large as 30 percent. (See ref. 23.) For model exposure times of 1 sec or more, the uncertainty in the value of h associated with the error in t_{pc} is less than 5 percent. The great majority of the data presented herein are for exposure times considerably larger than 1 sec. The variation of $\sqrt{\rho ck}$ for silicone rubber material with a surface temperature taken as equal to T_{pc} is plotted in figure 7 (calculated by a method described in ref. 25) for an initial model surface temperature of 296 K. The dependence of $\sqrt{\rho ck}$ on T_{pc} varies slightly with T_i for the silicone rubber. Although small, this variation was included in the reduction of the data presented in this paper.

For accurate values of h , small values of T_i/T_{aw} are also desirable. The adiabatic wall temperature values used in this paper are calculated using a turbulent recovery factor, $0.72^{1/3}$. Oblique shock relations (ref. 26) are used to calculate the inviscid-flow static temperature rise across the elevon-generated shock wave. Values of T_{aw}/T_t , calculated in this manner, are listed in table III. The large running length Reynolds numbers, except near the out-board tip of the 70° wing, justify the assumption of turbulent boundary-layer flow over most of the region of interest. More thorough discussions of the uncertainties inherent in the phase change coating technique are available in references 19 to 23. The wing elevon model was designed to minimize these uncertainties and avoid the need for corrections to the values of h calculated from the data (ref. 22).

TABLE III.- T_{aw}/T_t VALUES

[$T_{aw}/T_t = 0.9089$ on all wing surfaces and on end plate surface upstream of elevon-generated shock wave]

Elevon deflection angle, ϵ , deg	Value of T_{aw}/T_t on elevon surface and on portion of end plate surface downstream of elevon-generated shock wave
0	0.9089
10	.9158
20	.9279
30	.9459

Model surfaces aligned with the free-stream direction are covered with one phase change temperature paint. Because of the higher heating rates anticipated on the elevon surface, higher temperature phase change paints are used to cover

the elevon surface. Strip recorders were used to record the tunnel flow stagnation pressure and temperature during each run. These values remain essentially constant during a run.

PRESENTATION OF EXPERIMENTAL RESULTS

Tracings of melt lines from many motion-picture frames of the phase change coating on a configuration are superimposed to obtain contours of equal and constant heat transfer coefficients for the configuration. Sample tracings for the unswept wing configuration with no elevon deflection are shown in figure 8. For no elevon deflection, the heating varies only slightly over the aft portion of the flat plate surface. The very small gradients in the surface heating lead to considerable uncertainty in the location of a constant heat transfer coefficient contour, and the jagged contours in figure 8(a) are thus produced. A comparison of motion pictures from different tunnel runs shows the variations in the melt lines to be random and not a function of tunnel flow conditions or initial model temperature. The variations in melt lines are attributed to minute variations in the thickness of the thin coat of paint sprayed on the model. A more realistic and usable presentation of the results, particularly for cases of small heat transfer coefficient gradients, is obtained by fairing smooth lines through the observed jagged melt lines (fig. 8(b)). These experimental values of heat transfer coefficient are compared in figure 9 with theoretical predictions calculated using (1) the methods of Anderson and Lewis (ref. 27), (2) that of Harris (ref. 28), and (3) the Van Driest II method (Hopkins, et al., ref. 29). The Van Driest II method for calculating skin friction is used in the integral method of reference 30 to obtain local heat transfer coefficients. The Anderson and Lewis method gives results that agree with the upstream portion of the data, but are about 12 percent above the data near the trailing edge of the plate. The Van Driest II method indicates good agreement with the downstream portion of the data, but falls below the upstream portion of the data. Harris' method (ref. 28) falls between the other two methods and agrees best with the data.

Major changes in the heat transfer distributions on the wing, elevon, and inboard body surfaces are caused primarily by different elevon deflections. Results for undeflected elevons are presented first in the following discussion; results for 10° , 20° , and 30° elevon deflections are then presented. Effects of wing sweep and different inboard and outboard attachments are described for each elevon deflection angle. For each elevon deflection angle, results on the wing and elevon surfaces are presented before showing results on the end plate or cylindrical body surfaces. The data presented for various model configurations are indicated in table IV. Sample frames of the oil flow and phase change coating motion pictures are presented only for selected configurations. Results based on examination of the motion pictures for all of the configurations are included in the discussion of the experimental results in the following section. Constant heat transfer coefficient contours, hereafter referred to simply as "contours," are presented for all configurations for which they were obtained.

TABLE IV.- DATA PRESENTED FOR VARIOUS MODEL CONFIGURATIONS

ϵ , deg	Λ , deg	Attachments to wing	Figure numbers for -		
			Sample oil flow and phase change coating photographs	Heat transfer contours on wing and elevon surfaces	Heat transfer contours on end plate and cylindrical body surfaces
0	0	None		8	
		Large tip plate		8	
		End plate		8	14
		End plate and large tip plate		8	14
	50	None		10	
		End plate		10	14
	70	None		11	
		Small tip plate		11	
		Small tip fin		11	
		End plate		11	14
		End plate and large tip plate	13	11	14
		Cylinder		12	17
		Cylinder and large tip fin	15, 16	12	17
10	0	None		18	
		Large tip plate		18	
		End plate		19	29
		End plate and large tip plate		20	29
		End plate with gap		18	30
	50	None		21	
		End plate		22	29
	70	None		23	
		Small tip plate		23	
		Small tip fin		24	
		End plate		25	29
		End plate and large tip plate	28	26	29
		End plate with gap and large tip plate		26	30
		Cylinder		27	32
		Cylinder and large tip fin	31	27	32
20	0	None		33	
		Small tip plate		33	
		Large tip plate		33	
		End plate		33	43
		End plate and large tip plate	41	33	43
		End plate with gap		33	44
	50	None		34	
		End plate	42	34	43
	70	None		35	
		Small tip plate		35	
		Small tip fin		36	
		End plate		38	43
		End plate and large tip plate		38	43
		End plate with gap		37	44
		End plate with gap and large tip plate		37	44
		Cylinder		39	45
	30	Cylinder and large tip plate		40	45
		Cylinder and large tip fin		40	45
30	0	None	46	47	
		Small tip plate		47	
		Large tip plate		47	
		End plate	49, 70	51	73
		End plate and large tip plate	50, 71	51	73
		End plate with gap	75	48, 51	74, 77, 78, 79
	50	None		52	
		End plate	53, 72	54	73
	70	None	55	56	
		Small tip plate		58	
		Small tip fin	57	58	
		End plate	59	61	73
		End plate and large tip plate	63	64	73
		End plate with gap	60, 76	61	77
		End plate with gap and large tip plate		62	74, 77, 78, 79
		Cylinder	65	69	81
		Cylinder and small tip fin	66		
		Cylinder and large tip plate	68	69	81
		Cylinder and large tip fin	67, 80	69	81

Notice from table IV that contours for several different configurations are frequently presented in one figure. This indicates that the contours for those configurations were all essentially the same. For example, if the contours on the wing and elevon surfaces are the same whether or not a tip plate is attached to the wing, then the contours are shown in the same figure, and the location of the attachable tip plate is indicated by dashed lines. For contours on the elevon surface, the true view of the elevon surface is always shown instead of projecting the deflected elevon surface onto the plane of the wing. The projection of the elevon surface on the end plate and cylindrical body surfaces is indicated. In certain instances, the words "hot" and/or "cold" are shown on the contour plots to indicate regions of relatively high heating and relatively low heating.

Elevon Deflection Angle of 0°

Contours on the unswept wing and undeflected elevon surfaces are shown in figure 8. The contours are essentially the same whether or not the large tip plate and/or the end plate are attached to the wing. The contours for the 50° and 70° swept wings parallel the wing leading edge on the outboard portions of the wings and are not affected substantially by either the end plate or the various wing tip attachments (figs. 10 and 11). When the cylindrical body is attached to the 70° wing, a hot streak occurs on the wing and elevon near the body (fig. 12). The addition of the large tip fin does not materially change the contours. On the outboard portion of the wing, the heating distribution is similar to that for the 70° wing without the cylindrical body.

Oil flow on the end plate surface (fig. 13) indicates the streamwise nature of the flow on the silicone rubber portion of the surface. Contours on the end plate surface parallel the 70° swept leading edge of the end plate and are essentially unaffected by either wing sweep or the large tip plate attachments (fig. 14). The oil flow on the cylindrical body surface accumulates along the tangency line between the cylindrical and planar portions of the body (fig. 15). However, the heating contours on the silicone rubber portion of the cylindrical body parallel the body ridge line, which is similar to the blunt leading edge of a highly swept wing (figs. 16 and 17). The contours on the body surface are not affected by the addition of a tip fin.

Elevon Deflection Angle of 10°

Contours of equal heat transfer coefficient values on the unswept wing and 10° elevon surfaces are presented in figures 18 to 20. Without attachments, the downstream two-thirds of the elevon surface indicates a slight decrease in heating. The contours remain essentially the same when either the large tip plate or the end plate with a 0.64-cm gap are attached to the wing (fig. 18). However, the contours change notably when the end plate is attached with no gap between it and the elevon (fig. 19). Further significant changes in the heating distribution occur when both the end plate and large tip plate are attached (fig. 20). Attaching the end plate also alters significantly the heating contours on the 10° elevon on the 50° swept wing (figs. 21 and 22).

Contours for the 70° wing and 10° elevon are shown in figures 23 to 27. As indicated by the dashed contours 1A and 2A in figure 23, attaching the small tip plate increases the extent of the region of high heating rates but does not affect the other contours. The contours are altered when the small tip plate is replaced by the small tip fin (fig. 24), and the heating distribution is changed considerably when the end plate is attached to the wing (fig. 25). Only the inboard region of highest heating (contours 1 and 1A, fig. 26) is affected by a gap when both the end plate and large tip plate are attached to the wing. When the cylindrical body is attached to the wing (fig. 27), the contours on the wing and elevon remain unchanged whether or not the large tip fin is also attached.

The oil accumulation line evident in figure 28 demarcates approximately the extent of the region of increased heating on the end plate caused by the elevon (fig. 29). The contours on the end plate are not affected noticeably by wing sweep nor by whether or not the large tip plate is attached to the wing. However, the heat transfer and the extent of increased heating are reduced when there is a gap between the elevon and end plate (fig. 30). The oil accumulation line on the cylindrical body surface (fig. 31) demarcates the region of increased heating on the body (fig. 32); the oil pattern and the heating distribution are not affected by attaching the large tip fin to the wing.

Elevon Deflection Angle of 20°

Heating distributions on the various wing and 20° elevon surfaces are presented in figures 33 to 40. Contours on the unswept wing and 20° elevon (fig. 33) are approximately the same whether or not the small tip plate, the large tip plate, the end plate (with or without a gap), or both the end plate and large tip plate are attached to the wing. As indicated in table IV, the contours shown in figure 33 represent the wing and elevon data for six different model configurations. The contours on the 50° wing and 20° elevon are similar with or without the end plate (fig. 34).

For the 70° wing, the small tip plate alters the regions of highest heating (contours 1A and 2A) on the elevon (fig. 35). The small tip fin alters the contours on both the wing and elevon (fig. 36). The heating distribution on the elevon is also affected by the end plate and by whether or not there is a gap between the end plate and elevon (figs. 37 and 38). With or without a gap between elevon and end plate, attaching the large tip plate increases the region of high heating on the outboard portion of the elevon (dashed contours 1A, 2A, and 3A in figs. 37 and 38). Contours on the wing and elevon with the cylindrical body attached are presented in figures 39 and 40. The effects of attaching either the large tip plate or the large tip fin are indicated in figure 40. The first two contours in figure 40 differ only slightly on the elevon surface when the plate is replaced by the fin; the third dashed contour, 3A ($h = 350 \text{ W/m}^2\text{-K}$), shows an embedded region of high heating on the elevon.

Oil flow patterns (figs. 41 and 42) and heating contours (fig. 43) on the end plate surface are not affected by wing sweep or the addition of the large tip plate. The extent of the region of increased heating on the end plate is reduced when there is a gap (fig. 44); the contours in this region are

unaffected by wing sweep and the addition of the large tip plate. Neither the large tip plate nor the large tip fin substantially affect the heating on the cylindrical body caused by the 20° elevon (fig. 45). The heating pattern appears somewhat complex because several of the relatively high heating areas are separated by regions of lower heating.

Elevon Deflection Angle of 30°

The 30° elevon separates the flow ahead of the hinge line, as evidenced by the oil accumulation line in figure 46. The separation line curves toward the hinge line near the inboard and outboard edges of the elevon. Heating contours for this configuration are shown in figure 47. Also shown in figure 47 are the changes in the contours caused by attaching either the small tip plate (contours 1A, 2A, and 3A) or the large tip plate (contours 1B, 2B, and 3B). Contours on the unswept wing and 30° elevon when the end plate is attached with large gaps are shown in figure 48. For the 1.27-cm gap, the contours on the elevon are straight spanwise lines, similar to those shown in figure 47 for no attachments. The region of high heating increases on the inboard portion of the elevon for the 0.95-cm gap (contours 1A and 2A), and increases further for the 0.64-cm gap (contours 1B and 2B). Attaching the end plate and large tip plate prevents outflow from the separated flow region and results in straight oil accumulation lines near the attached plate (figs. 49 and 50). Heating contours on the unswept wing and 30° elevon when the end plate is attached with a 0.32-cm gap are presented in figure 51. The regions of relatively high heating on the wing and elevon are increased inboard when the end plate is attached with no gap; these regions of heating are increased outboard when the large tip plate is also attached (contours 1A, 2A, 3A, and 5A). Heating contours on the 50° wing and 30° elevon are presented in figure 52. An oil flow photograph of the wing and elevon with the end plate attached is shown in figure 53; heating contours for the same configuration are shown in figure 54.

Separation ahead of the elevon on the 70° wing is evidenced by the oil accumulation line apparent in figure 55; the heating contours for the same configuration are presented in figure 56. The change in the separation line caused by attaching the small tip fin is evident in figure 57. Contours on the wing and elevon with either the small tip plate or the small tip fin (contour 2A) are shown in figure 58. Separation locations when the end plate is attached with no gap or with a 0.64-cm gap are indicated by the oil accumulation lines in figures 59 and 60. The contours for these configurations are shown in figure 61 (contours 1A and 2A indicate change caused by 0.64-cm gap). Contours on the wing and elevon with the large tip plate attached and with the end plate attached with various gaps are presented in figure 62. The smaller the gap, the larger the region of high heating on the inboard portion of the elevon (contours 1A and 2A for 0.32-cm gap, contours 1B and 2B for 0.64-cm gap). An oil flow photograph and heating contours for the configuration with the large tip plate and end plate with no gap are shown in figures 63 and 64. Sample frames from motion pictures showing the oil film flow on the 70° wing and 30° elevon surfaces, with the cylindrical body and various wing tip attachments, are presented in figures 65 to 68. Constant h contours for three of

these configurations are shown in figure 69. The large tip fin has essentially no effect on the heating distribution, but the large tip plate alters the contours (1A, 2A, and 3A in fig. 69) on the outboard portion of the elevon. (Sample motion picture frames of phase change coating for one of these configurations were mentioned earlier and are shown in fig. 6.)

Oil flow patterns and heating distributions on the end plate, for 30° elevon deflections, are not substantially affected by the addition of the large tip plate or by wing sweep (figs. 70 to 73). (As indicated in table IV, the contours shown in fig. 73 represent the heating distributions on the end plate for five different configurations.) The extent of the region of heating on the end plate caused by the elevon is decreased when there is a gap, but is not affected by wing sweep (fig. 74). Similarly, the oil accumulation lines occur further aft when there is a gap, but are at the same location whether the wing is unswept or swept 70° (figs. 75 and 76). The extent of the region of increased heating on the end plate diminishes with increasing gap size and is independent of wing sweep. In addition, the region of increased heating is not affected by whether or not the large tip fin is attached (figs. 77 to 79).

The oil accumulation line on the cylindrical body demarcates approximately the forward extent of heating caused by the 30° elevon (figs. 80 and 81). The heating distributions on the body are not affected by attaching either the large tip plate or large tip fin (fig. 81).

DISCUSSION OF RESULTS

Elevon Deflection Angle of 0°

Planform and profile oil flow motion pictures were examined and revealed streamwise flow over the silicone rubber portions of the end plate, wing, and undeflected elevon (fig. 13). The streamwise nature of the flow is unaffected by wing sweep and remains unchanged when the end plate and/or tip plate are attached. Heating contours on the wing and elevon parallel the wing leading edges; the contours on the end plate parallel the swept leading edge of the end plate. Neither the end plate nor any tip attachment has any substantial effect on the heating distributions on the wing and undeflected elevon (figs. 8, 10, and 11). The heating distribution on the end plate is not affected by wing sweep, nor is it affected by whether the large tip plate is attached to the wing (fig. 14). The experimental heating distribution on the unswept wing is compared with theoretical distributions in figure 9.

The cylindrical body causes a small outboard component of the streamlines on the portion of the 70° wing near the body. A streak of relatively high heating occurs near the body approximately where the inviscid body shock would strike the wing surface. The heating distribution on the outboard portion of the 70° wing is not affected by the cylindrical body. (Cf. figs. 11 and 12.) The oil flow on the cylindrical body accumulates along the tangency line between the cylindrical and planar portion of the body (fig. 15). The heating contours parallel the ridge line of the body (figs. 16 and 17).

Elevon Deflection Angle of 10°

The 10° elevon on the unswept wing experiences a slight decrease in heating on the downstream surface (fig. 18). However, when the end plate is attached with no gap, the heating on the elevon is reduced considerably, and a streak of comparatively low heating appears on the inboard portions of the wing and elevon near the end plate (fig. 19). When both the end plate and large tip plate are attached, a region of relatively high heating appears on the wing just upstream of the hinge line (fig. 20). The region of high heating on the elevon occurs near the trailing edge in this case. Heating distributions on the elevon on the 50° wing are substantially different from those on the unswept wing (cf. figs. 18 and 21), and attaching the end plate causes large changes in the heating distributions (cf. figs. 21 and 22). Attaching the end plate to the 50° wing increases the heating on the 10° elevon. The highest heating on the 10° elevon is experienced when it is on the 70° wing. This high heating region occurs on the outboard portion of the elevon, and the extent and location of this region are altered when either the small tip plate or small tip fin are attached (figs. 23 and 24). The heating on the elevon is reduced when both the end plate and large tip plate are attached, but the heating is even lower when only the end plate is attached (cf. figs. 23 to 26). The heating distribution on the elevon is also changed substantially when the cylindrical body is attached to the wing (fig. 27). In this case a streak of relatively high heating appears on the wing surface (similar to that experienced for no elevon deflections, cf. figs. 12 and 27).

The 10° elevon causes an oil accumulation line to appear on the end plate surface (fig. 28). This line forms a much larger angle with the free-stream direction than that predicted by inviscid shock theory, and downstream of the line the oil flow on the end plate parallels the oil accumulation line instead of the elevon surface, contrary to what would be anticipated using inviscid flow analyses (ref. 25). The extent of increased heating on the end plate caused by the 10° elevon is demarcated approximately by the oil accumulation line (cf. figs. 28 and 29). The heating and the extent of heating are reduced when there is a gap between the end plate and elevon (fig. 30). Neither sweeping the wing nor attaching the large tip plate affect the heating distributions on the end plate. With a 10° elevon, the cylindrical body experiences somewhat higher heating than the end plate (cf. figs. 29 and 32).

Elevon Deflection Angle of 20°

Planform oil flow motion pictures give no indication of flow separation ahead of the 20° elevon for any configuration tested. Heating distributions on the elevon are similar for both the unswept and 50° wings. For both wings the heating is highest on the aft portion of the elevon, and the heating contours are independent of whether or not the end plate and large or small tip plates are attached (figs. 33 and 34). A large change in the heating distribution occurs when the elevon is on the 70° wing (figs. 35 to 38). The heating on the elevon is much higher for the 70° swept wing, with the highest heating occurring on the forward portion of the elevon. Further, for the 70° wing, the end plate and the various tip attachments strongly affect the heating distributions (figs. 35 to 38). The cylindrical body results in regions of high heating on

the portions of the wing and elevon near the body. Heating distributions on the 20° elevon are changed significantly when either the large tip plate or large tip fin are attached in addition to the cylindrical body (figs. 39 and 40).

Oil accumulation lines on the end plate are at a considerably larger angle with the free-stream direction than the shock-wave angle for a 20° flow deflection (ref. 26). Downstream of the lines, the surface flow on the end plate parallels the oil accumulation lines instead of following the elevon surface direction (figs. 41 and 42). The lines demarcate approximately the region of increased heating on the end plate caused by the elevon (cf. figs. 41 to 43). The oil patterns and heating distributions on the end plate are not affected by sweeping the wing or by attaching the large tip plate. The reduced extent of increased heating when there is a gap (cf. figs. 43 and 44) is also unaffected by wing sweep and the addition of the large tip plate. Maximum heating on the end plate near the 20° elevon is approximately the same as that on the cylindrical body (cf. figs. 43 to 45).

Elevon Deflection Angle of 30°

The 30° elevon forces flow separation and increases the heating on the wing surface upstream of the hinge line. High heating is experienced on the elevon in the vicinity of flow reattachment downstream of the hinge line. Attaching the end plate and/or large tip plate prevents venting of the separated flow region on the side adjacent to the attached plate. This results in a more nearly constant extent of separation and somewhat larger regions of high heating on the wing and elevon in the vicinity of the attached plate (figs. 46 to 51). However, for end plate-elevon gaps greater than 0.5 cm, the end plate does not affect the heating distribution on the wing (figs. 48 and 51).

Separation lines and heating contours upstream of the hinge line on the swept wings are not symmetric about the elevon midspan line. The streamwise extent of separation is smaller, but the heating is greater on the outboard portion than on the inboard portion of the swept wings. This effect is more pronounced for the 70° wing than for the 50° wing (figs. 52 to 56). Heating contours on the elevon are fairly symmetric about the elevon midspan line for the 50° wing, but indicate higher heating on the outboard portion of the elevon than on the inboard portion for the 70° wing (figs. 52 and 56). Attaching the end plate or the small tip plate increases the high heating region on the portion of the elevon adjacent to the attached plate (figs. 54, 58, and 61). Attaching the end plate with a gap and the large tip plate yields similar results (fig. 62). However, when the end plate with no gap and large tip plate are both attached, thereby preventing any spanwise venting of the separated flow, the highest heating on the elevon occurs only adjacent to the attached plates and not along the hinge line. The aft portion of the elevon experiences higher heating than the forward portion in this case (fig. 64).

The oil accumulation line on the 70° wing surface is highly asymmetric when the cylindrical body is attached to the model (figs. 65 to 68). The extent of the region of increased heating on the wing is demarcated approximately by the oil accumulation line (cf. figs. 65 and 69). The heating contours on the

elevon are also highly asymmetric. The highest heating regions are near the cylindrical body and near the large tip plate, when it is attached (fig. 69).

Whether there is no gap (figs. 70 to 73) or whether there is a gap (figs. 74 to 79), wing sweep and wing tip attachments do not substantially affect either the oil flow pattern or the heating distribution on the end plate. Again, the oil accumulation lines demarcate the regions of increased heating on the end plate. Both the magnitude and extent of increased heating on the end plate are reduced when there is a gap. The maximum heating on the cylindrical body is comparable to that on the end plate when there is a gap; it is less than the maximum heating on the end plate when there is no gap. (Cf. figs. 73, 74, 77 to 79, and 81.)

CONCLUDING REMARKS

Data are presented on basic, flat plate configurations for which there are important three-dimensional separated flow effects that are not predictable using current theoretical methods. The configurations are representative of the fuselage-wing-elevon portions of hypersonic aircraft. The data, obtained for Mach 6 flow and a wing root chord Reynolds number of approximately 17×10^6 , can be used to guide analyses of flap or elevon-induced heating on adjacent surfaces of hypersonic aircraft for similar geometries and flow conditions.

The heat transfer coefficients on the unswept wing and undeflected elevon surfaces approximate those predicted by current analytical methods (refs. 26 to 29). Constant heat transfer coefficient contours for undeflected elevons parallel the wing and end plate leading edges on these surfaces and the ridge line on the cylindrical body.

Neither 10° nor 20° elevon deflections have substantial effects on the wing surface flow or heating distribution. Heating distributions on the 10° elevon surface depend strongly on wing sweep and whether or not the end plate or the cylindrical body are attached to the wing. Heating distributions on the 20° elevon surface depend weakly on whether the wing is unswept or swept 50° and are insensitive to an attached end plate for these wing sweeps. However, the heating distribution on the 20° elevon surface on the 70° swept wing differs greatly from that on the unswept or 50° swept wings. Thus, in certain instances, the heating distributions depend strongly on the geometric parameters varied in this study.

The 30° elevon separates the flow from the wing surface upstream of the hinge line; heat transfer to the wing is substantially increased in the separated flow region. The extent of separation is asymmetric about the elevon midspan line for the swept wings; the asymmetry is particularly pronounced when the cylindrical body is attached to the 70° swept wing. Heating distribution patterns on the 30° elevon depend on wing sweep and on whether or not a plate or body is attached to the model. The maximum heat transfer observed on the 30° elevon is comparable to the maximum value observed on the 20° elevon, but the distributions differ substantially.

Regions of increased heating on the end plate, induced by the deflected elevons, are considerably larger than use of inviscid-flow elevon shock-wave angles would suggest. The surface flows in these regions parallel the oil accumulation lines (which closely approximate the extents of the regions of increased heating) and not the deflected elevon surface direction. The heating distributions on the end plate are not significantly affected by sweeping the wing or by attaching a tip plate or tip fin. However, the extent of the region of increased heating diminishes substantially with increasing gap size between the elevon and end plate surface.

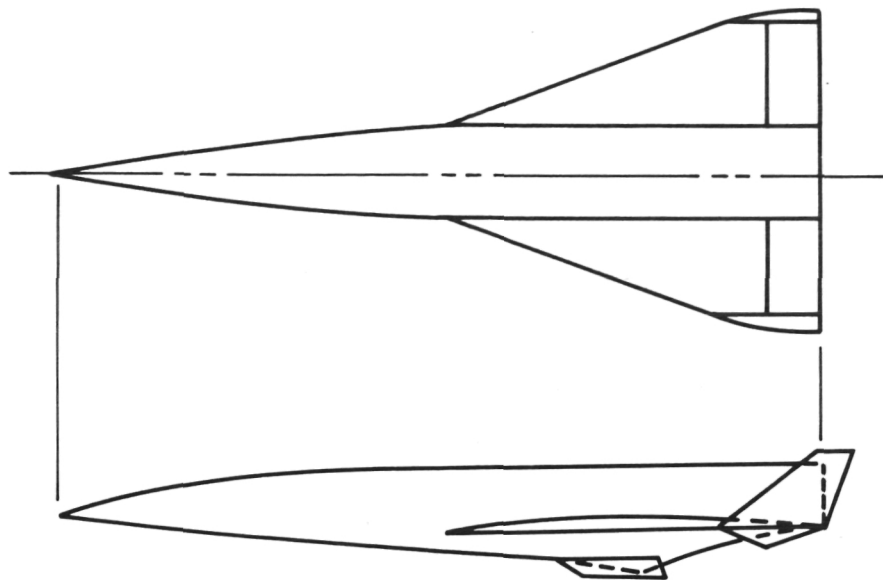
Langley Research Center
National Aeronautics and Space Administration
Hampton, VA 23665
April 21, 1978

REFERENCES

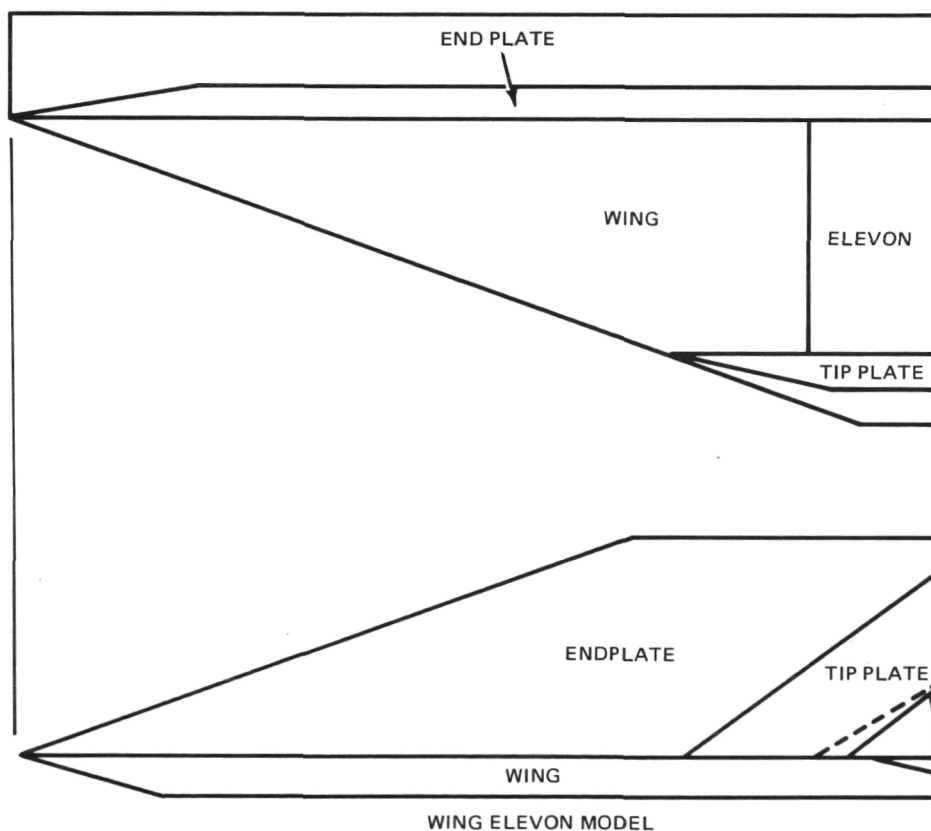
1. Korkegi, Robert H.: Survey of Viscous Interactions Associated With High Mach Number Flight. AIAA J., vol. 9, no. 5, May 1971, pp. 771-784.
2. Ryan, B. M.: Summary of Aerothermodynamic Interference Literature. Tech. Note 4061-160, Naval Weapons Center (China Lake, Calif.), Apr. 1969.
3. Goldberg, Theodore J.: Three-Dimensional Separation for Interaction of Shock Waves With Turbulent Boundary Layers. AIAA J., vol. 11, no. 11, Nov. 1973, pp. 1573-1575.
4. Sedney, Raymond; and Kitchens, Clarence W., Jr.: The Structure of Three-Dimensional Separated Flows in Obstacle, Boundary-Layer Interactions. Flow Separation, AGARD-CP-168, Nov. 1975, pp. 37-1 - 37-15.
5. Korkegi, R. H.: Comparison of Shock-Induced Two- and Three-Dimensional Incipient Turbulent Separation. AIAA J., vol. 13, no. 4, Apr. 1975, pp. 534-535.
6. McCabe, A.: The Three-Dimensional Interaction of a Shock Wave With a Turbulent Boundary Layer. Aeronaut. Q., vol. XVII, pt. 3, Aug. 1966, pp. 231-252.
7. Peake, David J.; Rainbird, William J.; and Atraghji, Edward G.: Three-Dimensional Flow Separations on Aircraft and Missiles. AIAA J., vol. 10, no. 5, May 1972, pp. 567-580.
8. Whitehead, Allen H., Jr.; Sterrett, James R.; and Emery, James C.: Effects of Transverse Outflow From a Hypersonic Separated Region. AIAA J., vol. 10, no. 4, Apr. 1972, pp. 553-555.
9. Small, William J.; Kirkham, Frank S.; and Fetterman, David E.: Aerodynamic Characteristics of a Hypersonic Transport Configuration at Mach 6.86. NASA TN D-5885, 1970.
10. Chapman, Dean R.; Kuehn, Donald M.; and Larson, Howard K.: Investigation of Separated Flows in Supersonic and Subsonic Streams With Emphasis on the Effect of Transition. NACA Rep. 1356, 1958.
11. Hypersonic Aircraft by 2000 Pushed. Aviation Week & Space Tech., vol. 99, no. 12, Sept. 1973, pp. 52-57.
12. Clark, Louis E.; and Richie, Christine B.: Aerodynamic Characteristics at Mach 6 of a Hypersonic Research Airplane Concept Having a 70° Swept Delta Wing. NASA TM X-3475, 1977.
13. Creel, Theodore R., Jr.; and Penland, Jim A.: Low-Speed Aerodynamic Characteristics of a Hypersonic Research Airplane Concept Having a 70° Swept Delta Wing. NASA TM X-71974, 1974.

14. Nagel, A. L.; and Becker, J. V.: Key Technology for Airbreathing Hypersonic Aircraft. AIAA Paper No. 73-58, Jan. 1973.
15. Whitehead, Allen H., Jr.; and Keyes, J. Wayne: Flow Phenomena and Separation Over Delta Wings With Trailing-Edge Flaps at Mach 6. AIAA J., vol. 6, no. 12, Dec. 1968, pp. 2380-2387.
16. Kaufman, Louis G., II; and Freeman, L. Michael: Separation Ahead of Controls on Swept Wings. ARL TR 75-0134, U.S. Air Force, June 1975.
17. Edwards, A. J.: Heat Transfer Distributions on a 70° Delta Wing With Flap-Induced Separation. I.C. Aero Rep. 75-01, Imperial College of Science and Technology (London), Mar. 1975.
18. Kaufman, Louis G., II; and Johnson, Charles B.: Pressure Distributions Induced by Elevon Deflections on Swept Wings and Adjacent End-Plate Surfaces at Mach 6. NASA TM X-3470, 1977.
19. Jones, Robert A.; and Hunt, James L.: Use of Fusible Temperature Indicators for Obtaining Quantitative Aerodynamic Heat-Transfer Data. NASA TR-230, 1966.
20. Kaufman, Louis G., II; Leng, Jarvis; and Johnson, Arnold R.: Exploratory Tests Using Temperature-Sensitive Paints To Obtain Hypersonic Heat Transfer Data on Spheres and on Fin-Plate Models. RM-487, Grumman Aerospace Corp., Sept. 1970.
21. Hunt, James L.; and Jones, Robert A.: Heating and Flow-Field Studies on a Straight-Wing Hypersonic Reentry Vehicle at Angles of Attack From 20° to 80° With Simulation of Real-Gas Trends. NASA TN D-7108, 1973.
22. Maise, George; and Rossi, Michael J.: Lateral Conduction Effects on Heat-Transfer Data Obtained With the Phase-Change Paint Technique. NASA CR-2435, 1974.
23. Gillerlain, Joseph D., Jr.: Use of Phase-Change Paints To Study Fin-Body Interference Heating. NSWC/WOL/TR 75-62, U.S. Navy, Apr. 1976. (Available from DDC as AD A027 029.)
24. Goldberg, Theodore J.; and Hefner, Jerry M. (Appendix by James C. Emery): Starting Phenomena for Hypersonic Inlets With Thick Turbulent Boundary Layers at Mach 6. NASA TN D-6280, 1971.
25. Drummond, John Philip; Jones, Robert A.; and Ash, Robert L.: Effective Thermal Property Improves Phase Change Paint Data. AIAA J., vol. 14, no. 10, Oct. 1976, pp. 1476-1478.
26. Ames Research Staff: Equations, Tables, and Charts for Compressible Flow. NACA Rep. 1135, 1953. (Supersedes NACA TN 1428.)

27. Anderson, E. C.; and Lewis, C. H.: Laminar or Turbulent Boundary-Layer Flows of Perfect Gases or Reacting Gas Mixtures in Chemical Equilibrium. NASA CR-1893, 1971.
28. Harris, Julius E.: Numerical Solution of the Equations for Compressible Laminar, Transitional, and Turbulent Boundary Layers and Comparisons With Experimental Data. NASA TR R-368, 1971.
29. Hopkins, Edward J.; Keener, Earl R.; and Louie, Pearl T.: Direct Measurements of Turbulent Skin Friction on a Nonadiabatic Flat Plate at Mach Number 6.5 and Comparisons With Eight Theories. NASA TN D-5675, 1970.
30. Johnson, Charles B.; and Boney, Lillian R.: A Simple Integral Method for the Calculation of Real-Gas Turbulent Boundary Layers With Variable Edge Entropy. NASA TN D-6217, 1971.



HYPERSONIC RESEARCH AIRPLANE



WING ELEVON MODEL

Figure 1.- Outline of "typical" hypersonic research airplane and "wing-elevon" model configuration.

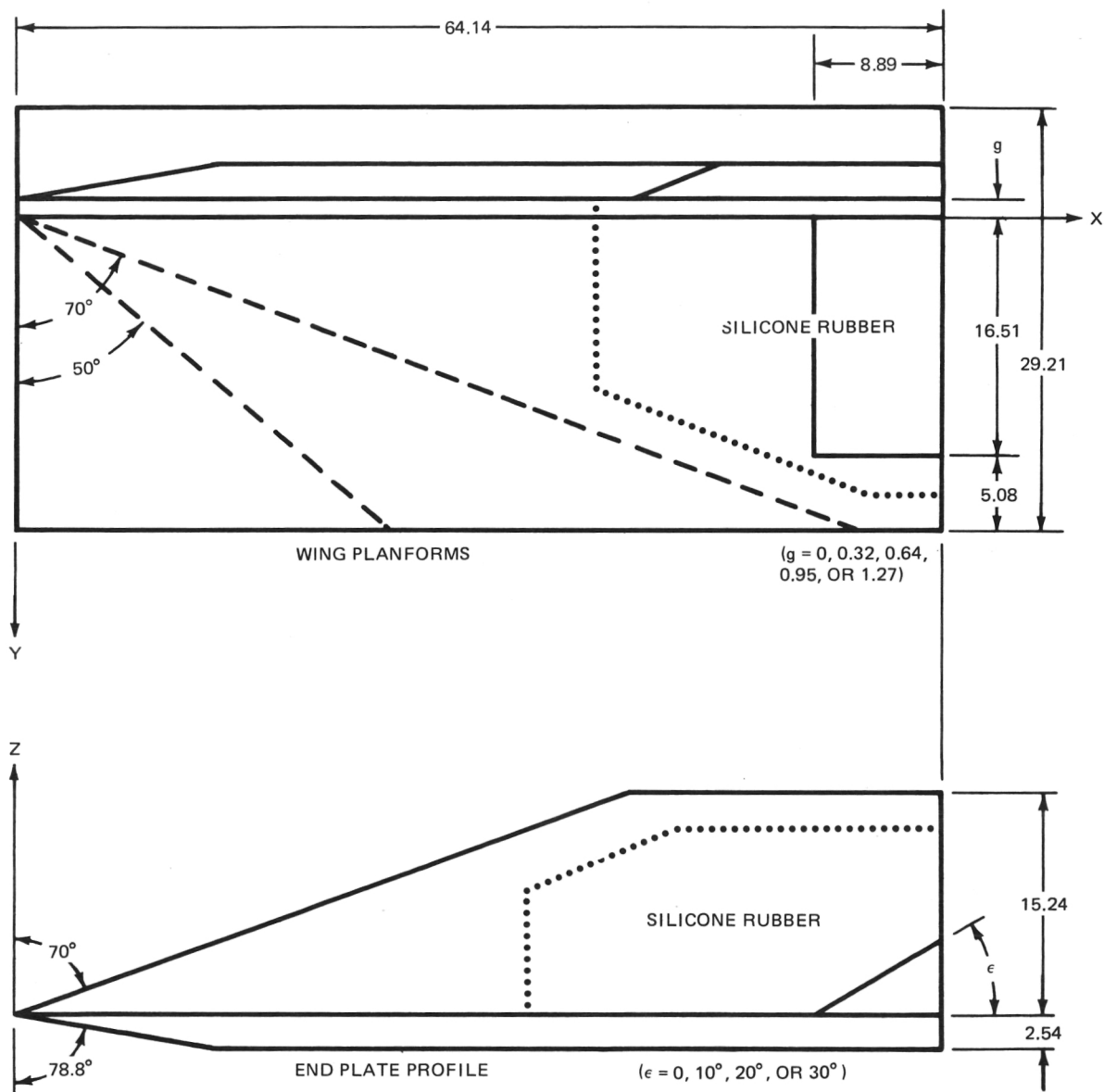


Figure 2.- Sketch of wing and end plate planforms for wing elevon model.
Linear dimensions are in cm.

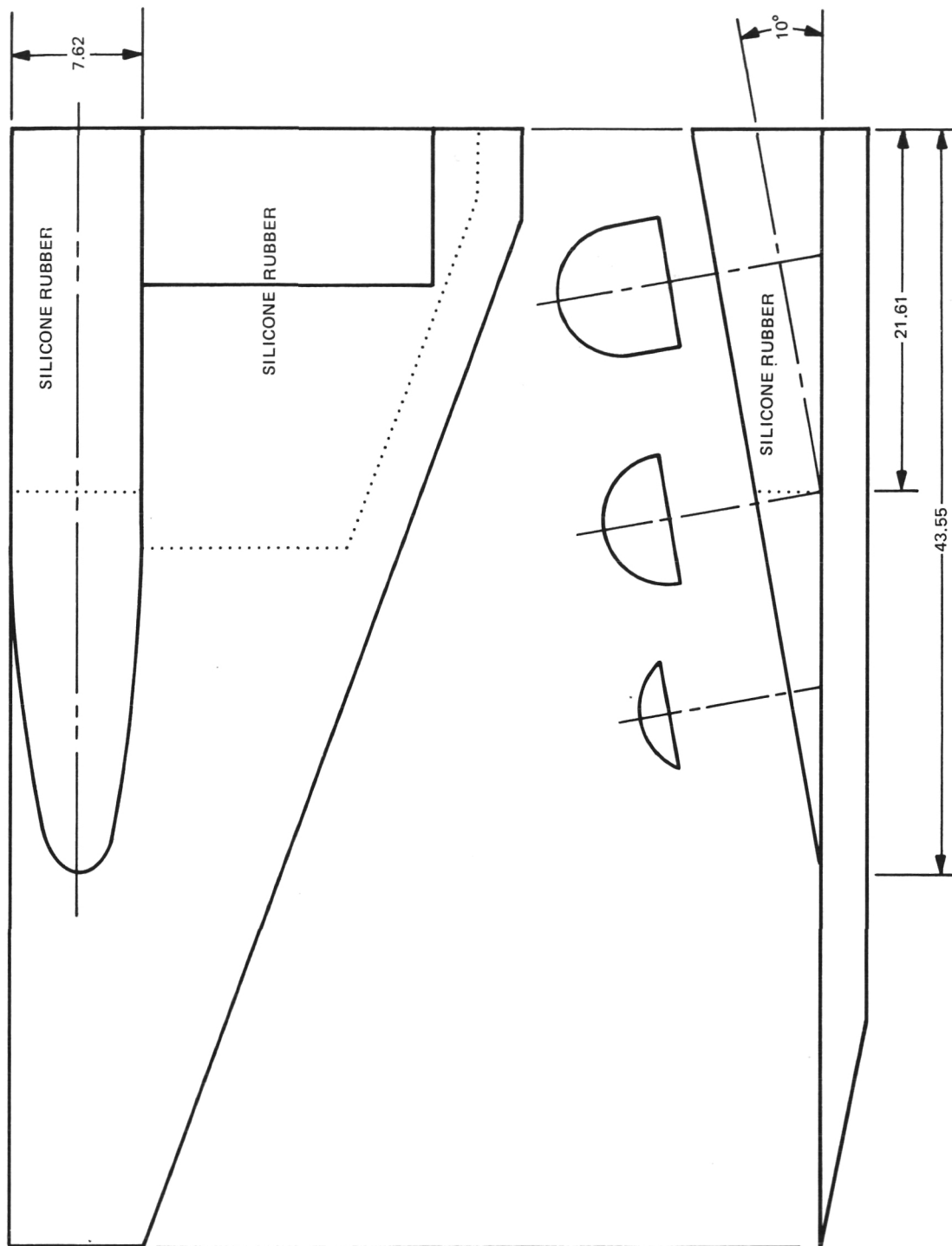


Figure 3.- Sketch of cylindrical body attached to 70° wing. Linear dimensions are in cm.

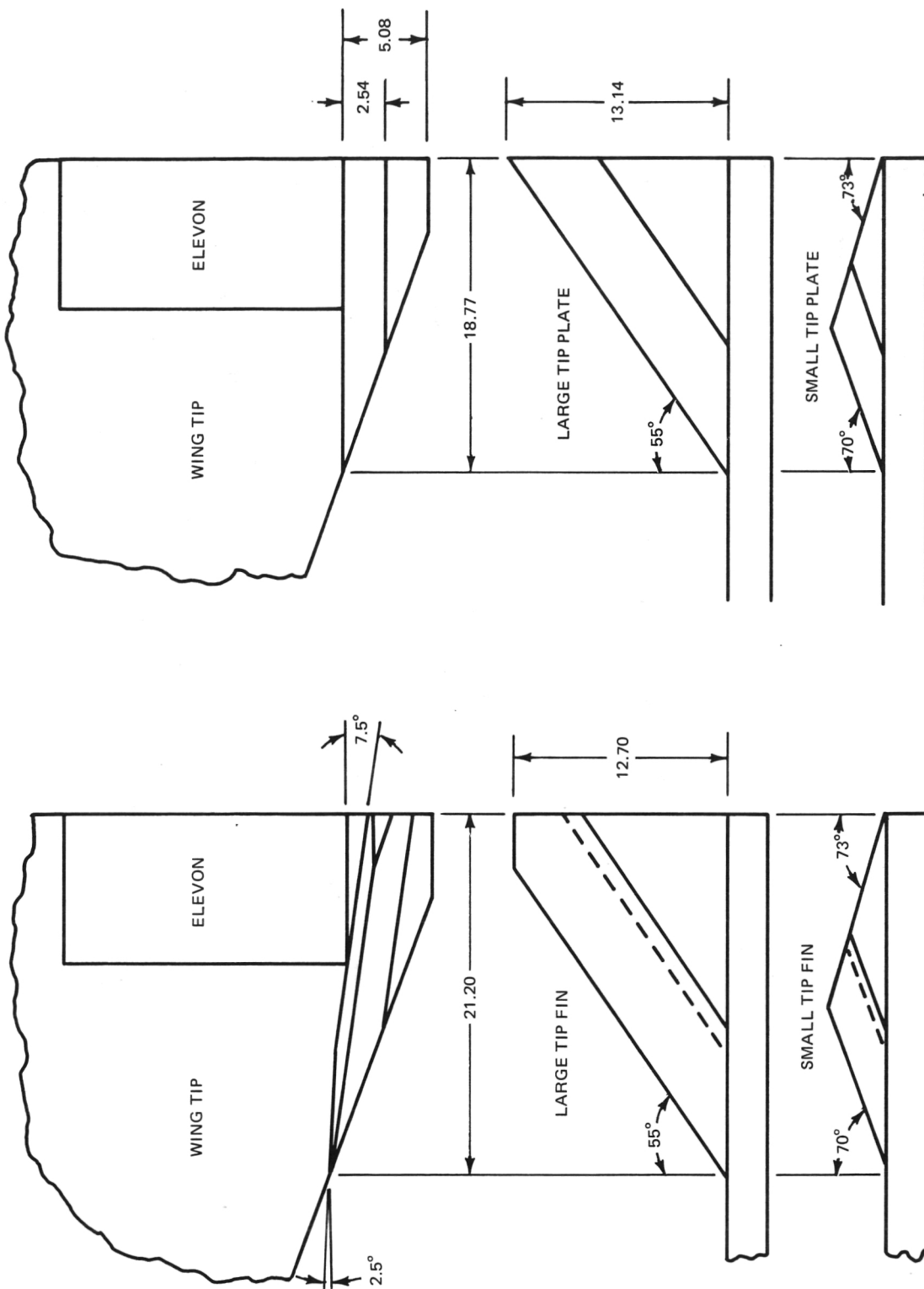
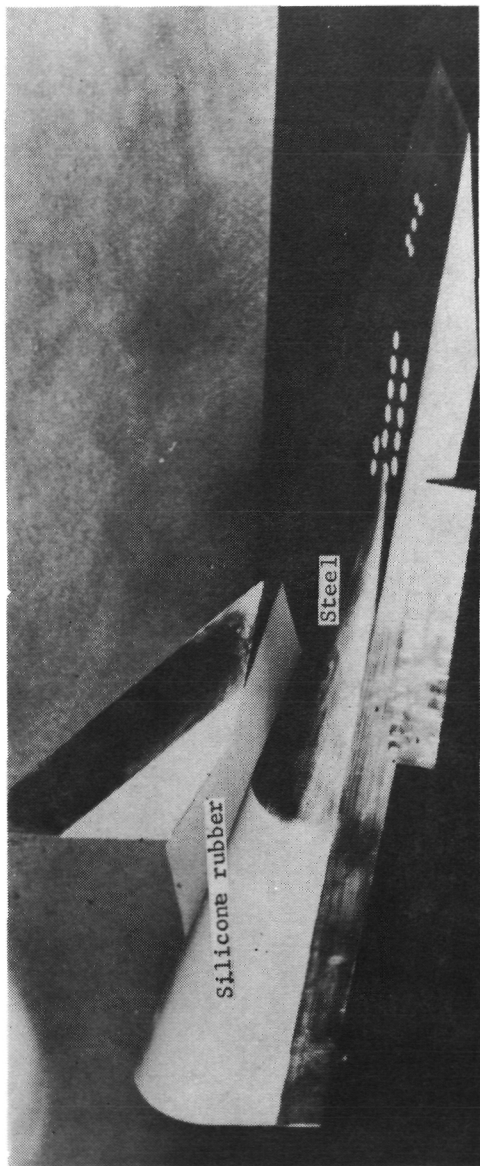
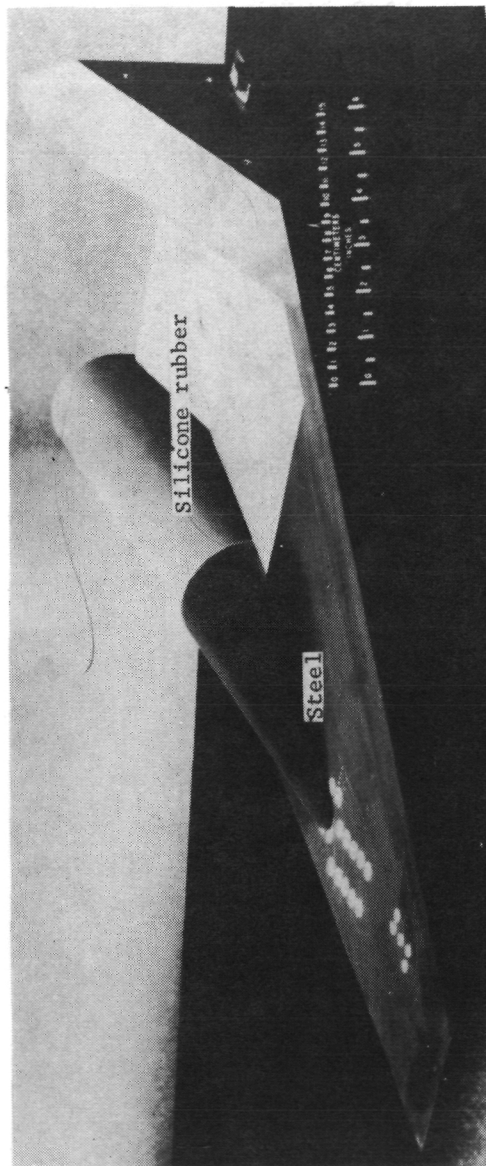


Figure 4.- Sketch of attachable tip fins and plates. Linear dimensions are in cm.

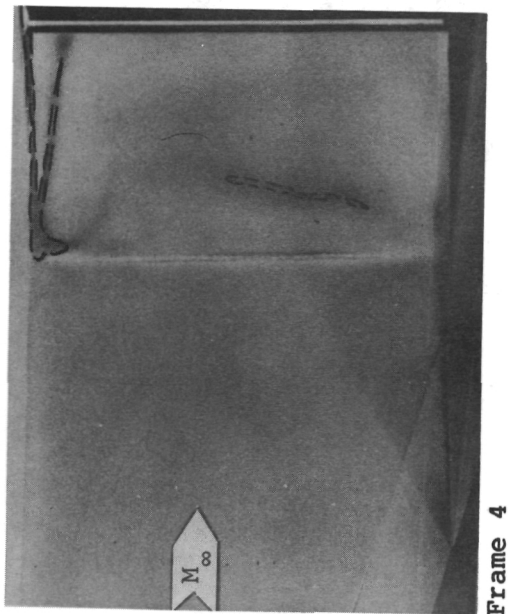


L-76-5852

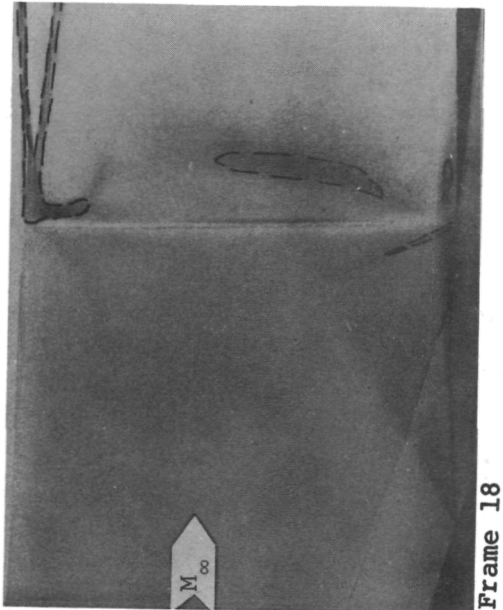


L-76-5853

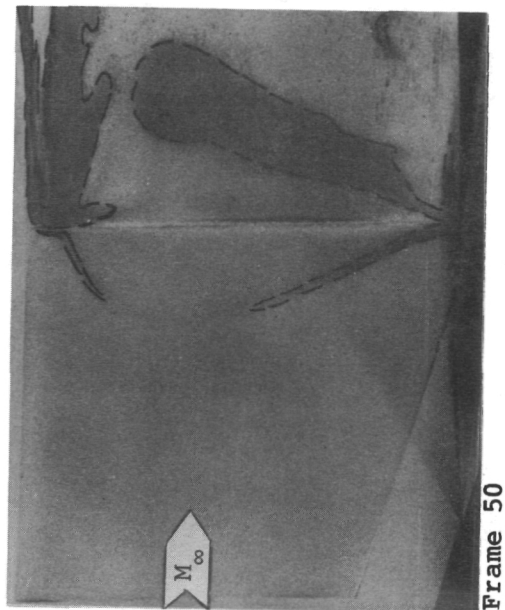
Figure 5.- Photographs of wing elevon model configuration; 70° wing with cylindrical body, large tip fin, and 20° elevon.



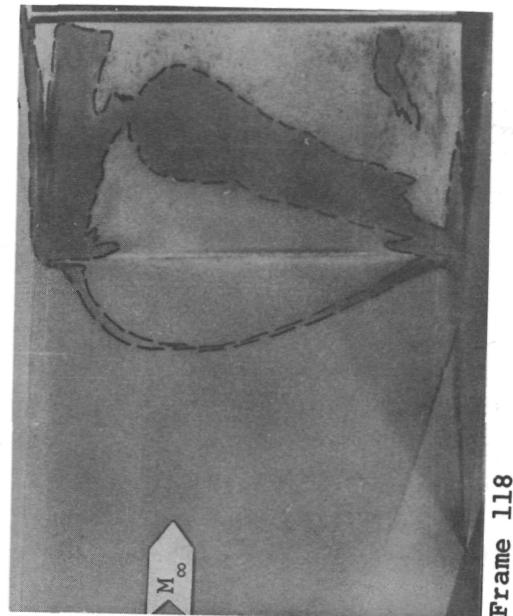
Frame 4



Frame 18



Frame 50

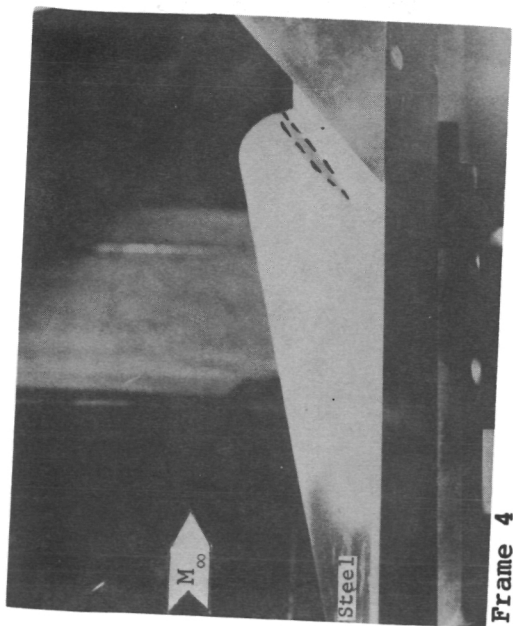


Frame 118

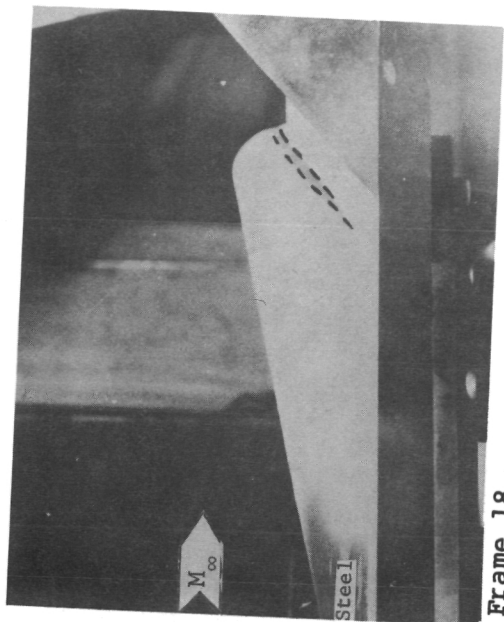
(a) Planform.

Figure 6.- Sample frames from profile and planform phase change paint motion pictures showing progression of melted paint regions with time for 70° wing with cylindrical body, large tip fin, and 30° elevon.

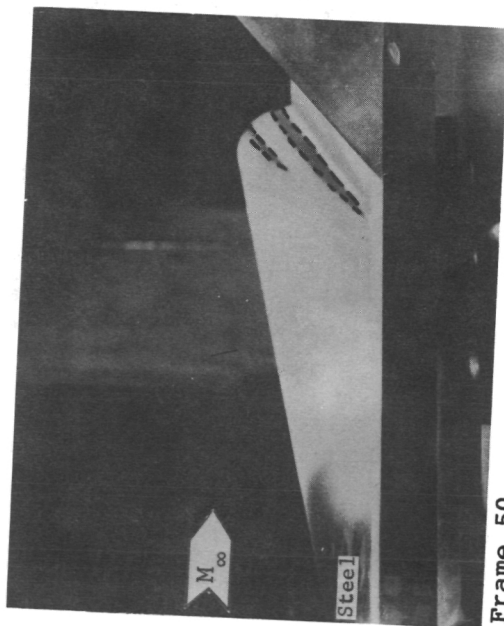
L-78-50



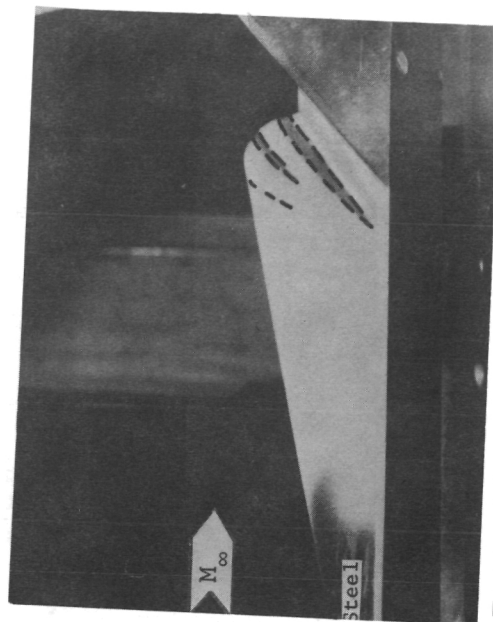
Frame 4



Frame 18



Frame 50



Frame 118

(b) Profile.

Figure 6.- Concluded.

L-78-51

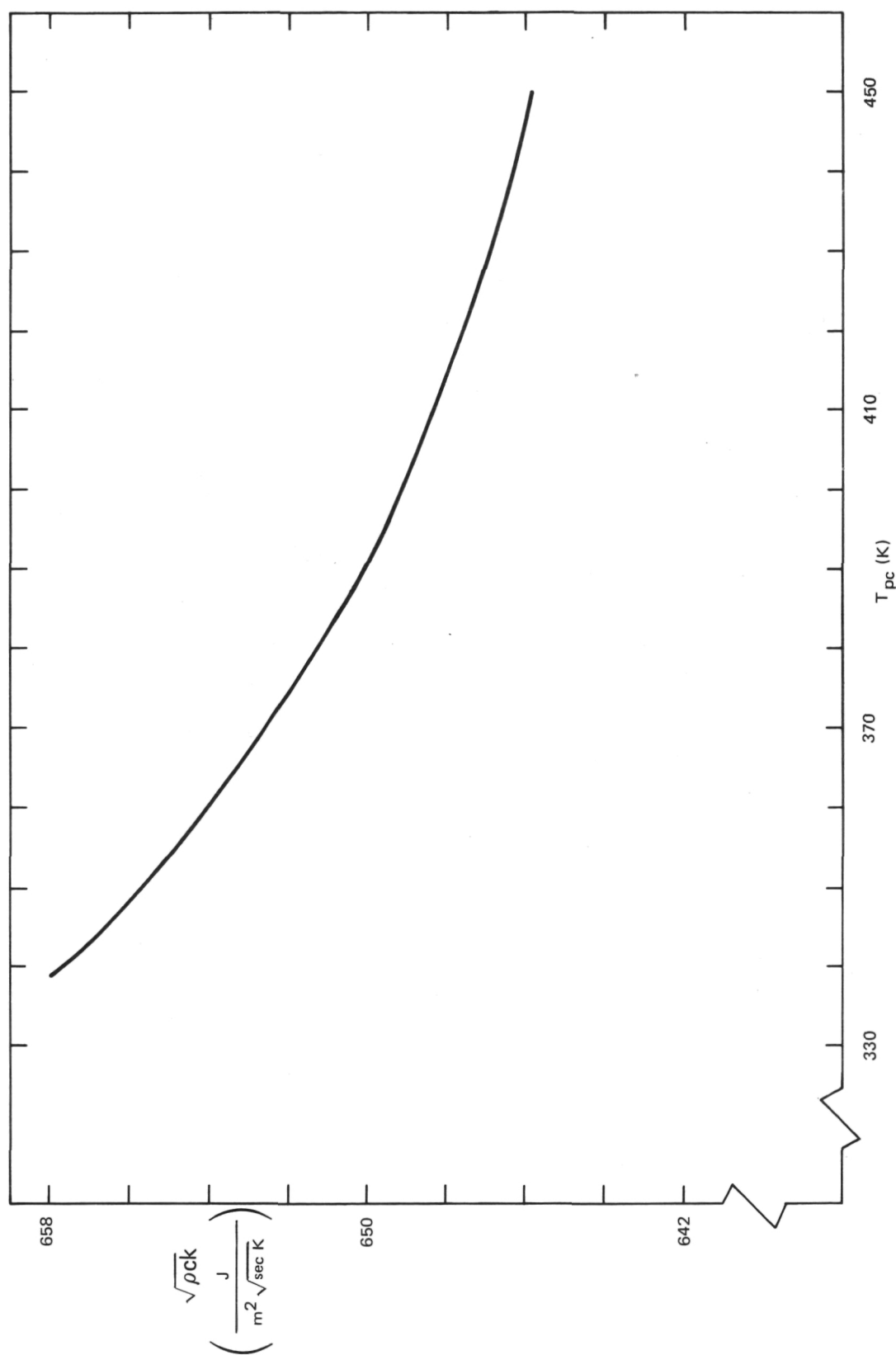
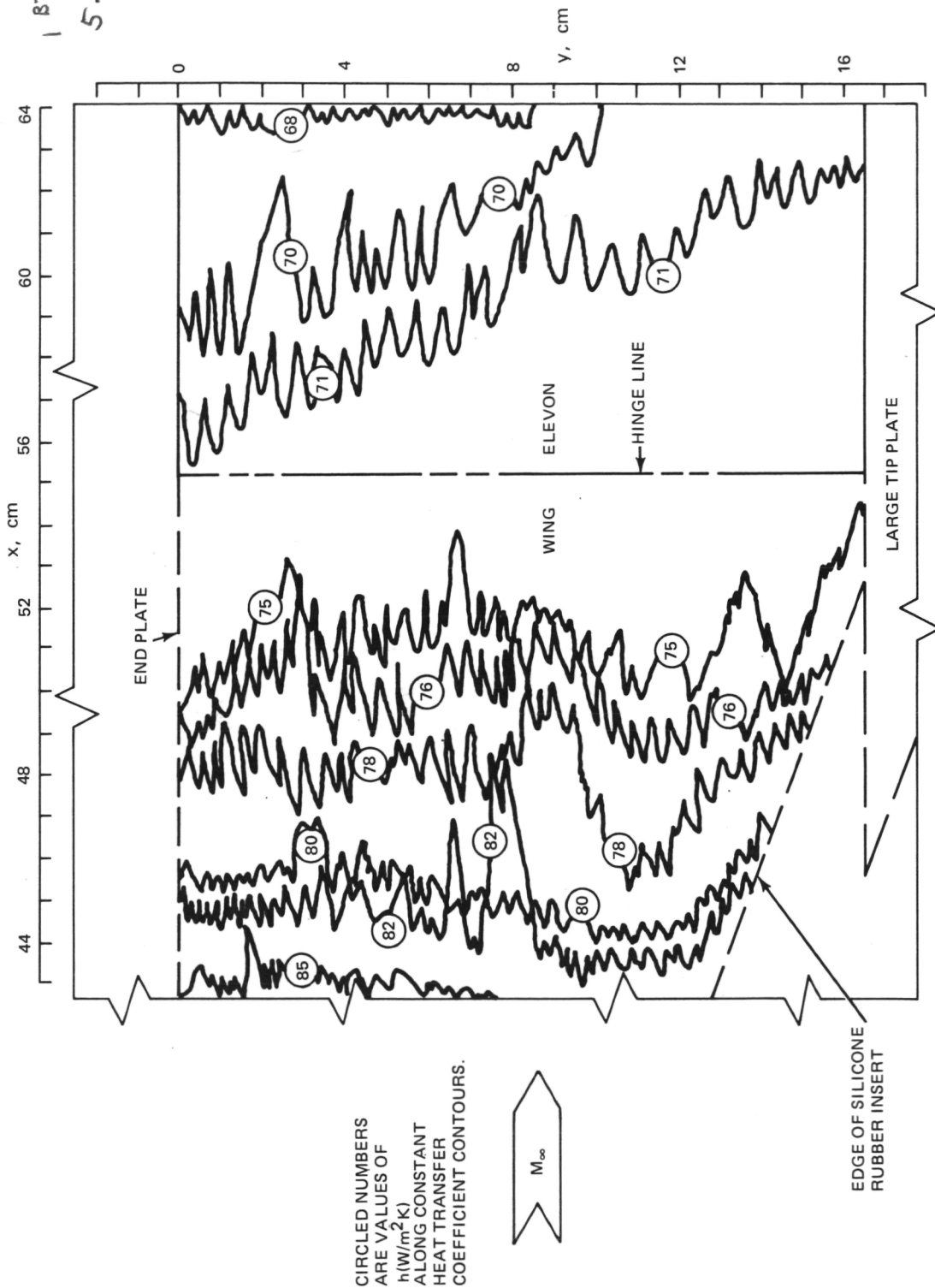


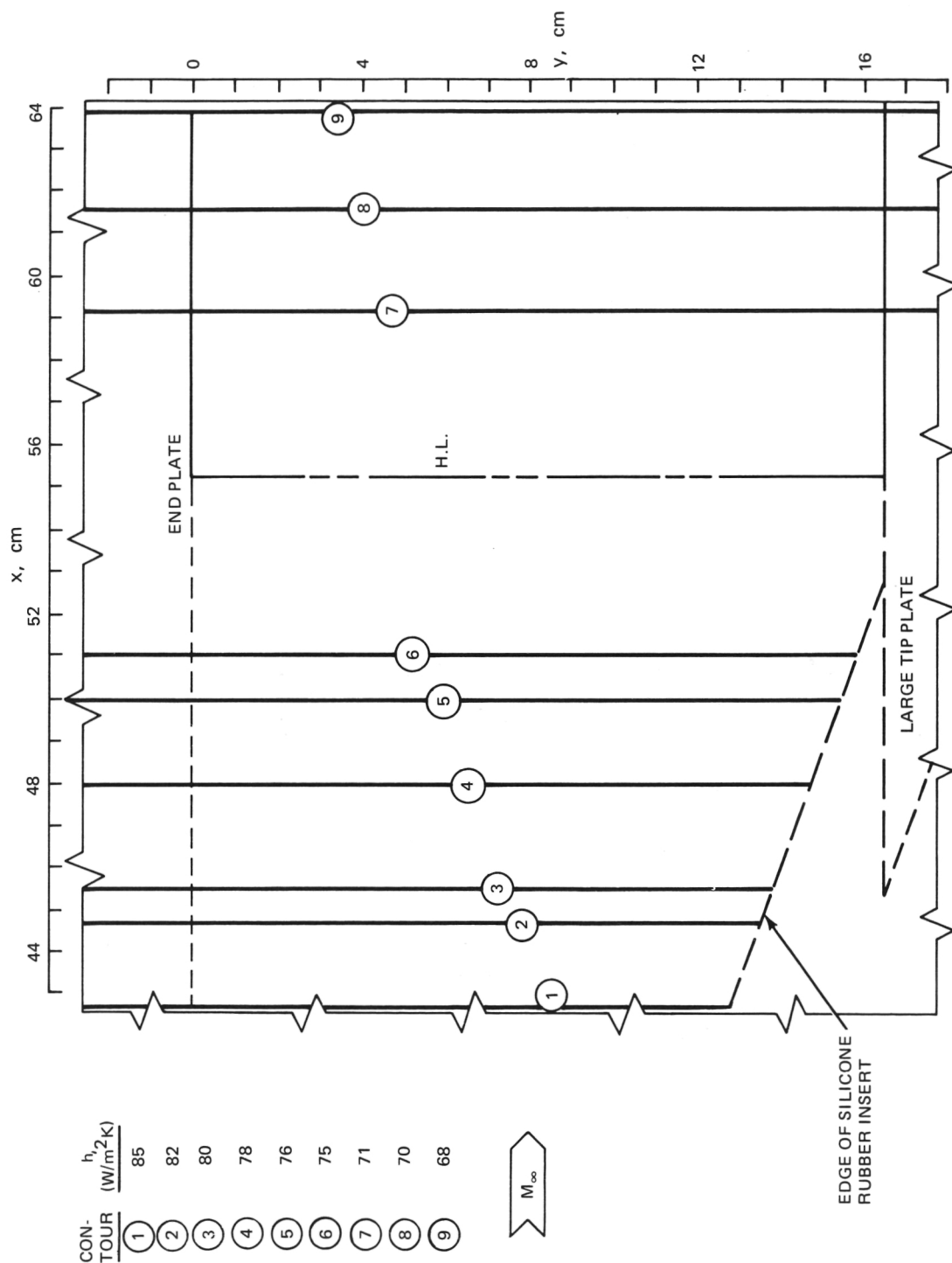
Figure 7.- Variation of $\sqrt{\rho ck}$ for silicone rubber material with surface temperature for $T_i = 296$ K.

$$1 \text{ BTU/hr-ft}^2\text{-}^\circ\text{F} = 5.6745 \text{ W/m}^2\text{-}^\circ\text{K}$$



(a) Actual contours.

Figure 8.- Constant heat transfer coefficient contours on wing and elevon surfaces. $\epsilon = 0^\circ$ and $\Lambda = 0^\circ$. Contours shown for four configurations: with and without end plate and/or large tip plate.



(b) Faired contours.

Figure 8.- Concluded.

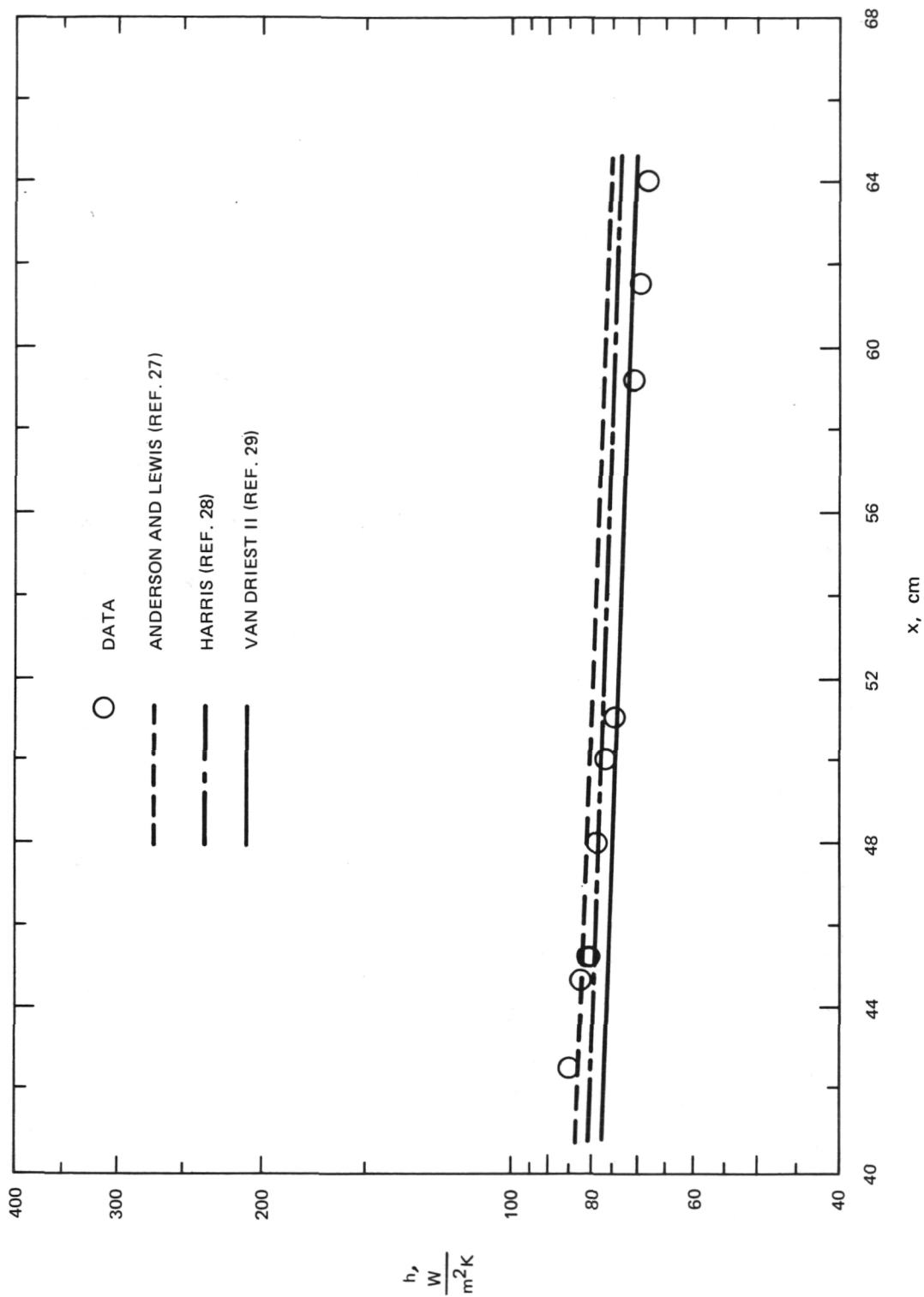


Figure 9.- Streamwise distributions of heat transfer coefficients on wing and elevon surfaces. $\Lambda = 0^\circ$ and $\epsilon = 0^\circ$.

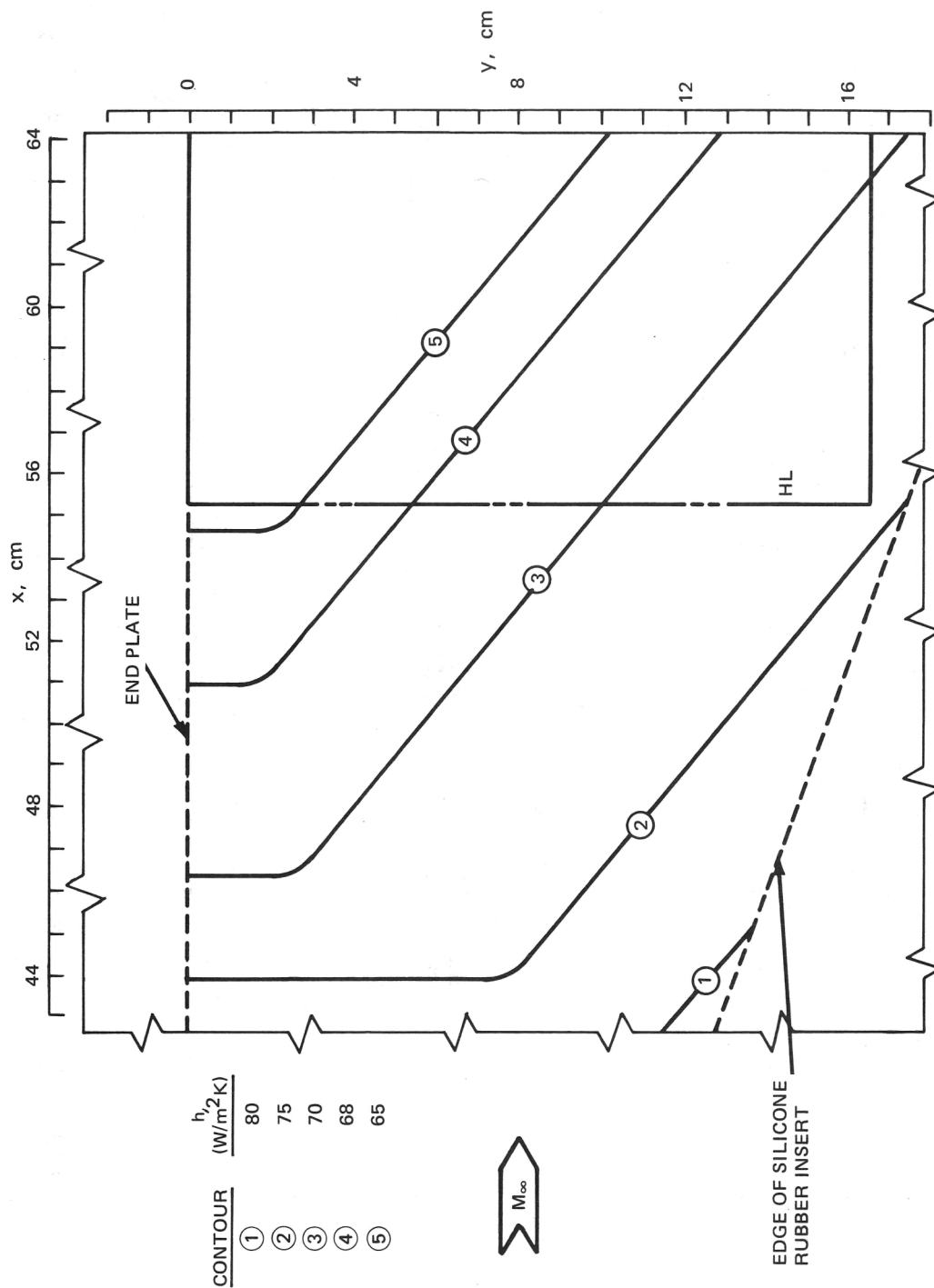


Figure 10.- Constant heat transfer coefficient contours on wing and elevator surfaces. $\epsilon = 0^\circ$ and $\Lambda = 50^\circ$. Contours shown for two configurations: with and without end plate.

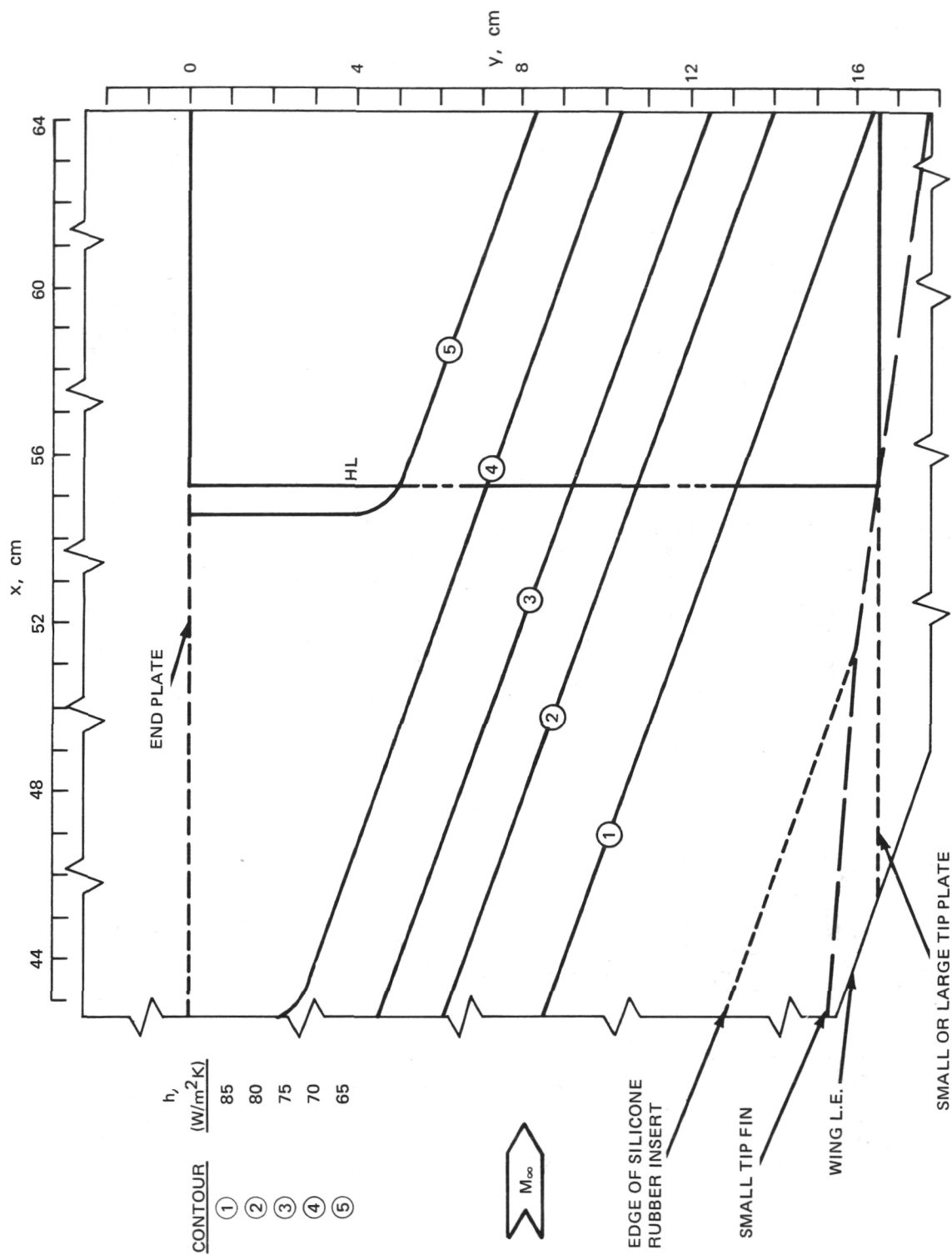


Figure 11.- Constant heat transfer coefficient contours on wing and elevon surfaces. $\epsilon = 0^\circ$ and $\Lambda = 70^\circ$. Contours shown for five configurations: with no attachment or with small tip plate, or small tip fin, or end plate, or end plate and large tip plate.

Figure 12.- Constant heat transfer coefficient contours on wing and elevon surfaces. $\epsilon = 0^\circ$; $\Lambda = 70^\circ$; and cylindrical body attached. Contours shown for two configurations: with and without large tip fin. L.E. denotes leading edge.

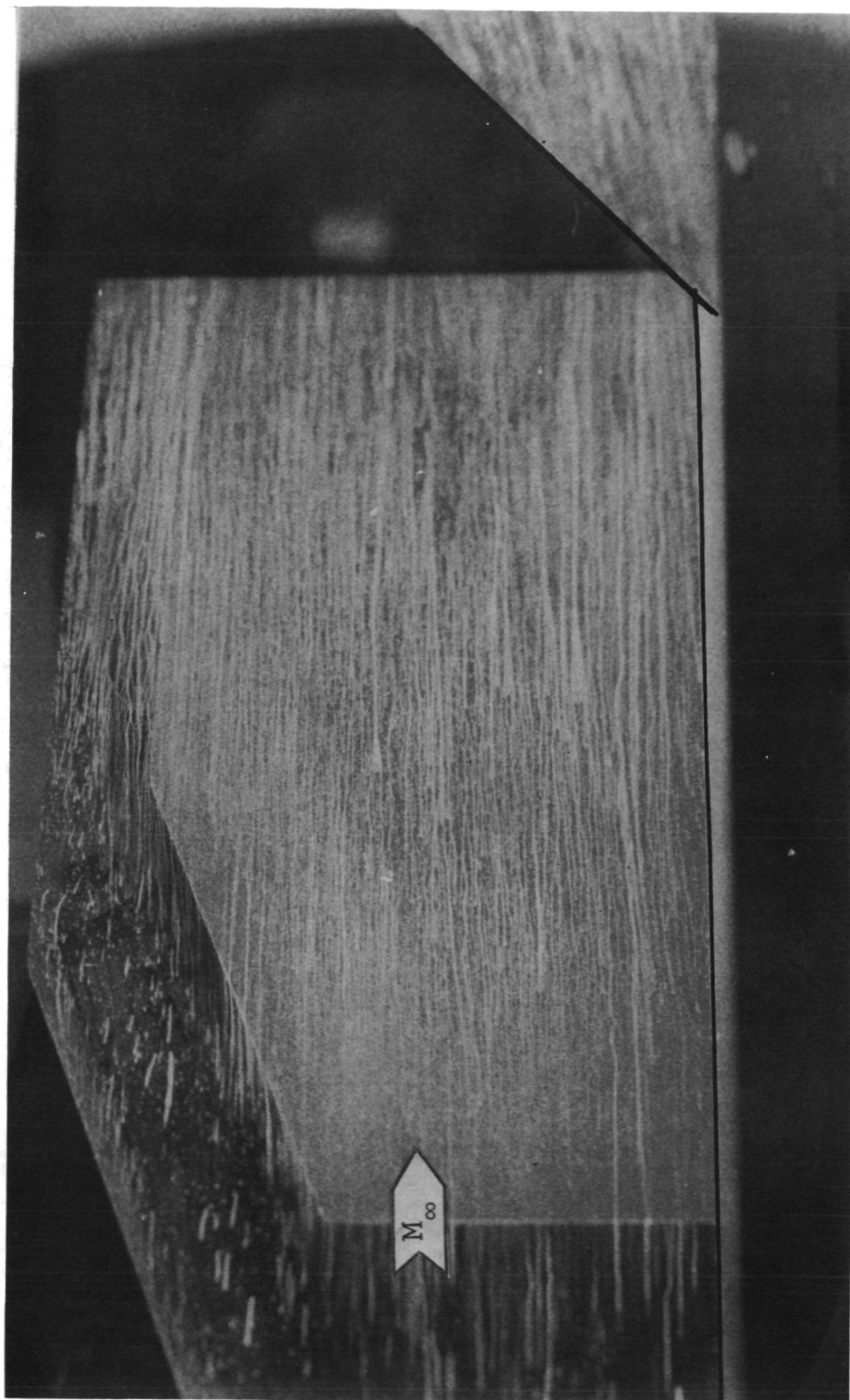


Figure 13.- Frame from profile oil film flow motion picture showing end plate surface.
 $\epsilon = 0^\circ$; $\Lambda = 70^\circ$; large tip plate attached.

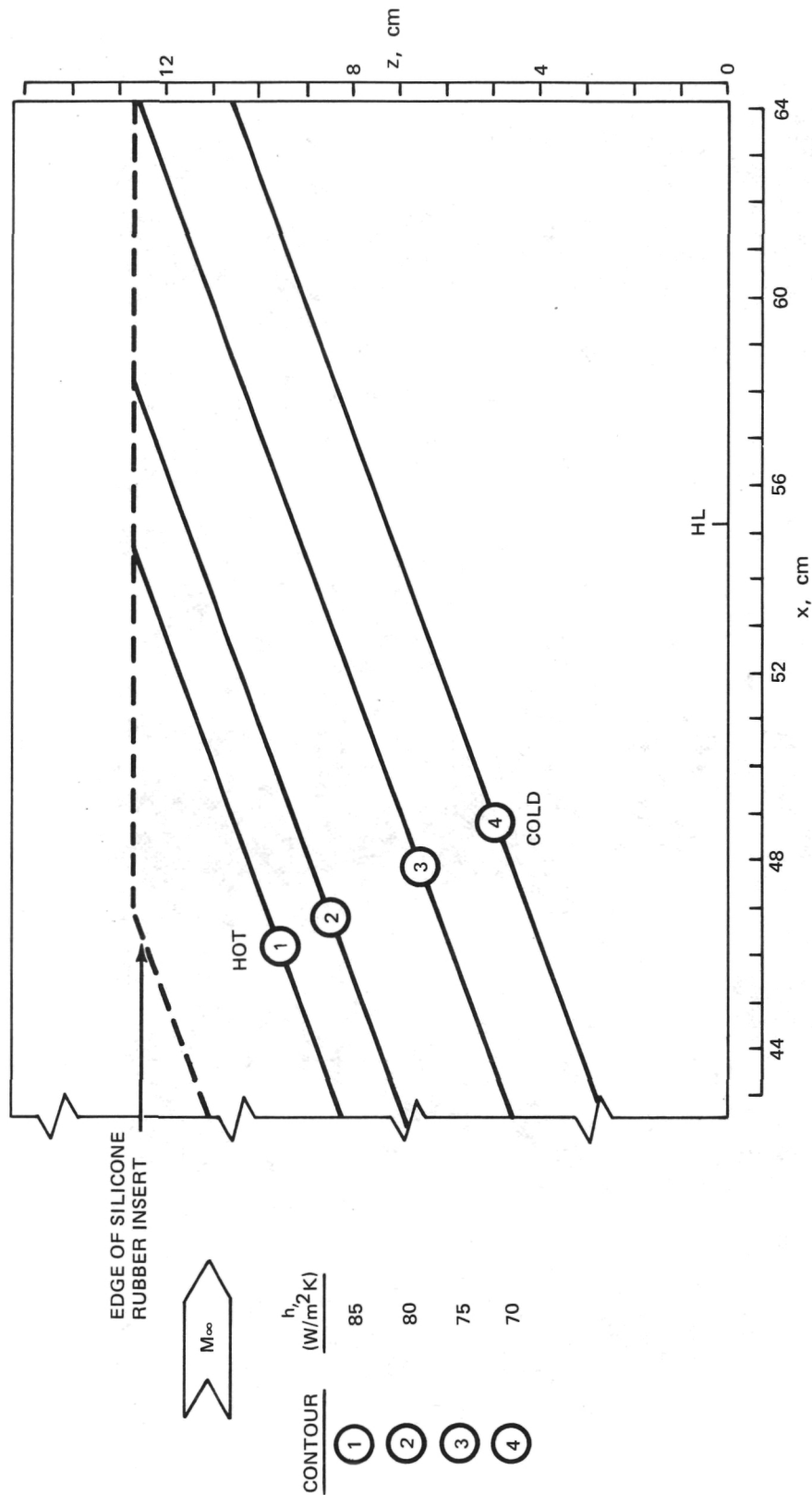


Figure 14.- Constant heat transfer coefficient contours on end plate surface. $\epsilon = 0^\circ$. Contours shown for five configurations: $\Lambda = 0^\circ$ with and without large tip plate, $\Lambda = 50^\circ$ without large tip plate, and $\Lambda = 70^\circ$ with and without large tip plate.

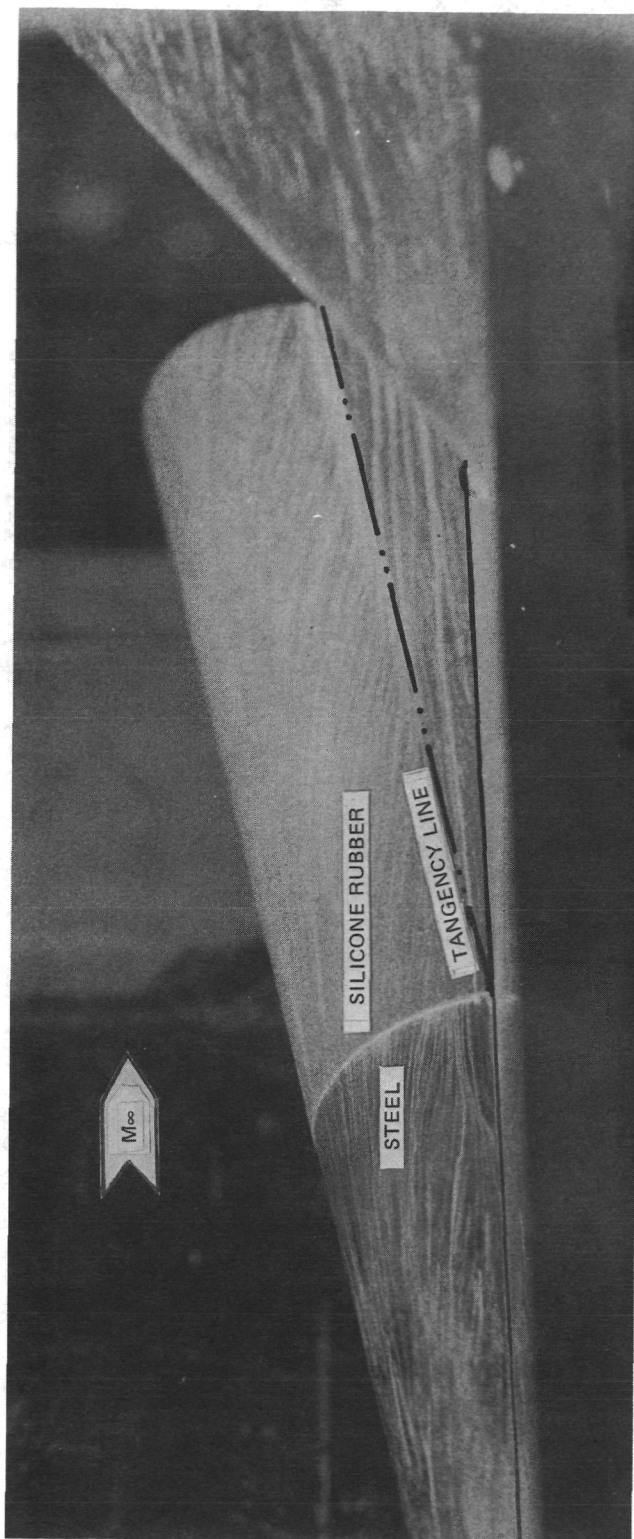
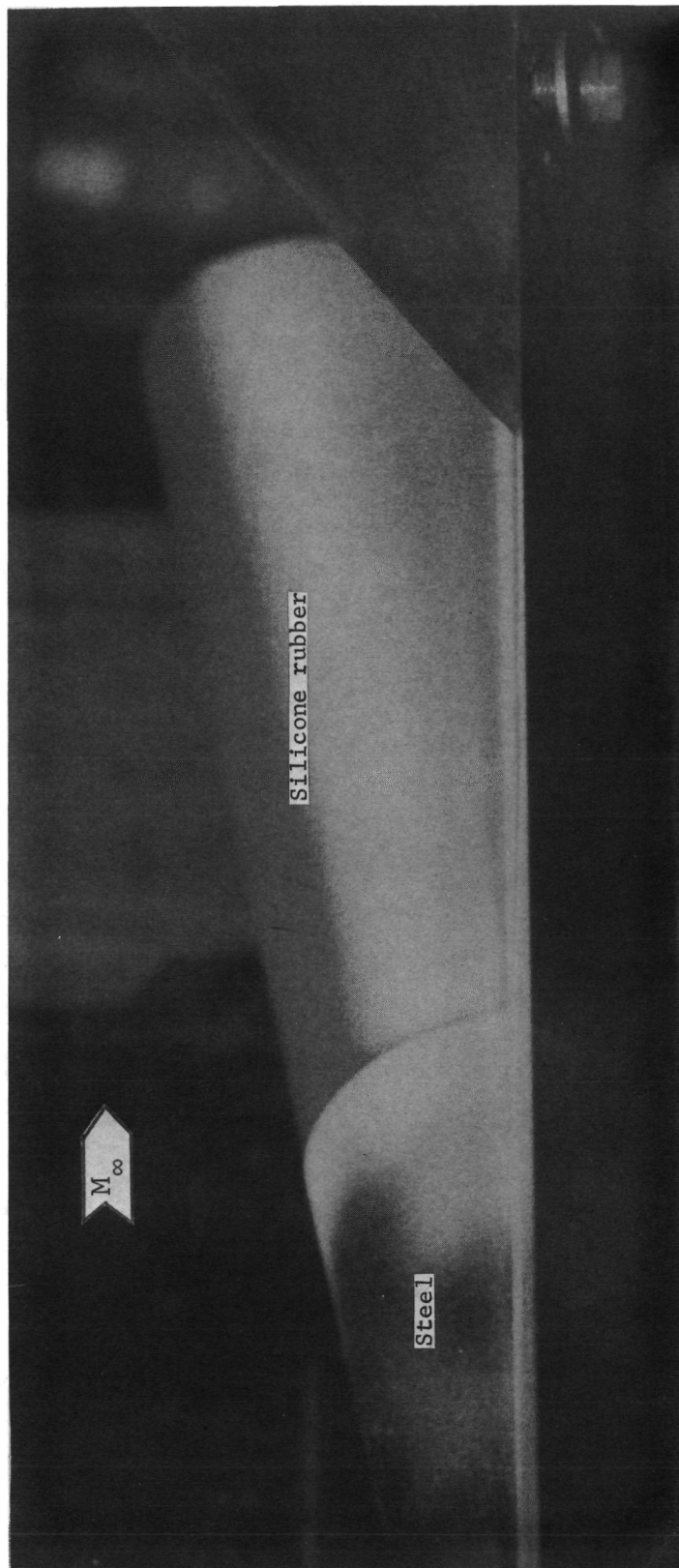


Figure 15.- Frame from profile oil film flow motion picture showing cylindrical body surface. $\epsilon = 0^\circ$; $\Lambda = 70^\circ$; large tip fin attached.

L-78-53



L-78-54

Figure 16.- Frame from profile phase change paint motion picture showing cylindrical body surface. $\epsilon = 0^\circ$; $\Lambda = 70^\circ$; large tip fin attached.

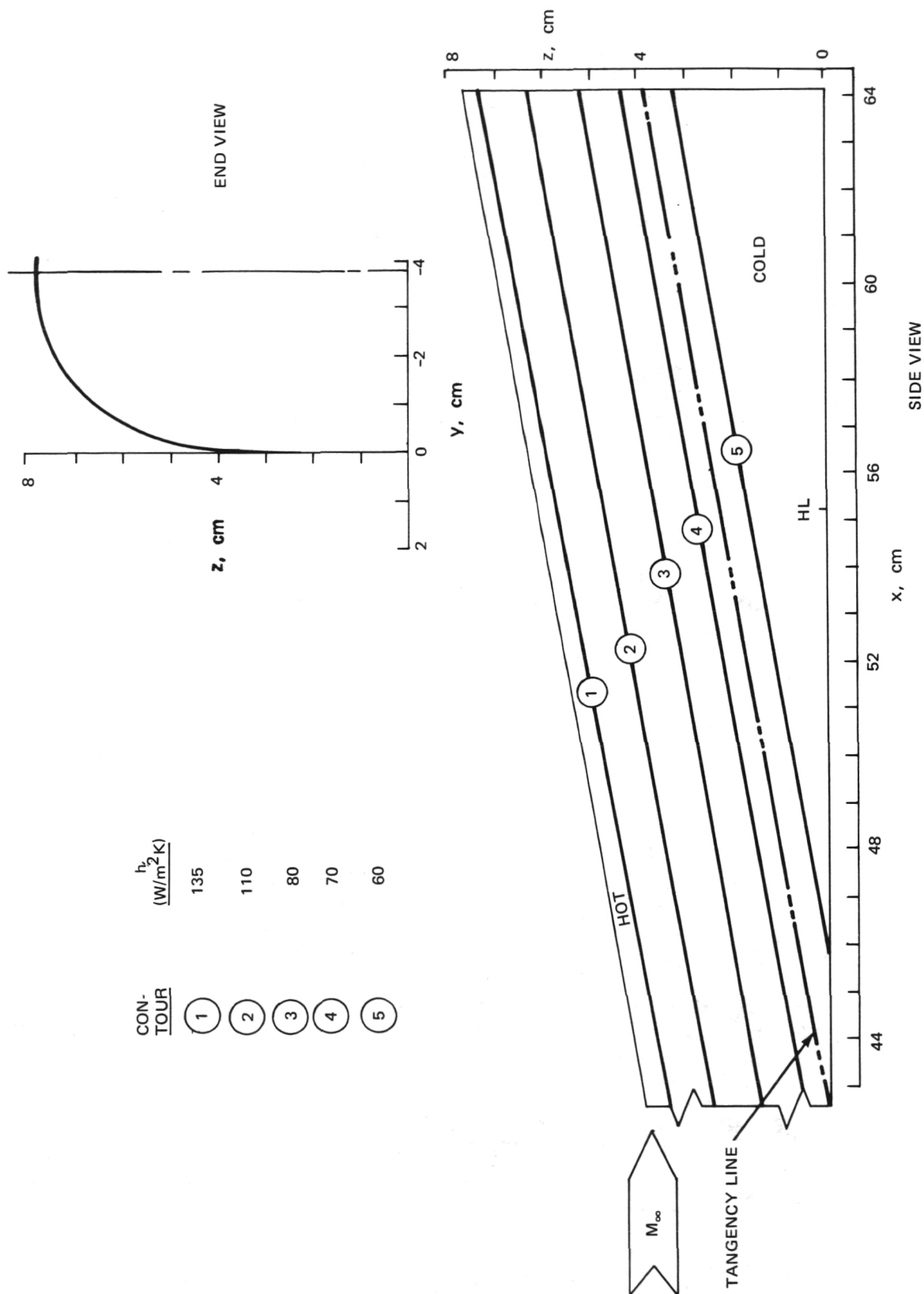


Figure 17.- Constant heat transfer coefficient contours on cylindrical body surface. $\epsilon = 0^\circ$ and $\Lambda = 70^\circ$. Contours shown for two configurations: with and without large tip fin.

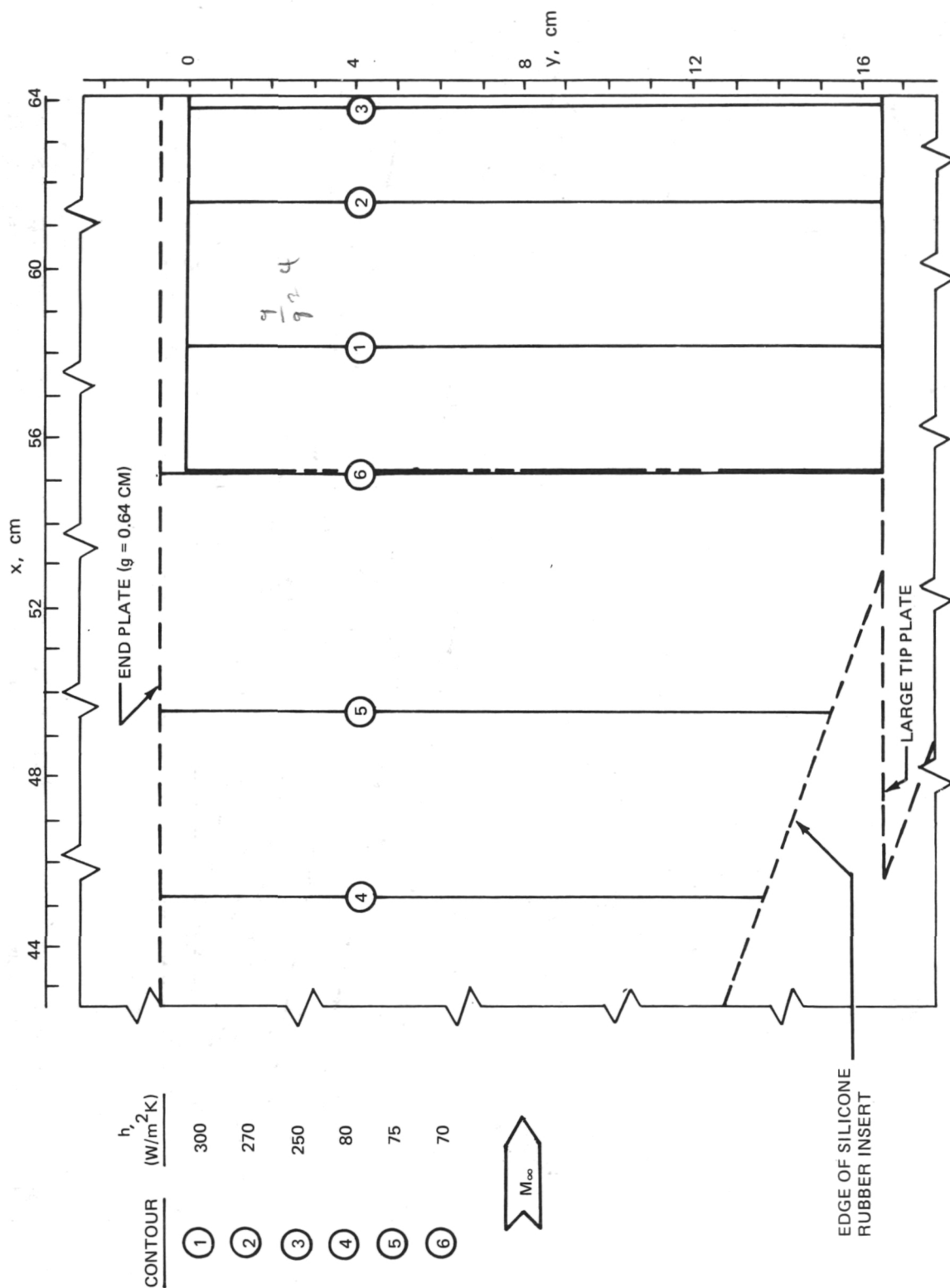


Figure 18.- Constant heat transfer coefficient contours on wing and elevon surfaces. $\epsilon = 10^\circ$ and $\Lambda = 0^\circ$. Contours shown for three configurations: with no attachments, with large tip plate, and with end plate with gap.

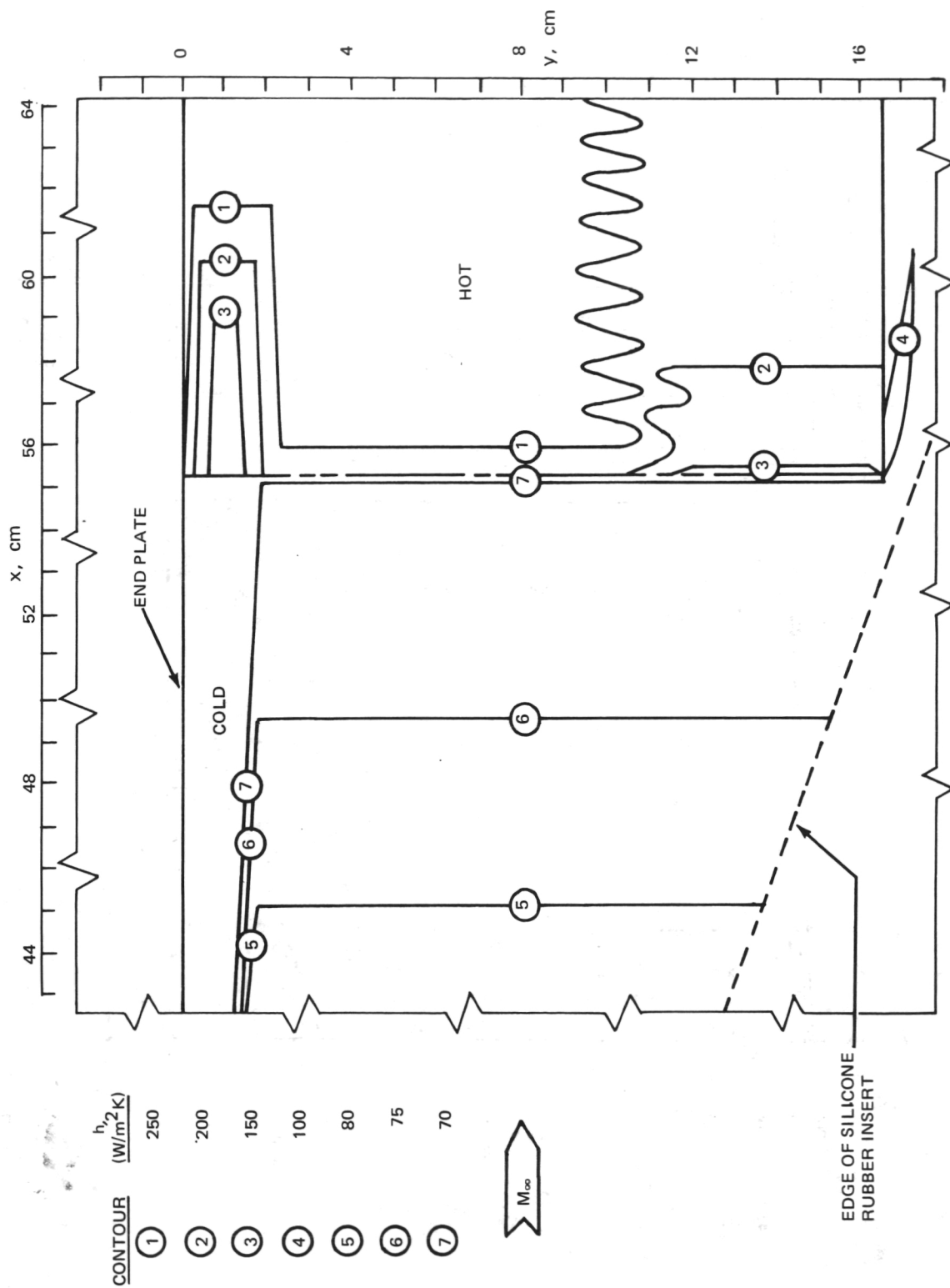


Figure 19.- Constant heat transfer coefficient contours on wing and elevon surfaces.
 $\epsilon = 10^\circ$; $\Lambda = 0^\circ$; end plate attached.

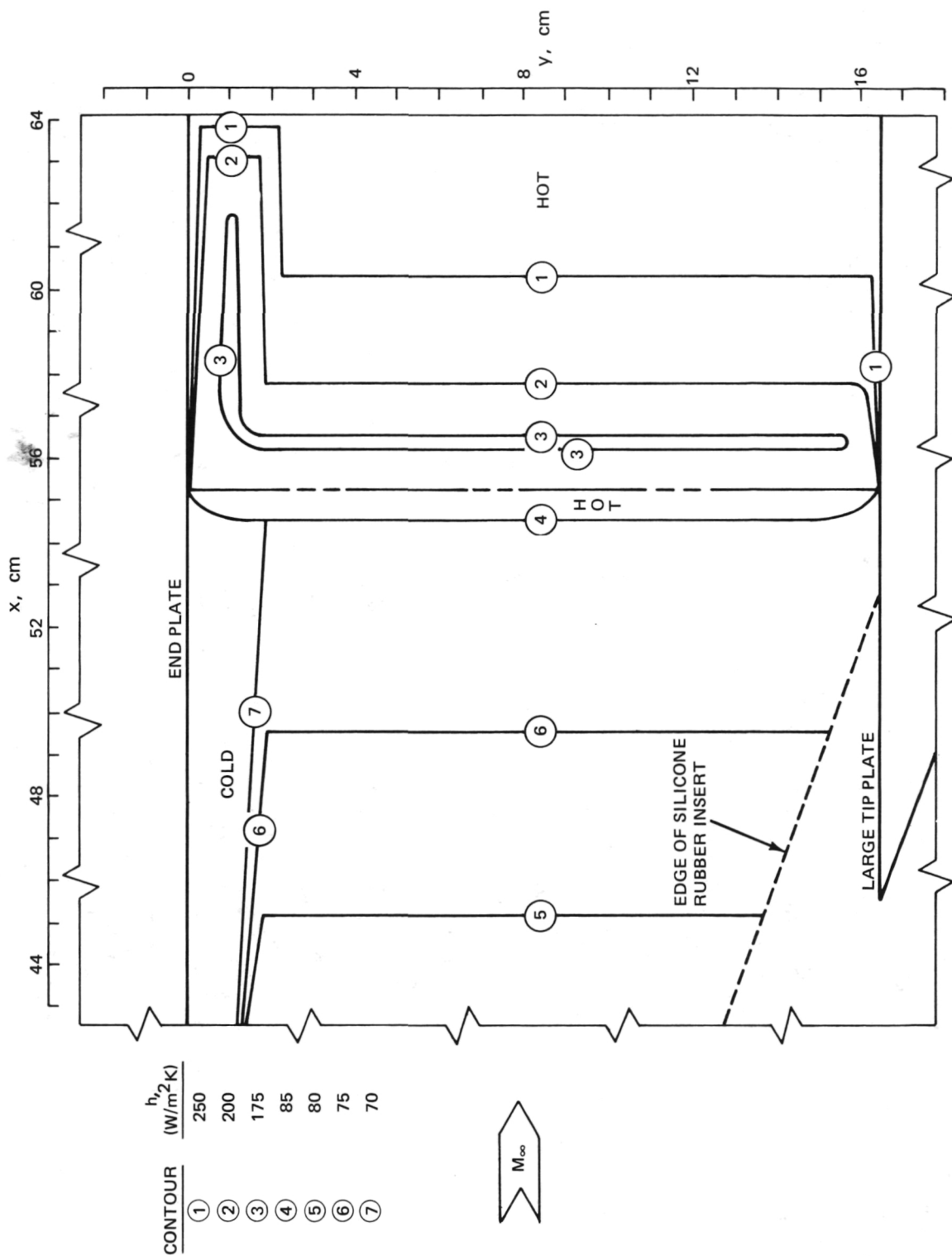


Figure 20.- Constant heat transfer coefficient contours on wing and elevator surfaces.
 $\epsilon = 10^\circ$; $\Lambda = 0^\circ$; end plate and large tip plate attached.

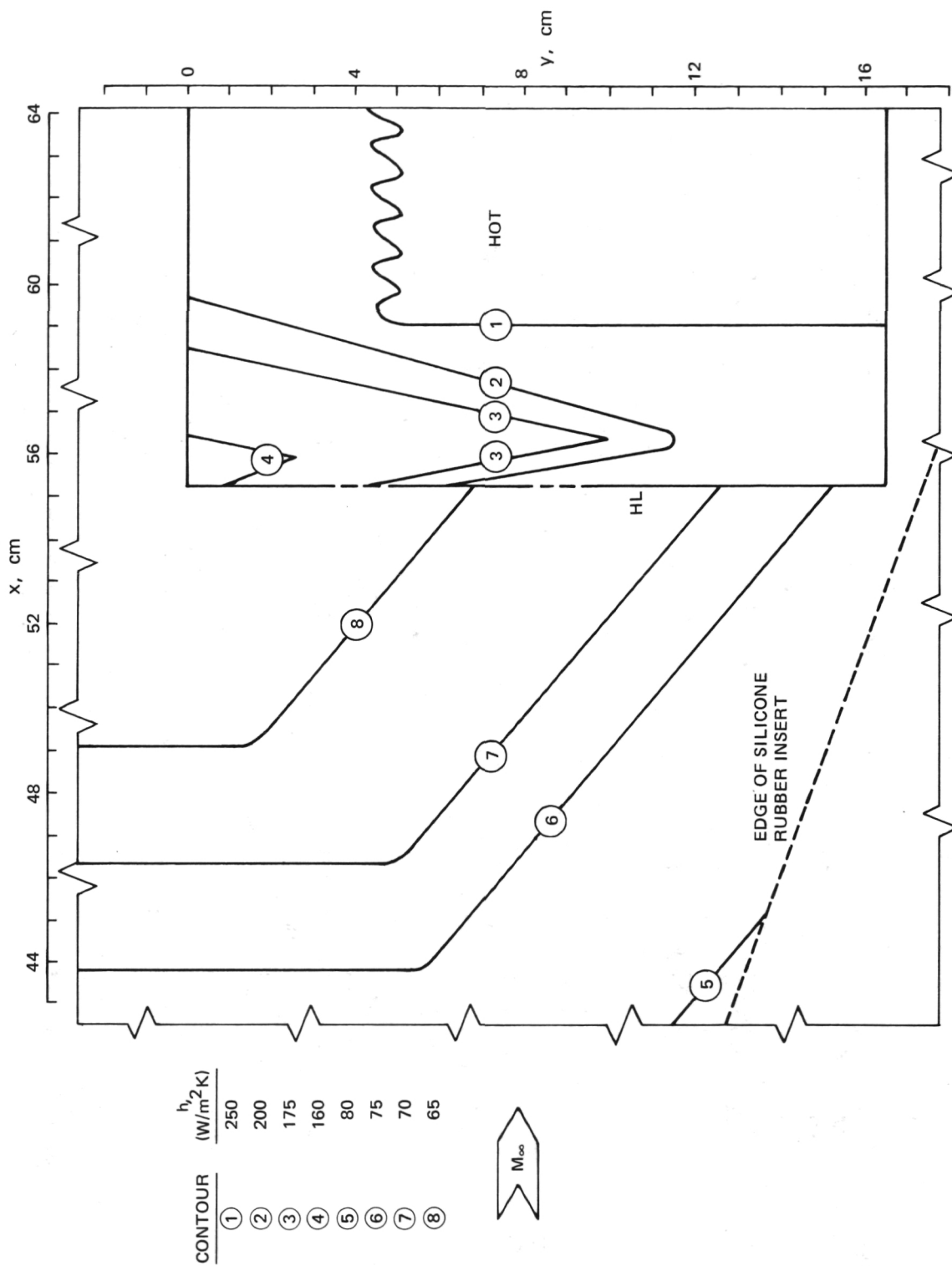


Figure 21.- Constant heat transfer coefficient contours on wing and elevon surfaces.
 $\epsilon = 10^\circ$ and $\Lambda = 50^\circ$.

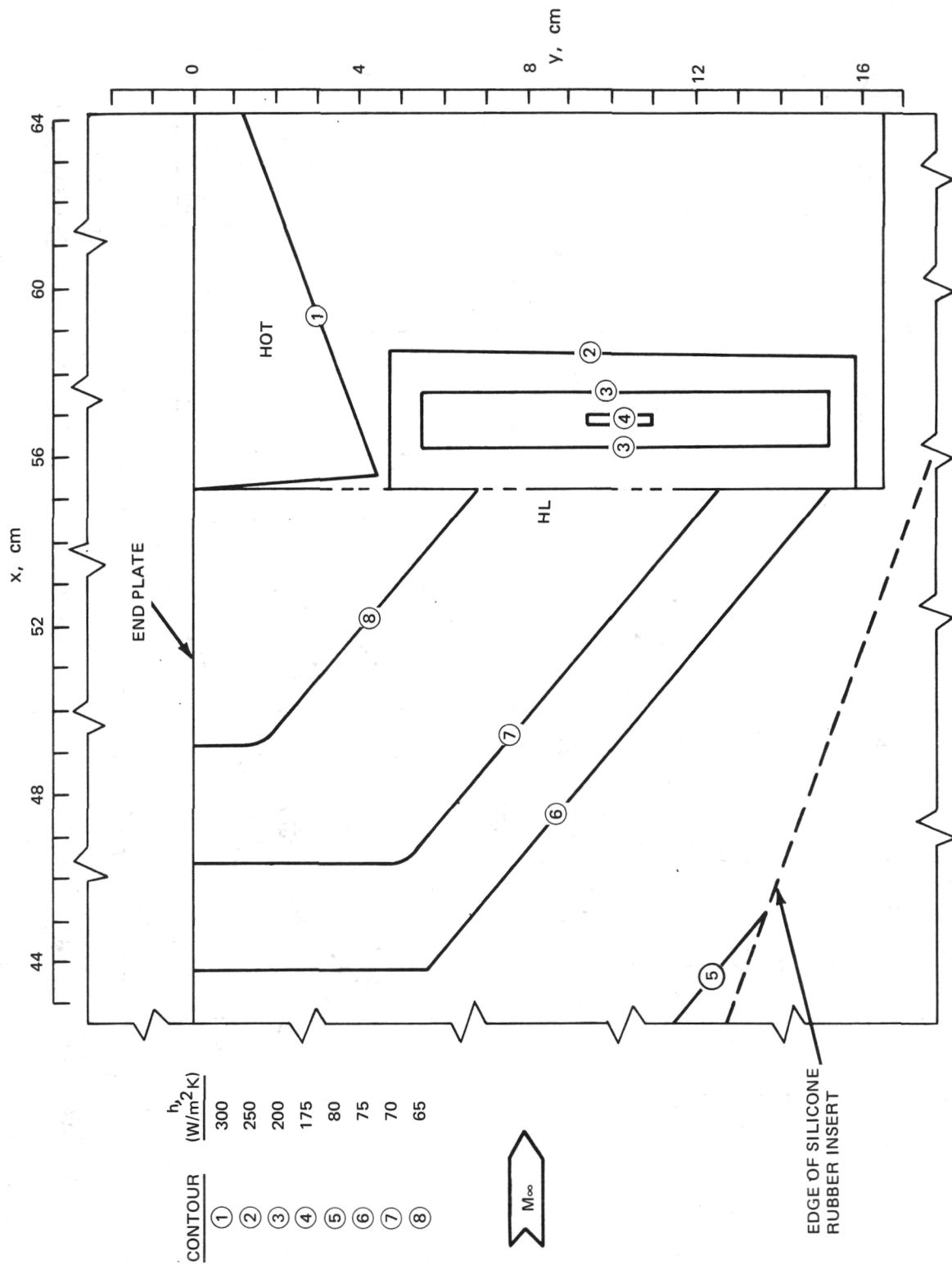


Figure 22.- Constant heat transfer coefficient contours on wing and elevon surfaces.
 $\epsilon = 10^\circ$; $\Lambda = 50^\circ$; end plate attached.

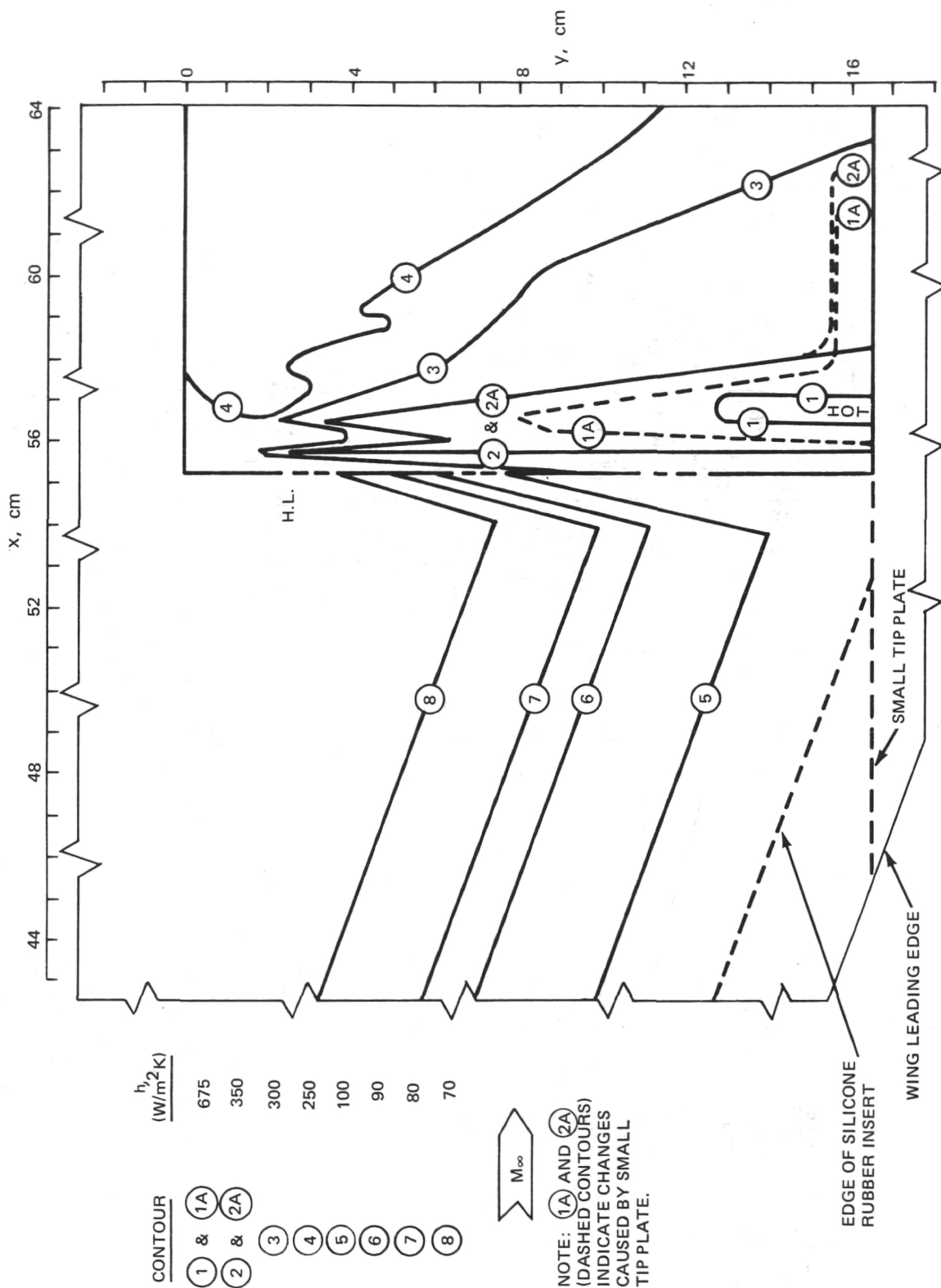


Figure 23.- Constant heat transfer coefficient contours on wing and elevon surfaces. $\epsilon = 10^\circ$ and $\lambda = 70^\circ$. Contours shown for two configurations: with and without small tip plate.

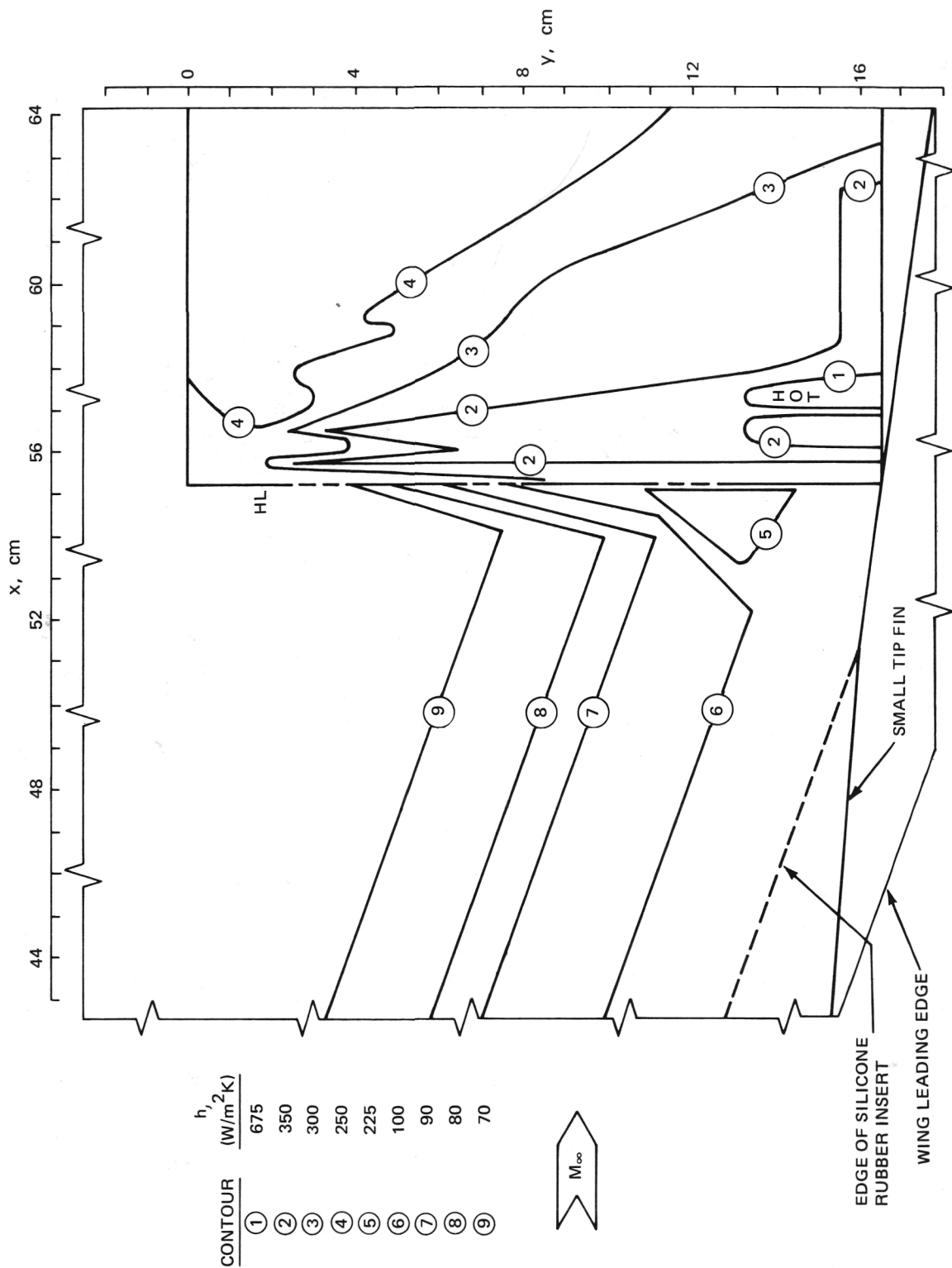


Figure 24.- Constant heat transfer coefficient contours on wing and elevon surfaces.
 $\epsilon = 10^\circ$; $\Lambda = 70^\circ$; small tip fin attached.

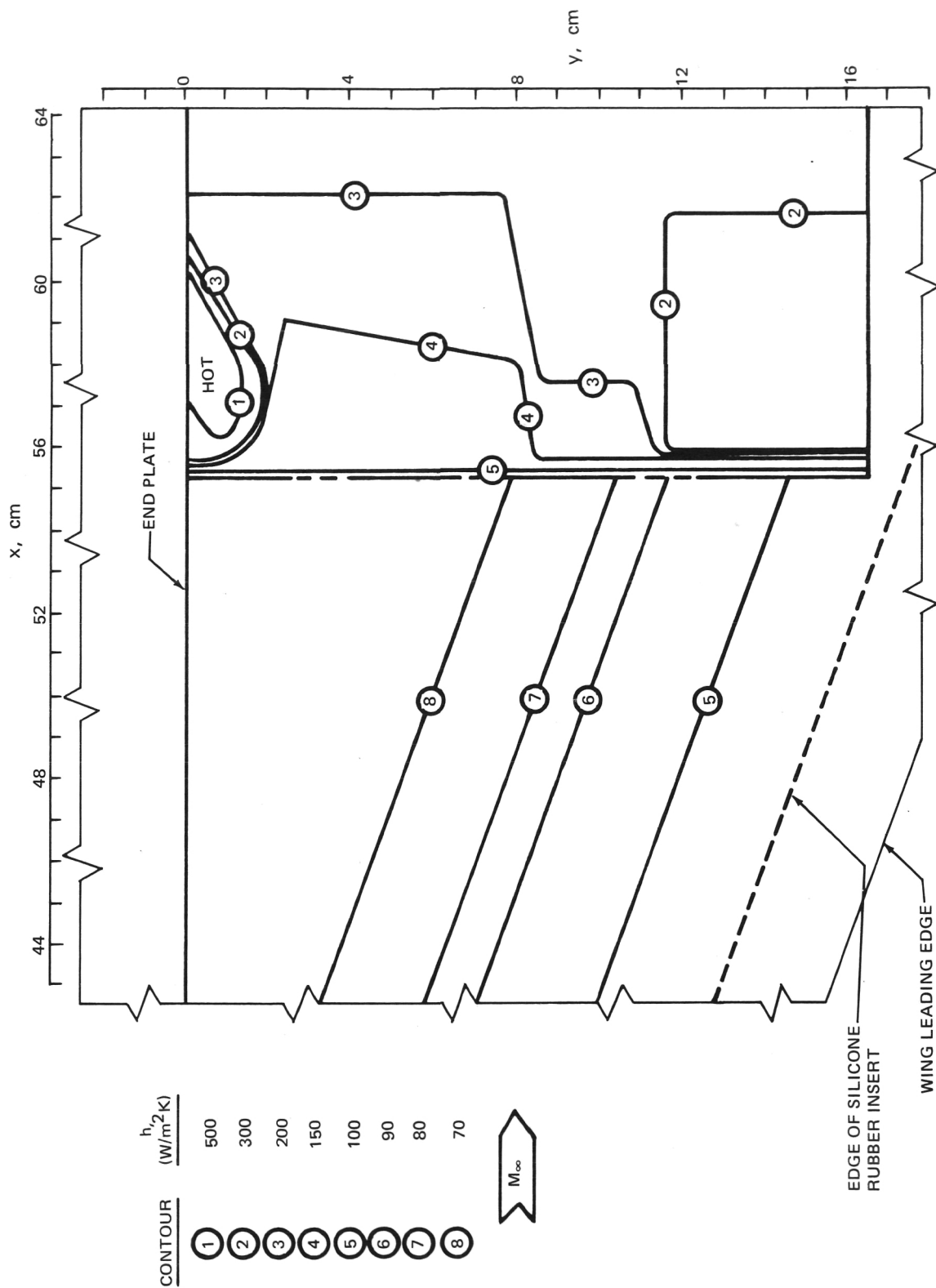
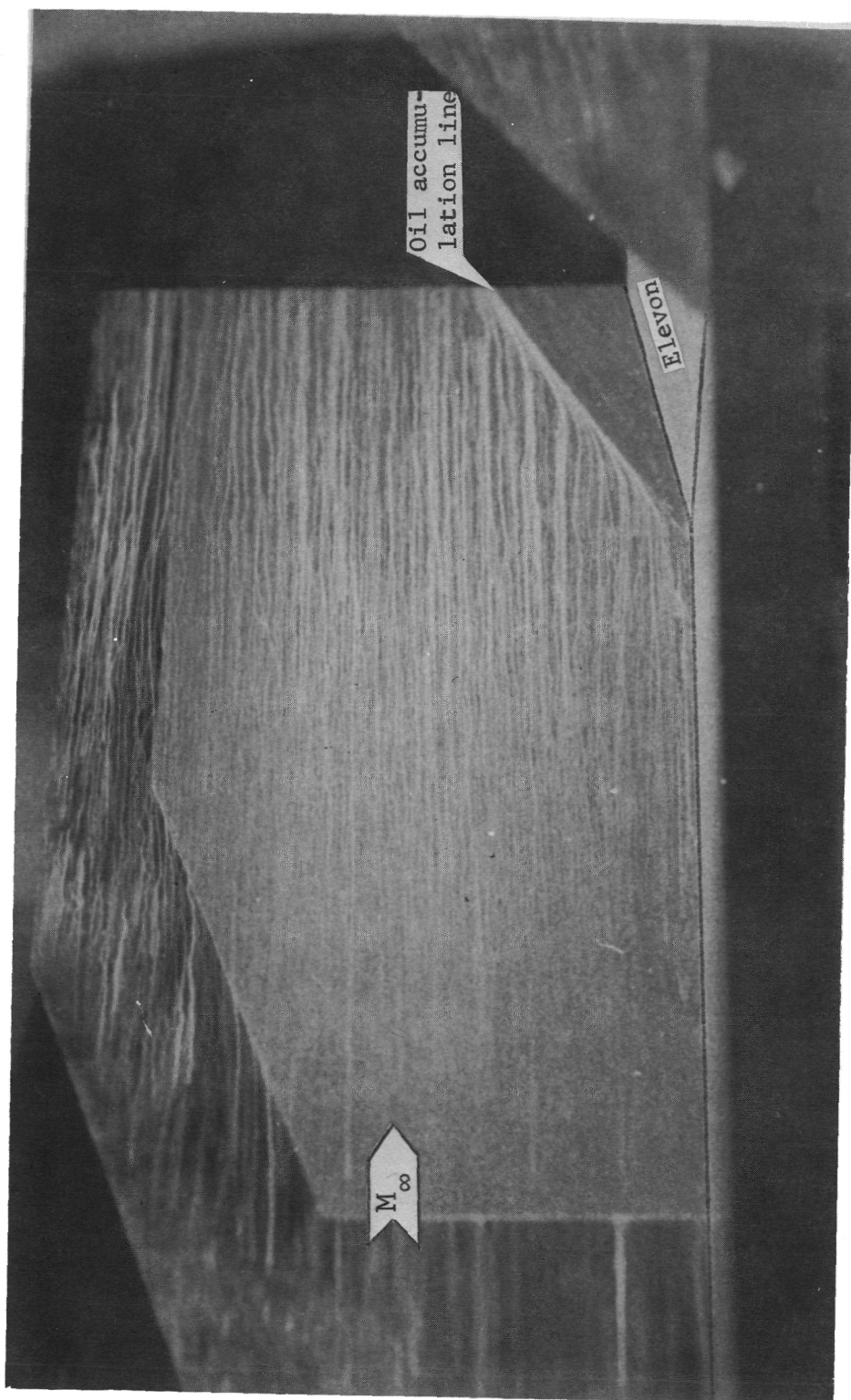


Figure 25.- Constant heat transfer coefficient contours on wing and elevon surfaces.
 $\epsilon = 10^\circ$; $\Lambda = 70^\circ$; end plate attached.



L-78-55

Figure 28.- Frame from profile oil film flow motion picture showing end plate surface. $\epsilon = 10^\circ$; $\Lambda = 70^\circ$; large tip plate attached.

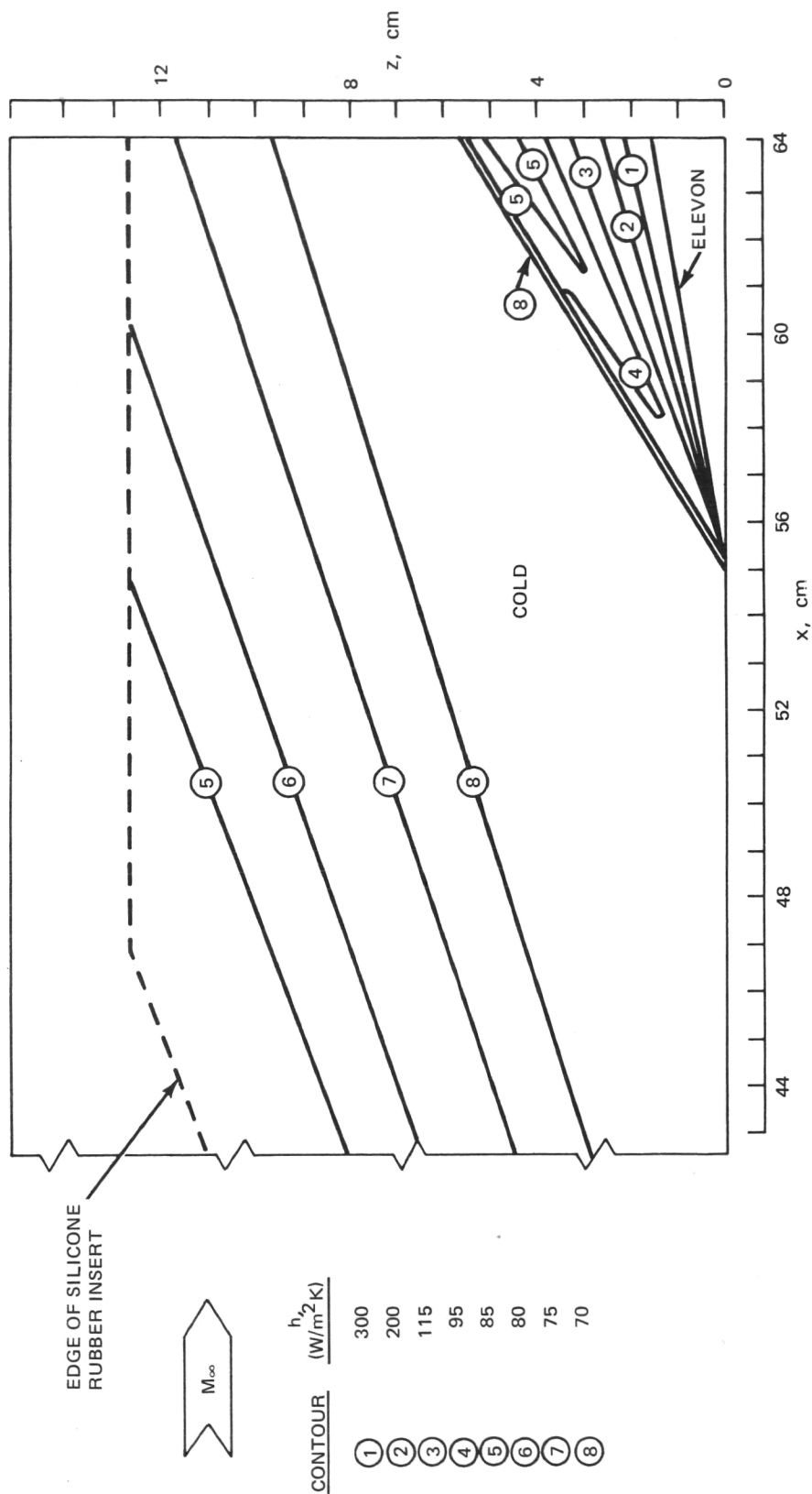


Figure 29.- Constant heat transfer coefficient contours on end plate surface. $\varepsilon = 10^\circ$. Contours shown for five configurations: $\Lambda = 0^\circ$ with and without large tip plate, $\Lambda = 50^\circ$ without large tip plate, and $\Lambda = 70^\circ$ with and without large tip plate.

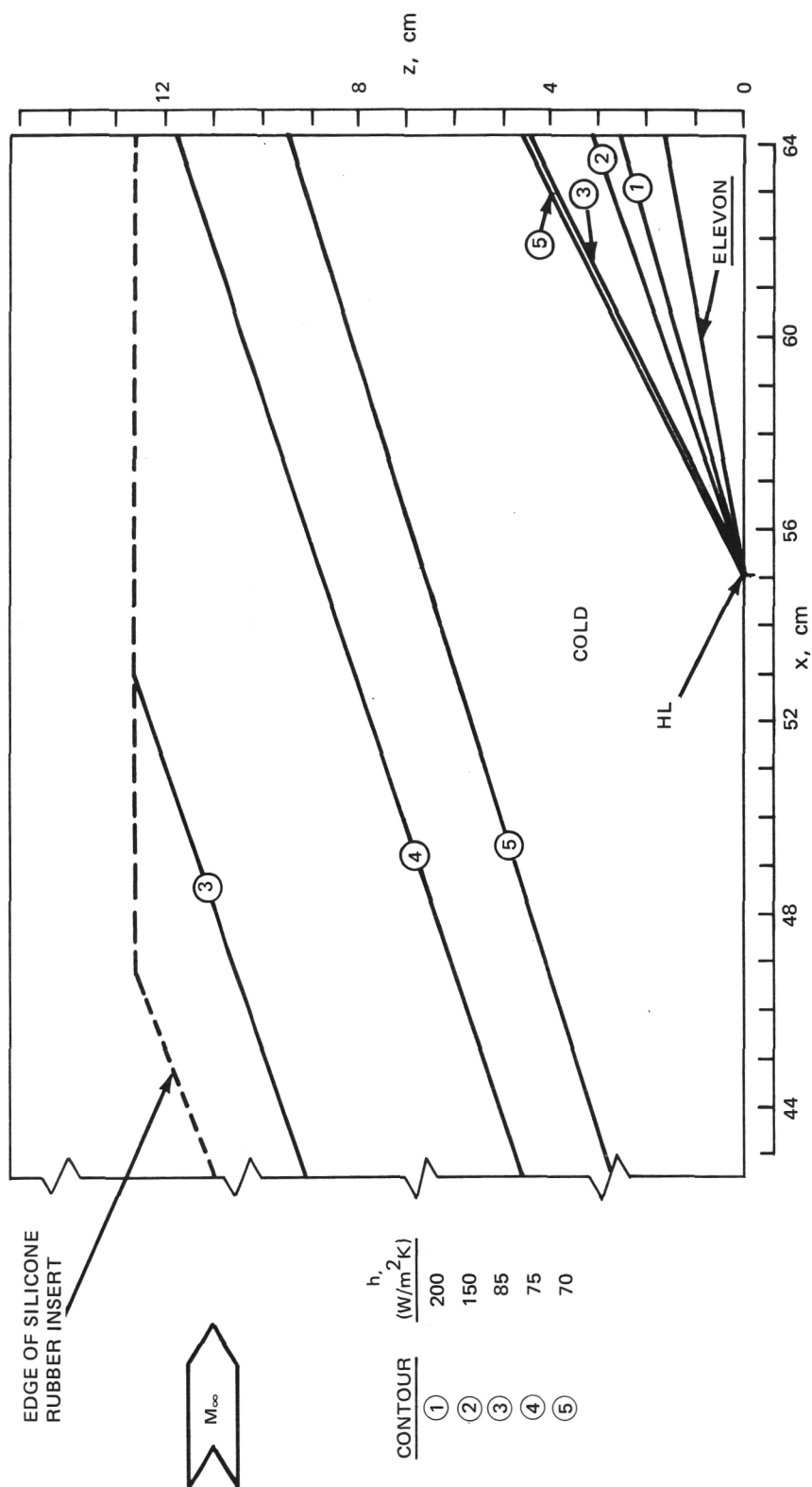
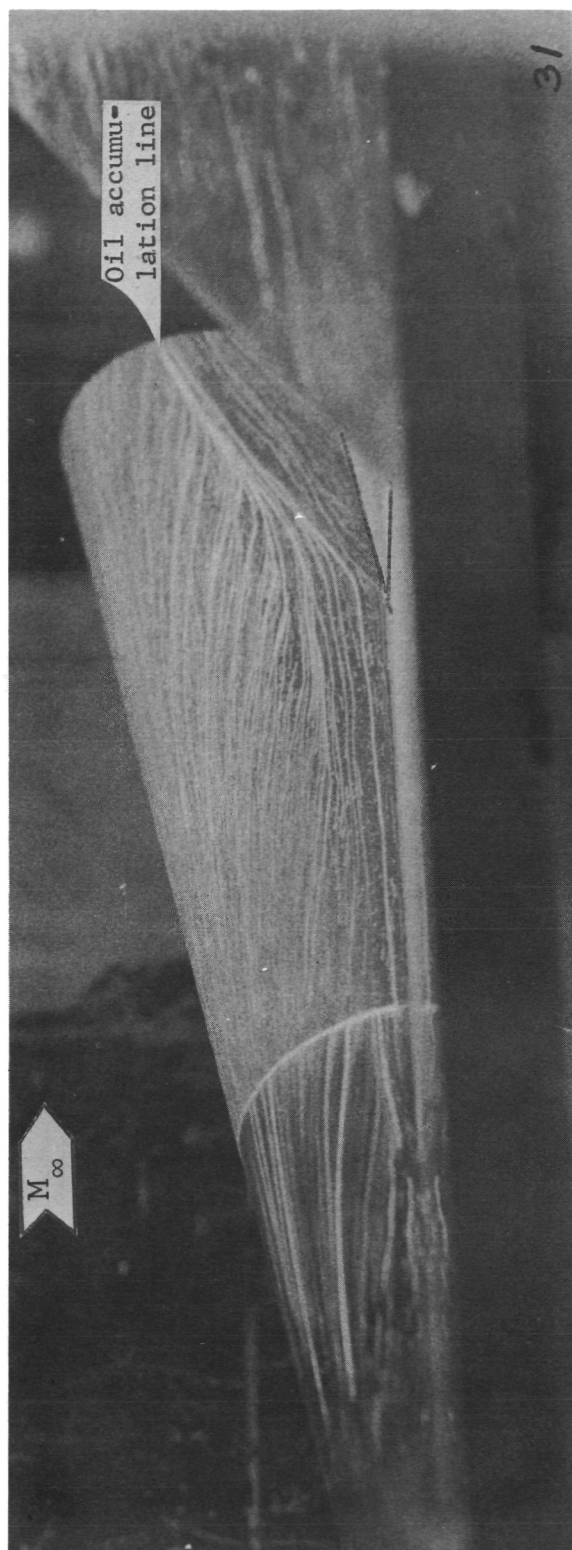


Figure 30.- Constant heat transfer coefficient contours on end plate surface. $\epsilon = 10^\circ$; 0.64-cm gap between end plate and elevon. Contours shown for two configurations: $\Lambda = 0^\circ$ without large tip plate and $\Lambda = 70^\circ$ with large tip plate.



L-78-56

Figure 31.- Frame from profile oil film flow motion picture showing cylindrical body surface. $\epsilon = 10^\circ$; $\Lambda = 70^\circ$; large tip fin attached.

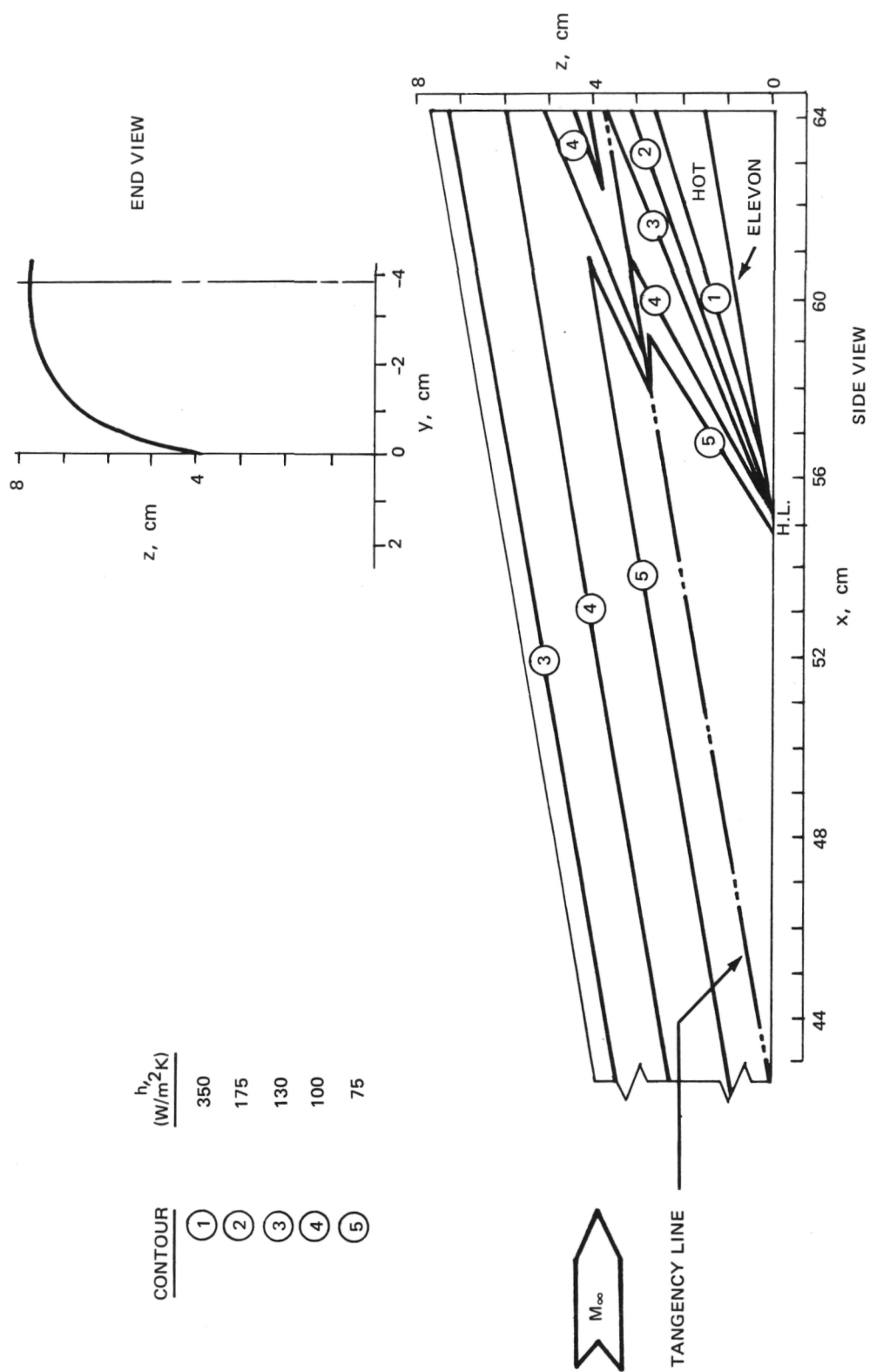


Figure 32.- Constant heat transfer coefficient contours on cylindrical body surface. $\epsilon = 10^\circ$ and $\Lambda = 70^\circ$. Contours shown for two configurations: with and without large tip fin.

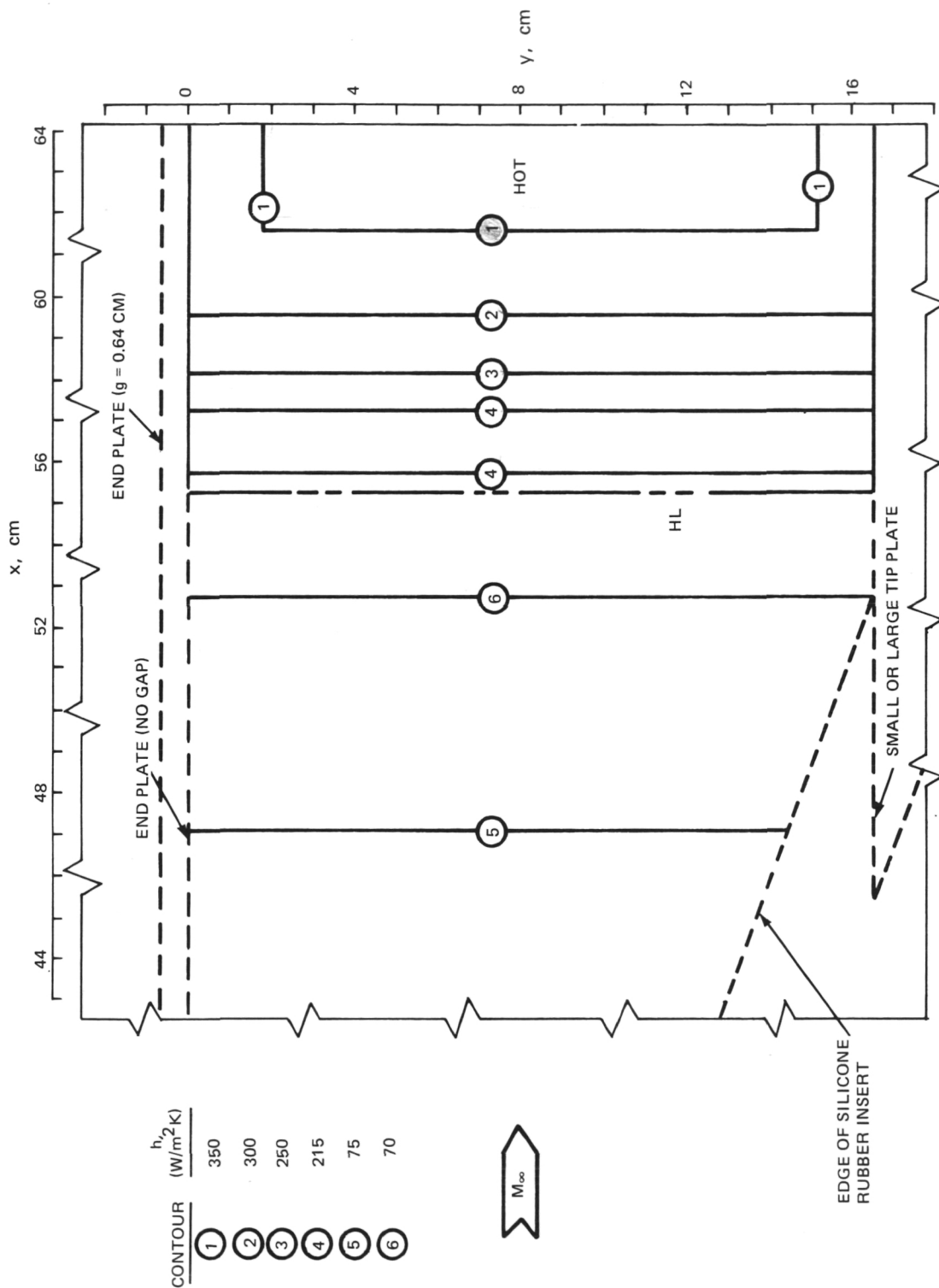


Figure 33.- Constant heat transfer coefficient contours on wing and elevon surfaces. $\epsilon = 20^\circ$ and $\Lambda = 0^\circ$. Contours shown for six configurations: with no attachment, with small tip plate, with large tip plate, with end plate ($g = 0$ cm), with end plate ($g = 0.64$ cm), and with end tip plate and large tip plate.

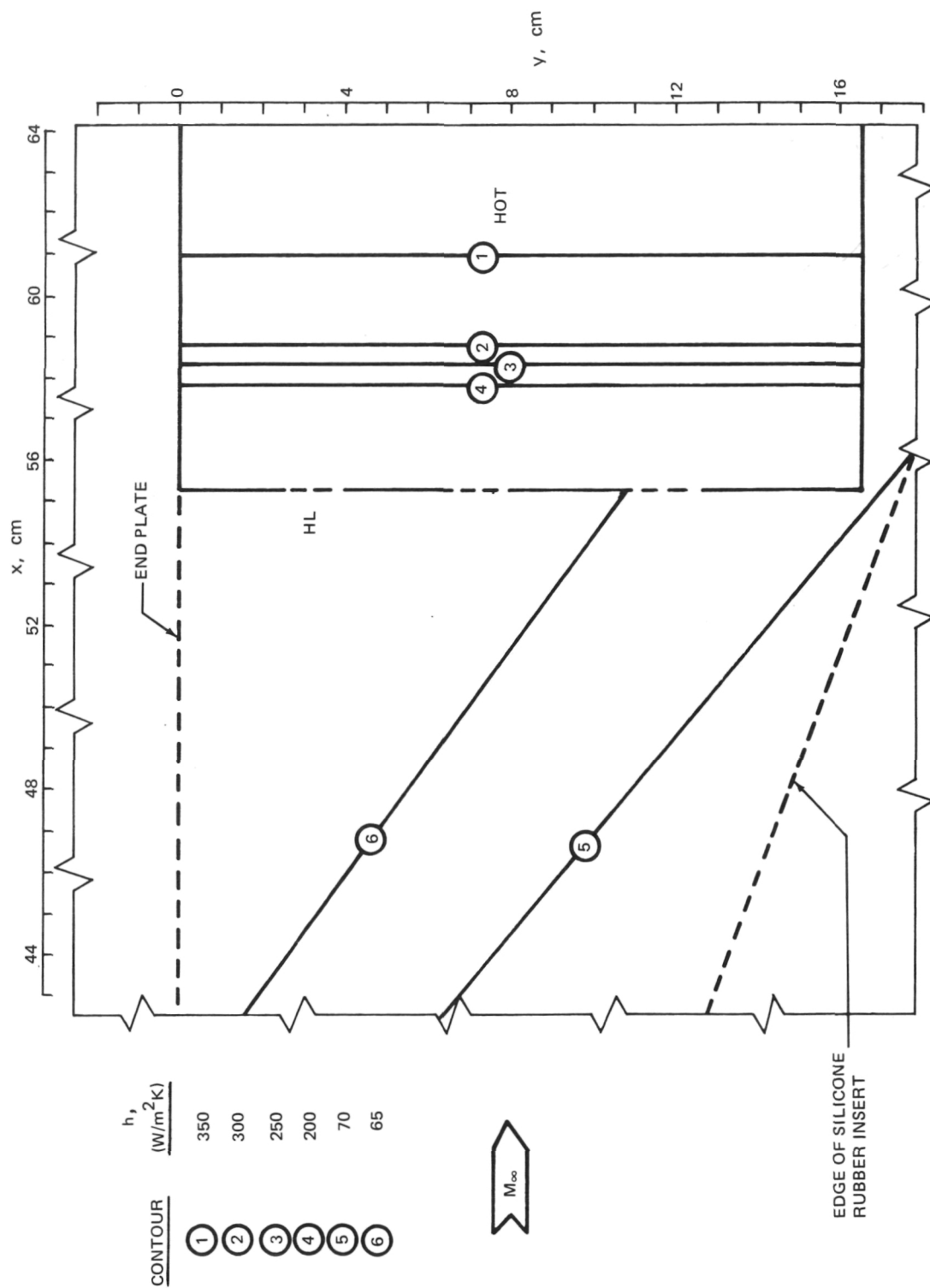


Figure 34.- Constant heat transfer coefficient contours on wing and elevator surfaces. $\epsilon = 20^\circ$ and $\Lambda = 50^\circ$. Contours shown for two configurations: with and without end plate.

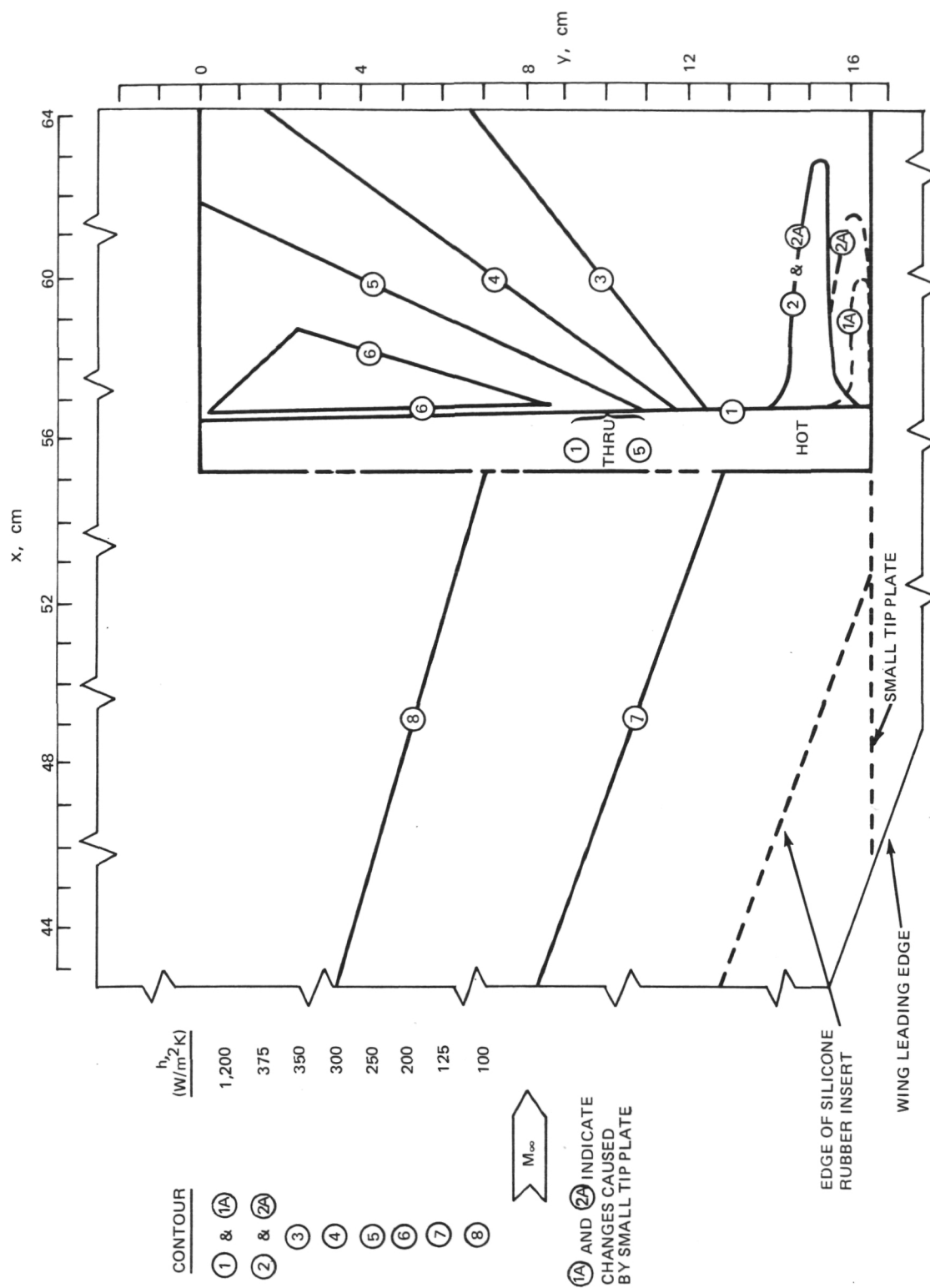


Figure 35.- Constant heat transfer coefficient contours on wing and elevator surfaces. $\epsilon = 20^\circ$ and $\Lambda = 70^\circ$. Contours shown for two configurations: with and without small tip plate. 1A and 2A indicate changes caused by small tip plate.

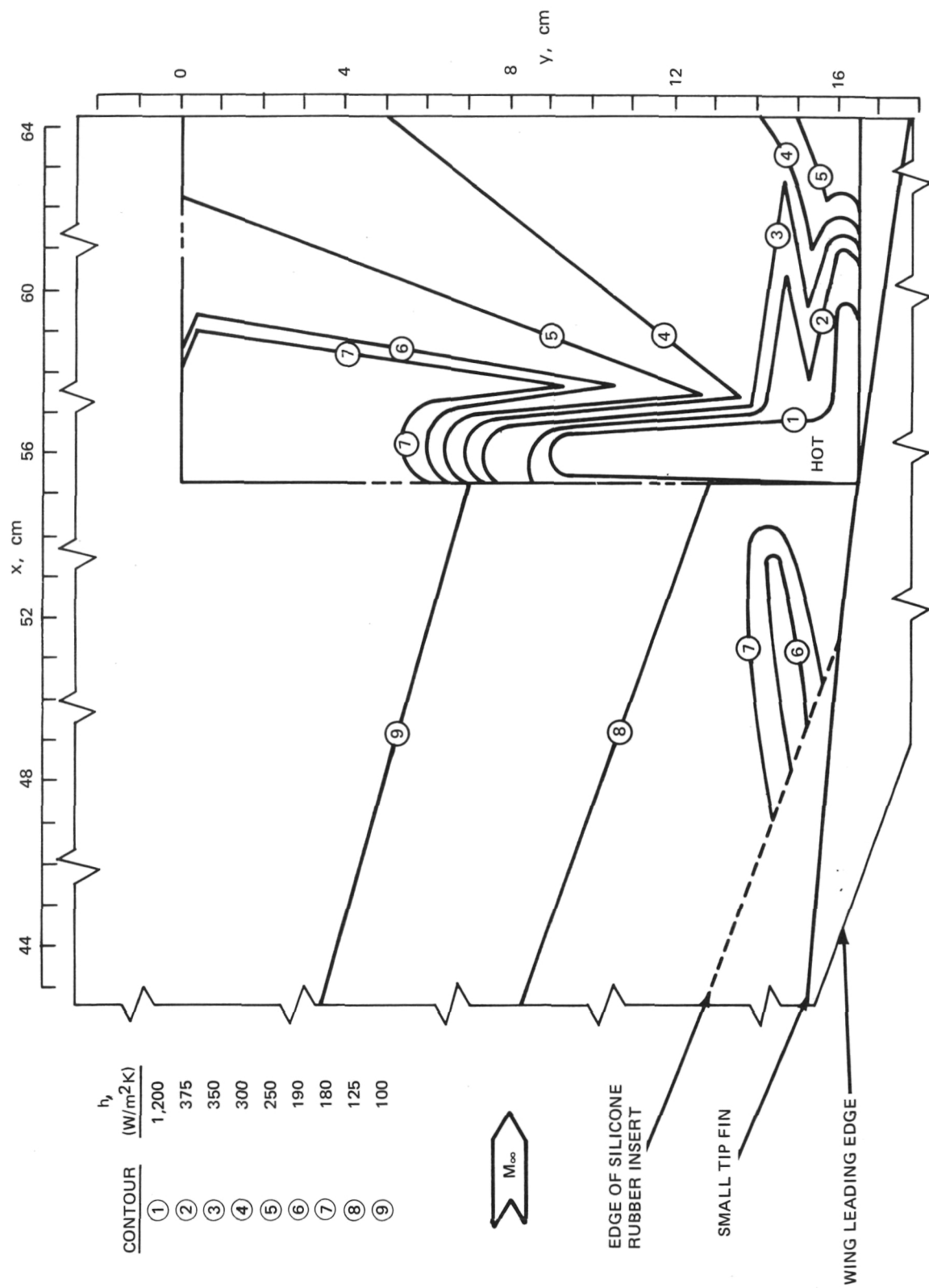


Figure 36.- Constant heat transfer coefficient contours on wing and elevator surfaces.
 $\epsilon = 20^\circ$; $\Lambda = 70^\circ$; with small tip fin.

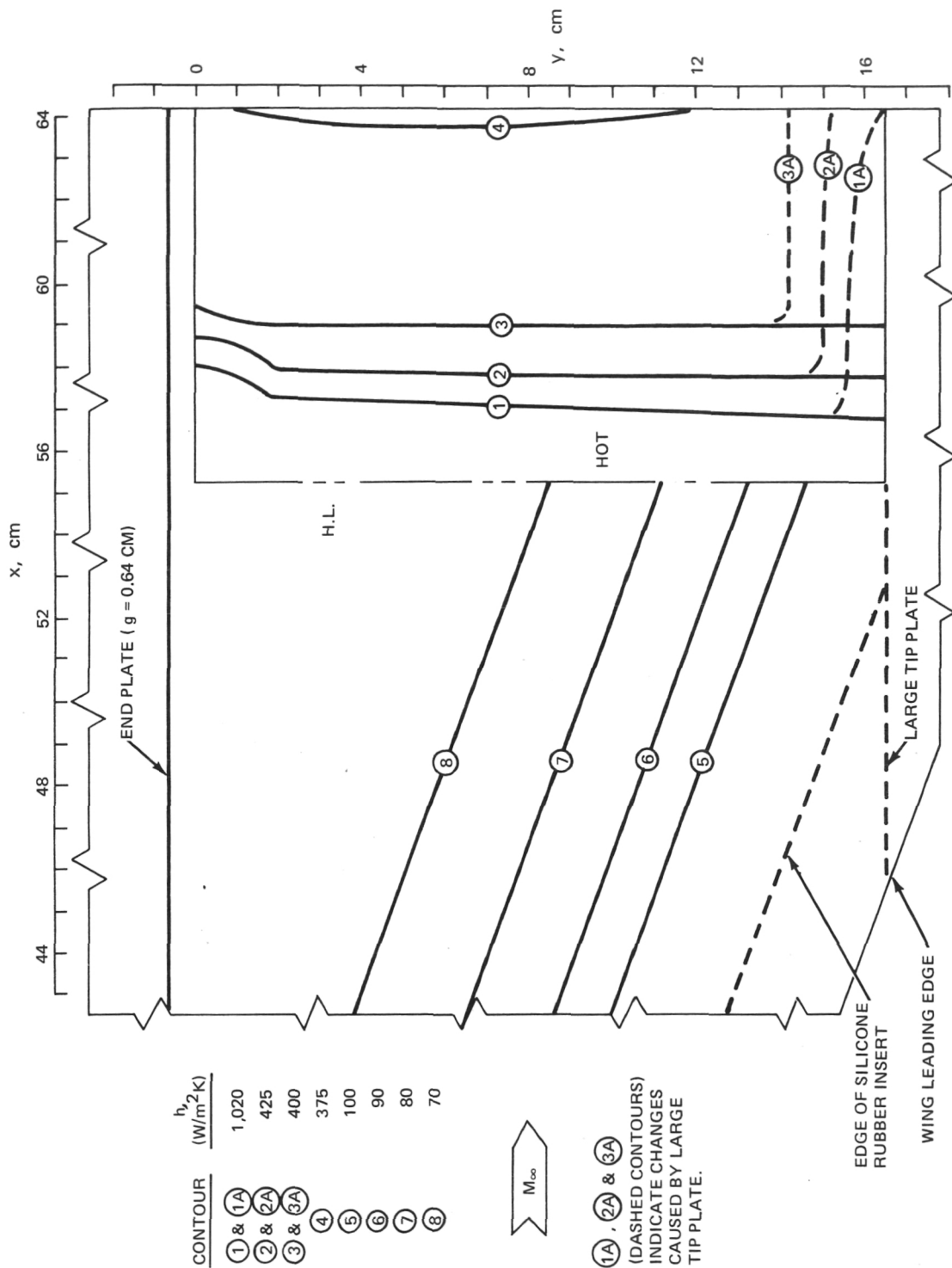


Figure 37.- Constant heat transfer coefficient contours on wing and elevon surfaces.
 $\varepsilon = 20^\circ$; $\Lambda = 70^\circ$; end plate attached with 0.64-cm gap between end plate and elevon.
 Contours shown for two configurations: with and without large tip plate.

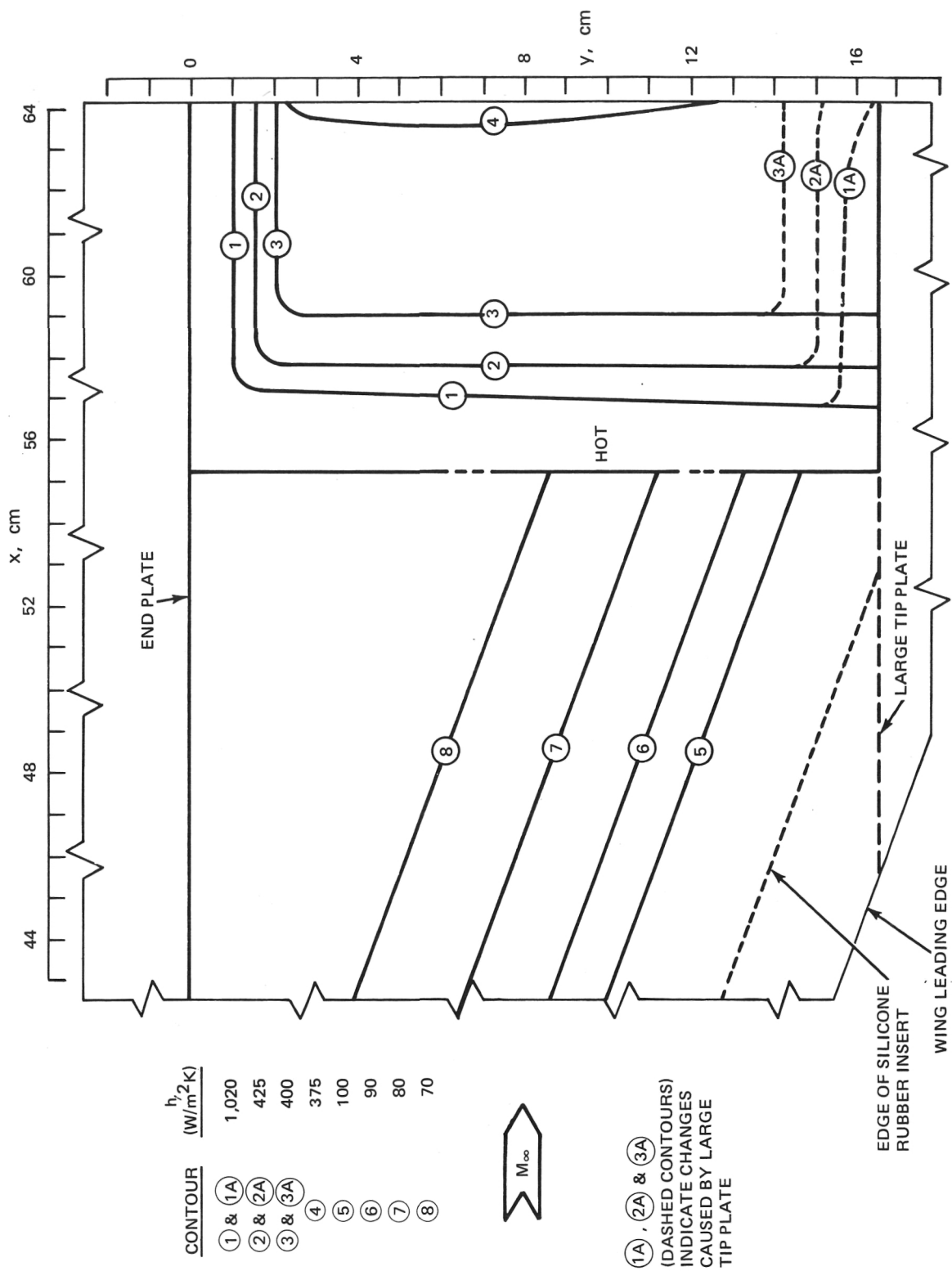


Figure 38.- Constant heat transfer coefficient contours on wing and elevon surfaces. $\epsilon = 20^\circ$; $\Lambda = 70^\circ$; end plate attached. Contours shown for two configurations: with and without large tip plate.

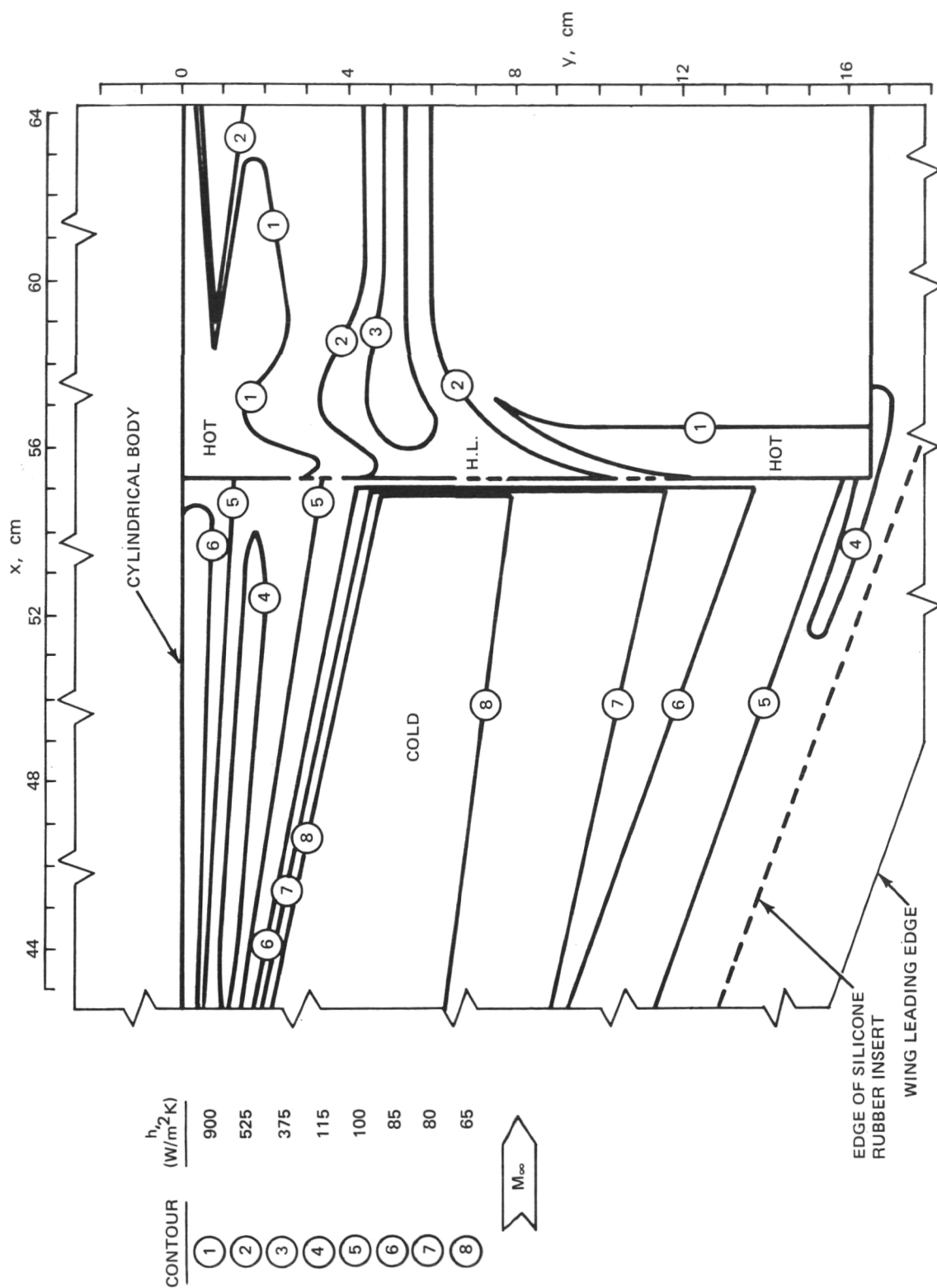


Figure 39.- Constant heat transfer coefficient contours on wing and elevon surfaces. $\epsilon = 20^\circ$; $\Lambda = 70^\circ$; cylindrical body attached.

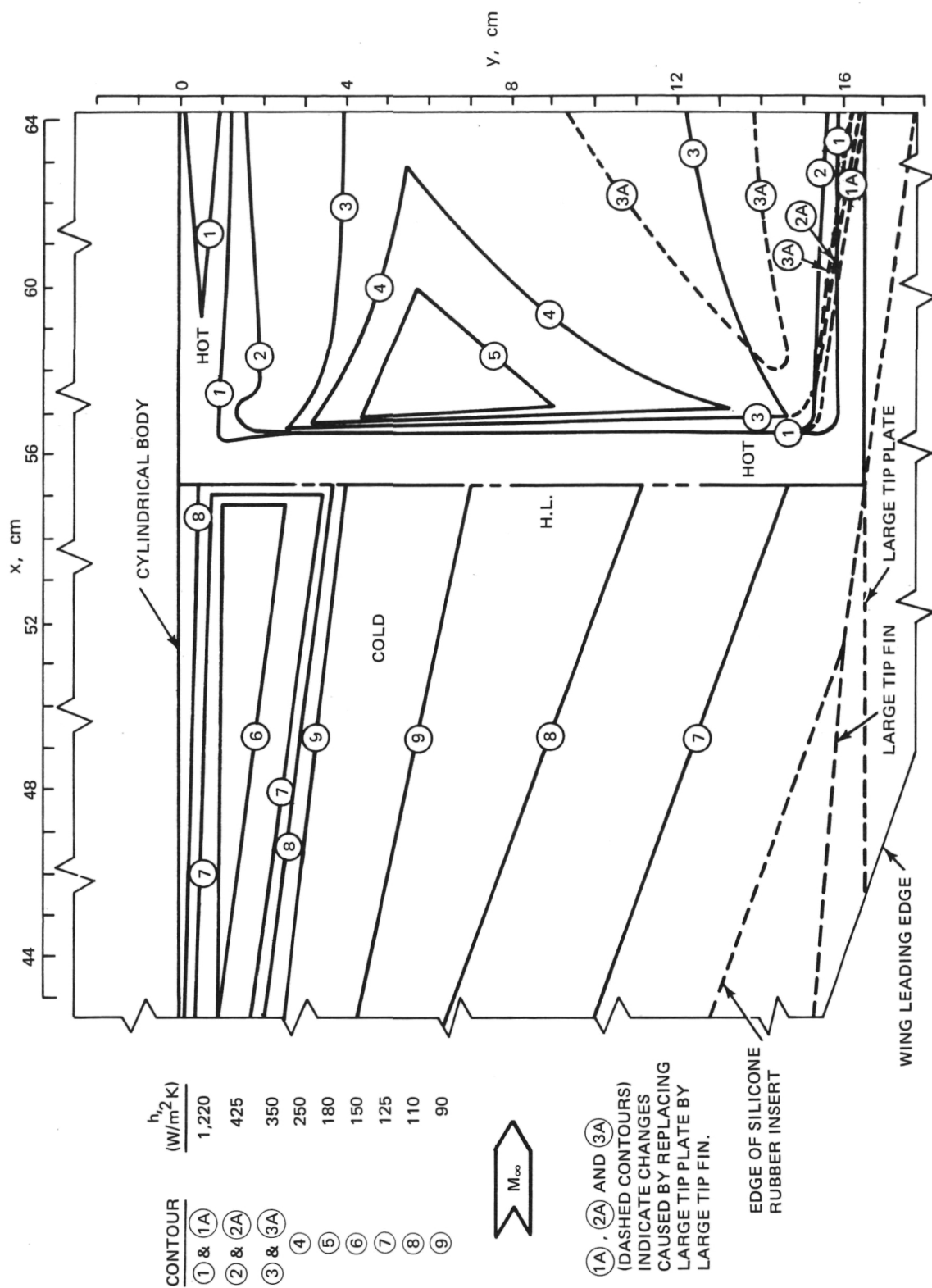
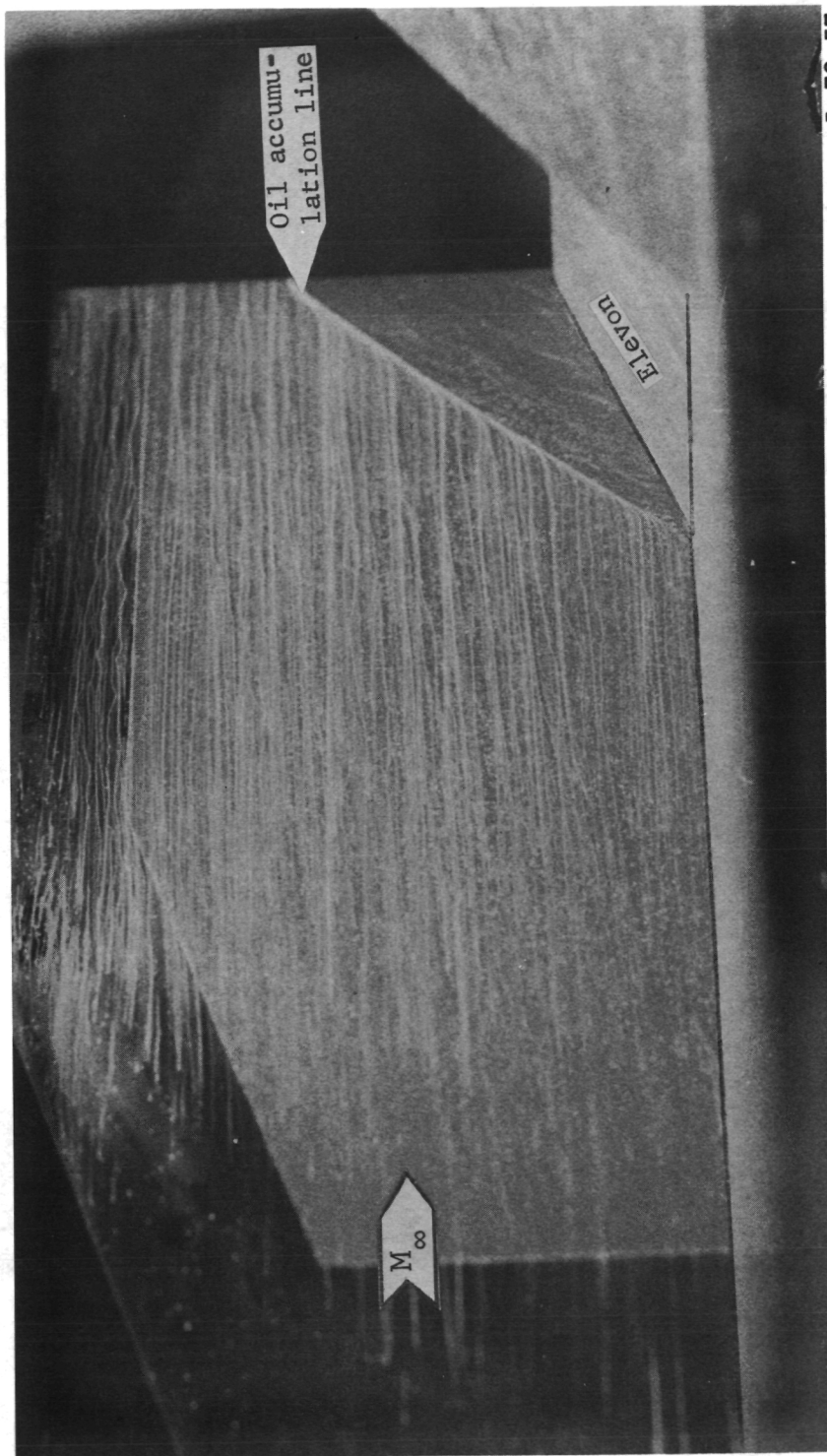
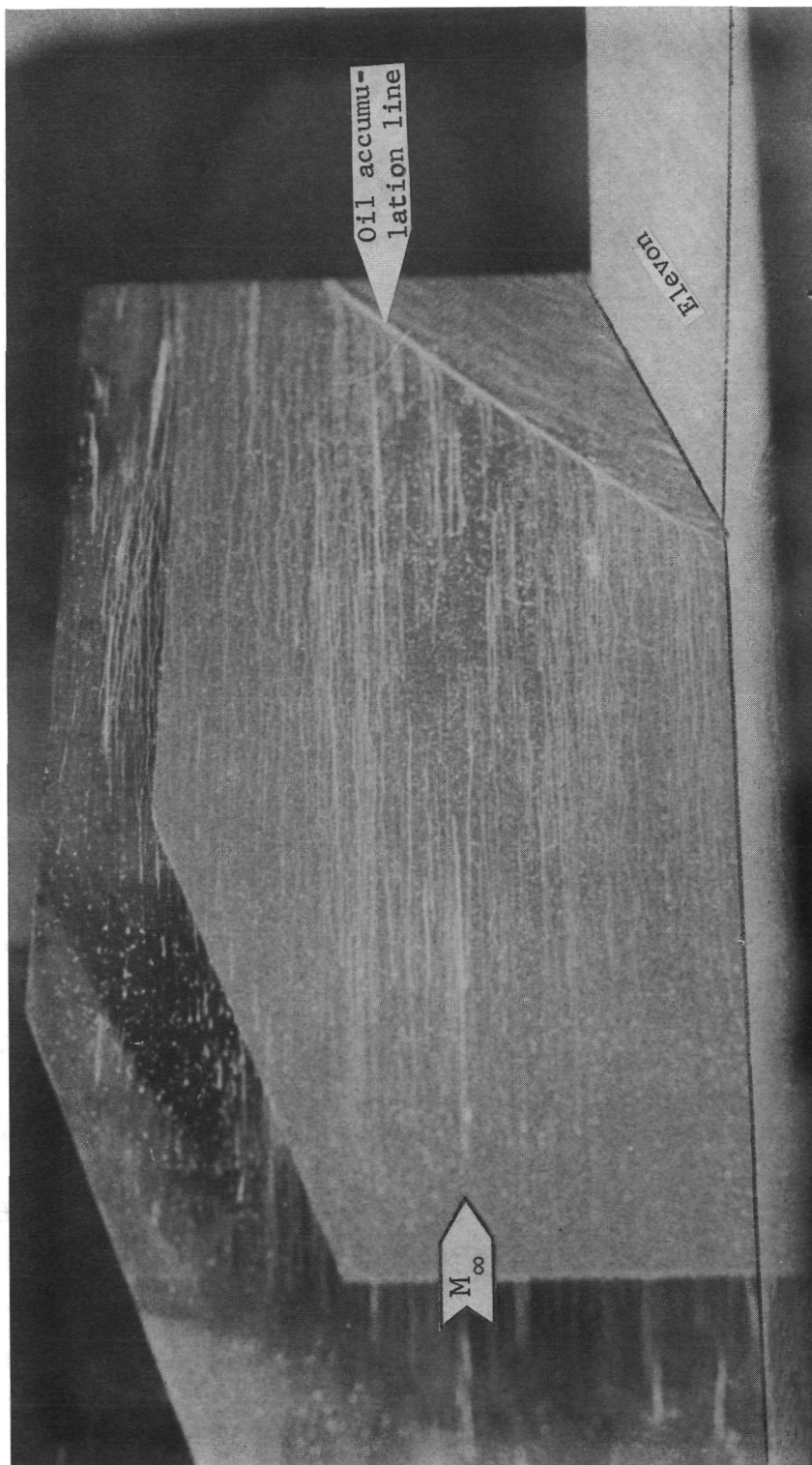


Figure 40.- Constant heat transfer coefficient contours on wing and elevon surfaces. $\epsilon = 20^\circ$; $\Lambda = 70^\circ$; cylindrical body and either large tip plate or large tip fin attached.



L-78-57

Figure 41.- Frame from profile oil film flow motion picture showing end plate surface.
 $\epsilon = 20^\circ$; $\Lambda = 0^\circ$; large tip plate attached.



L-78-58

Figure 42.- Frame from profile oil film flow motion picture showing end plate surface.
 $\epsilon = 20^\circ$ and $\Lambda = 50^\circ$.

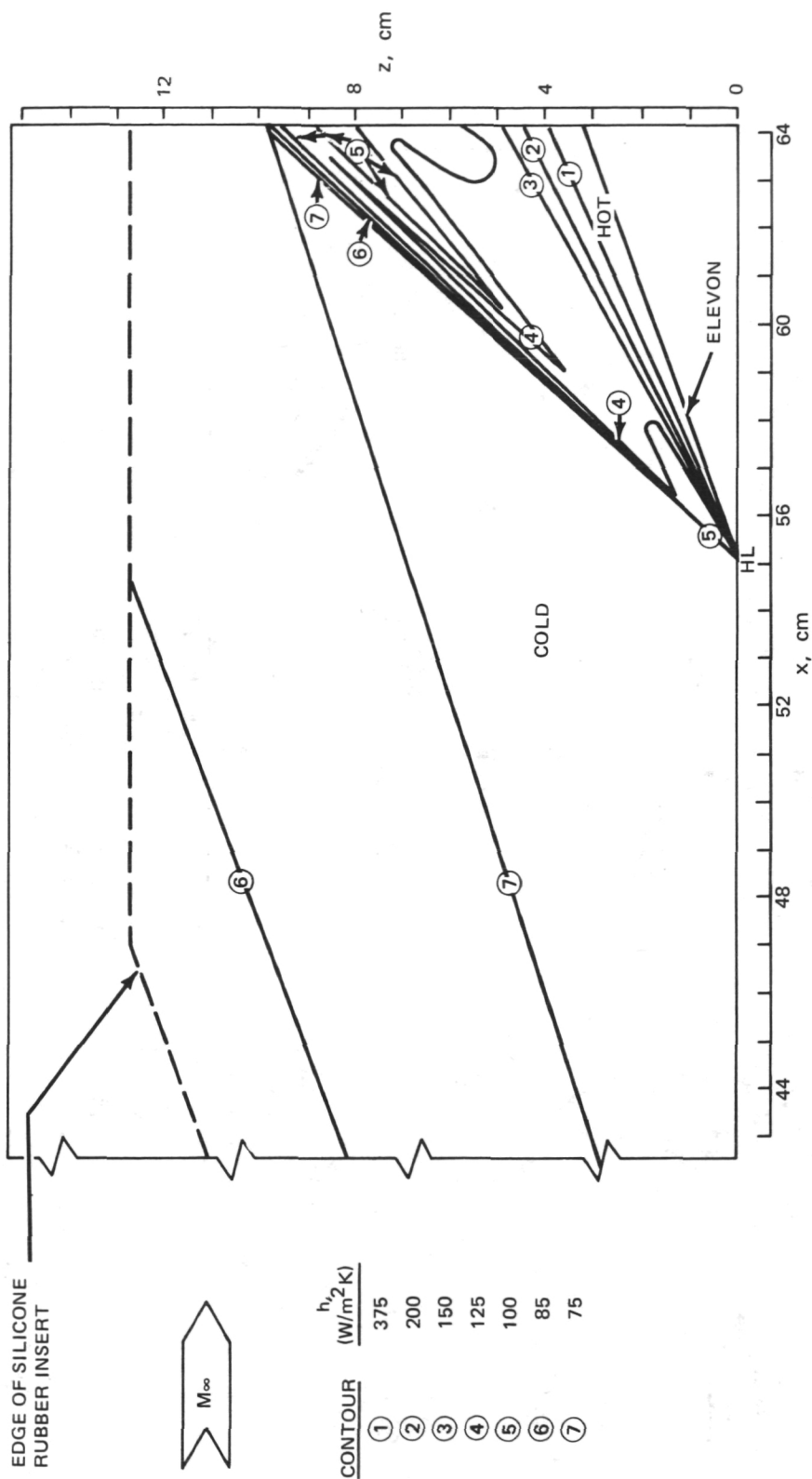


Figure 43.- Constant heat transfer coefficient contours on end plate surface. $\epsilon = 20^\circ$. Contours shown for five configurations: $\Lambda = 0^\circ$ with and without large tip plate, $\Lambda = 50^\circ$ without large tip plate, and $\Lambda = 70^\circ$ with and without large tip plate.

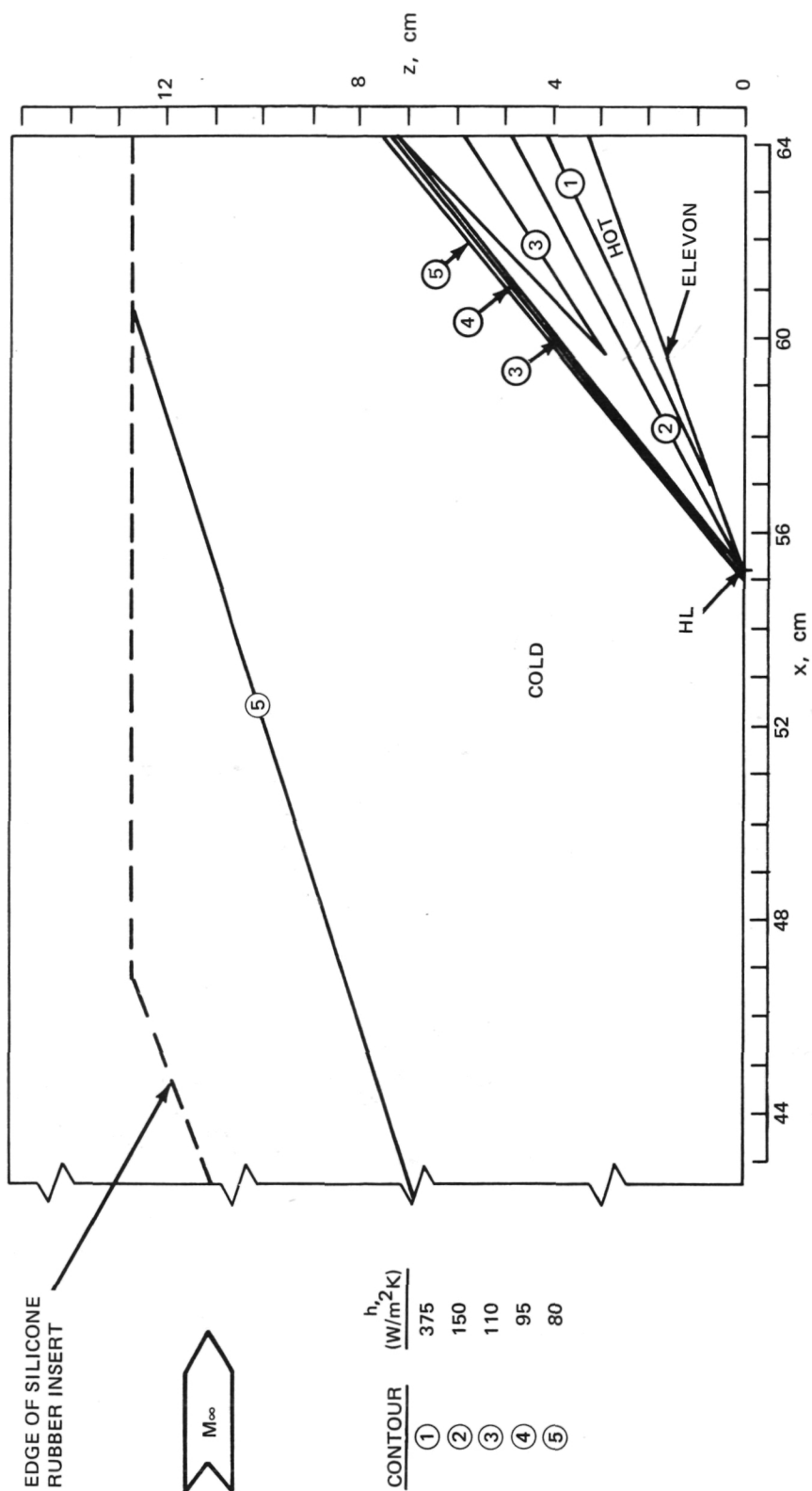


Figure 44.- Constant heat transfer coefficient contours on end plate surface. $\epsilon = 20^\circ$; 0.64-cm gap between end plate and elevon. Contours shown for three configurations: $\Lambda = 0^\circ$ without large tip plate and $\Lambda = 70^\circ$ with and without large tip plate.

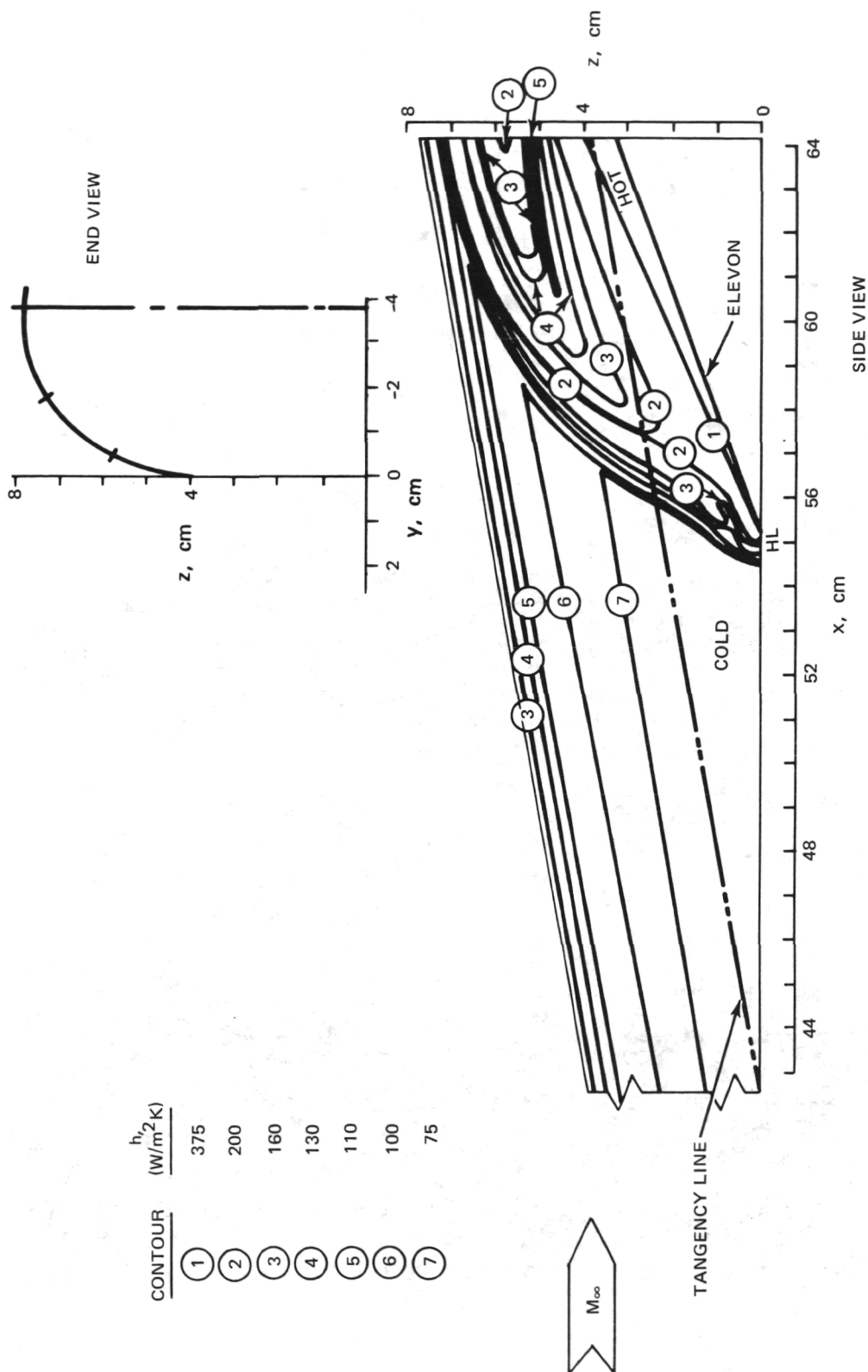


Figure 45.- Constant heat transfer coefficient contours on cylindrical body surface. $\varepsilon = 20^\circ$ and $\Lambda = 70^\circ$. Contours shown for three configurations: with no tip attachment, with large tip plate, and with large tip fin.

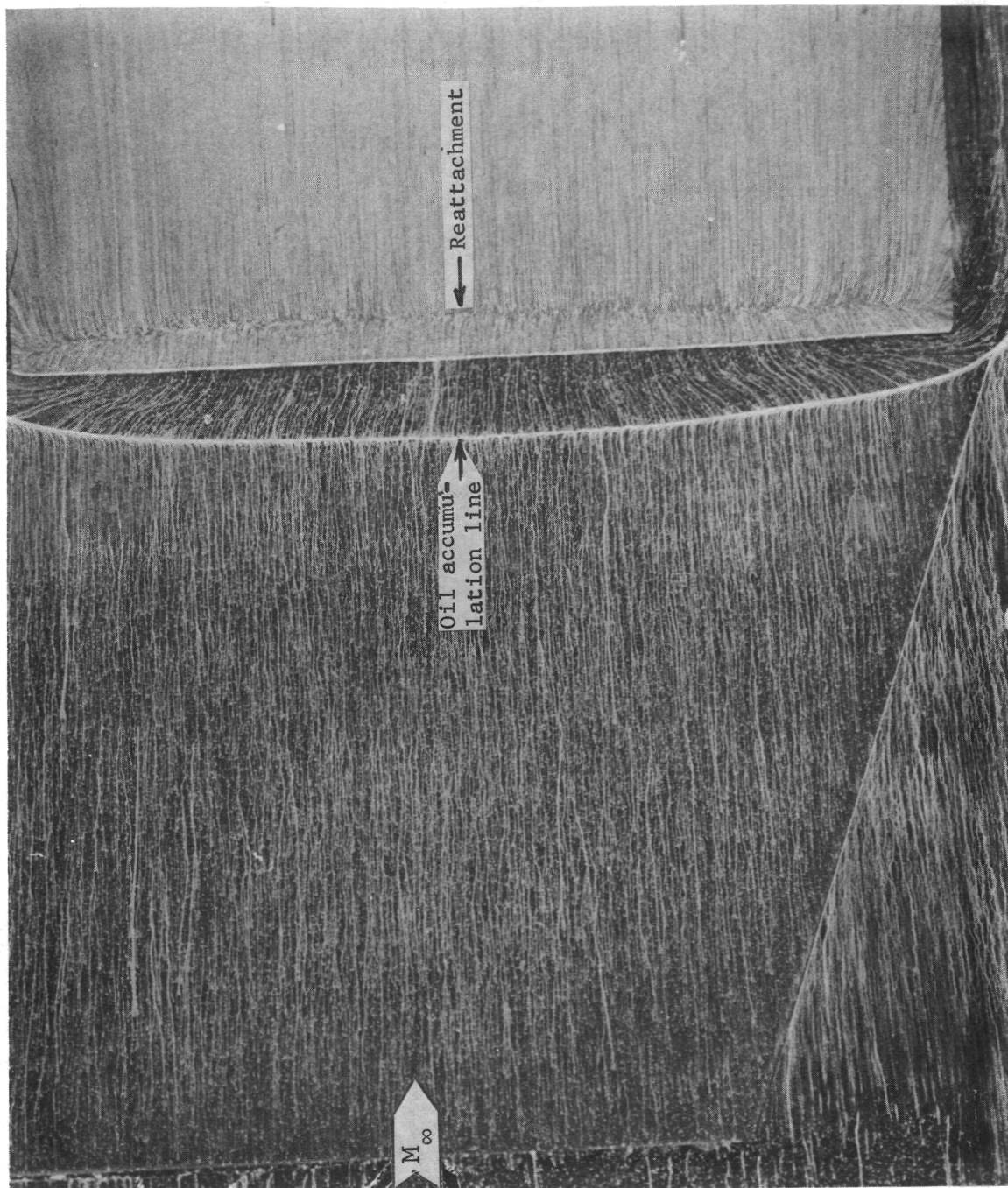


Figure 46.- Frame from planform oil film flow motion picture showing wing and elevon surfaces.
 $\epsilon = 30^\circ$ and $\Lambda = 0^\circ$.
 L-78-59

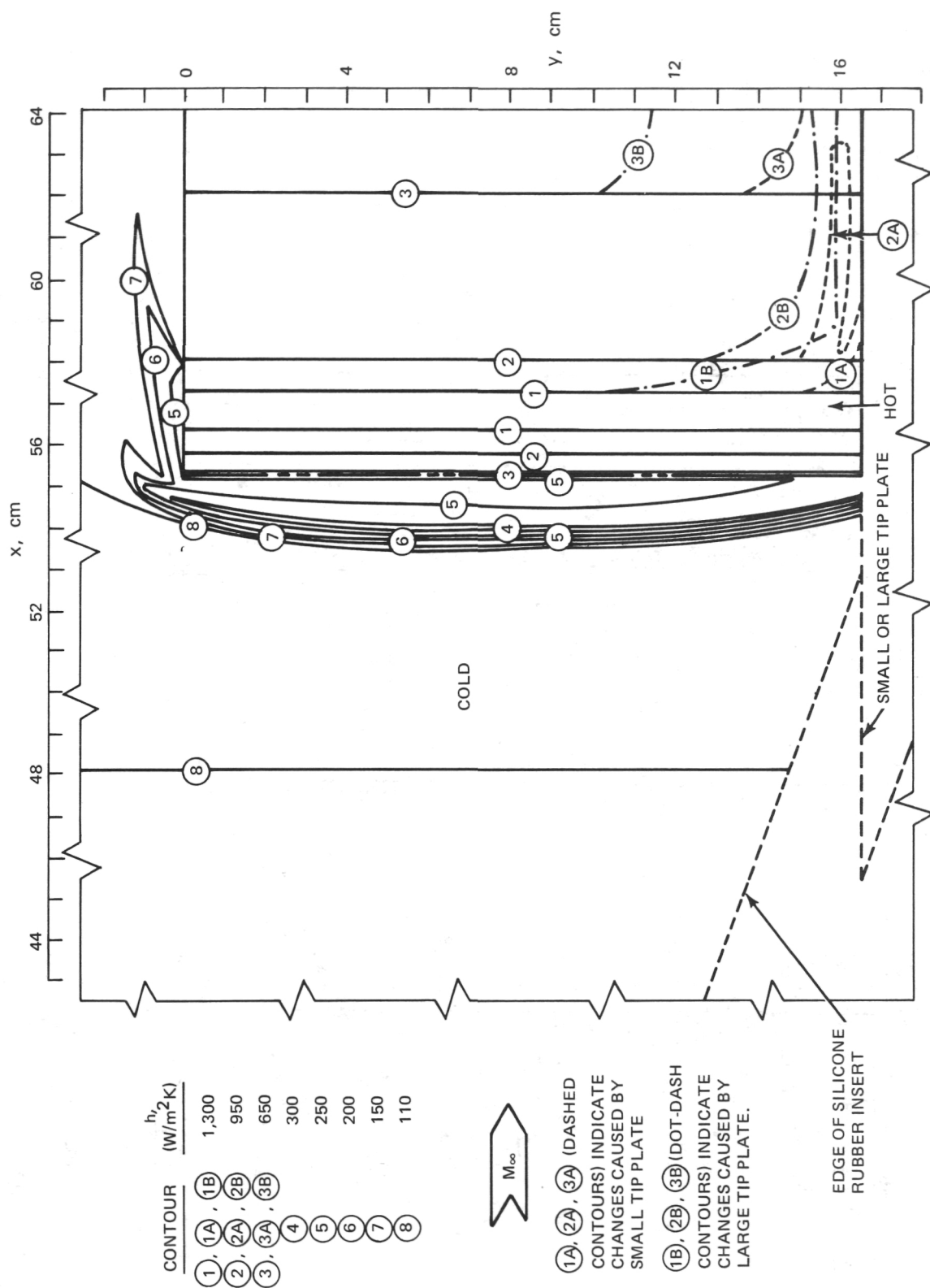


Figure 47.- Constant heat transfer coefficient contours on wing and elevon surfaces. $\epsilon = 30^\circ$ and $\Lambda = 0^\circ$. Contours shown for three configurations: with no attachments, with small tip plate, and with large tip plate.

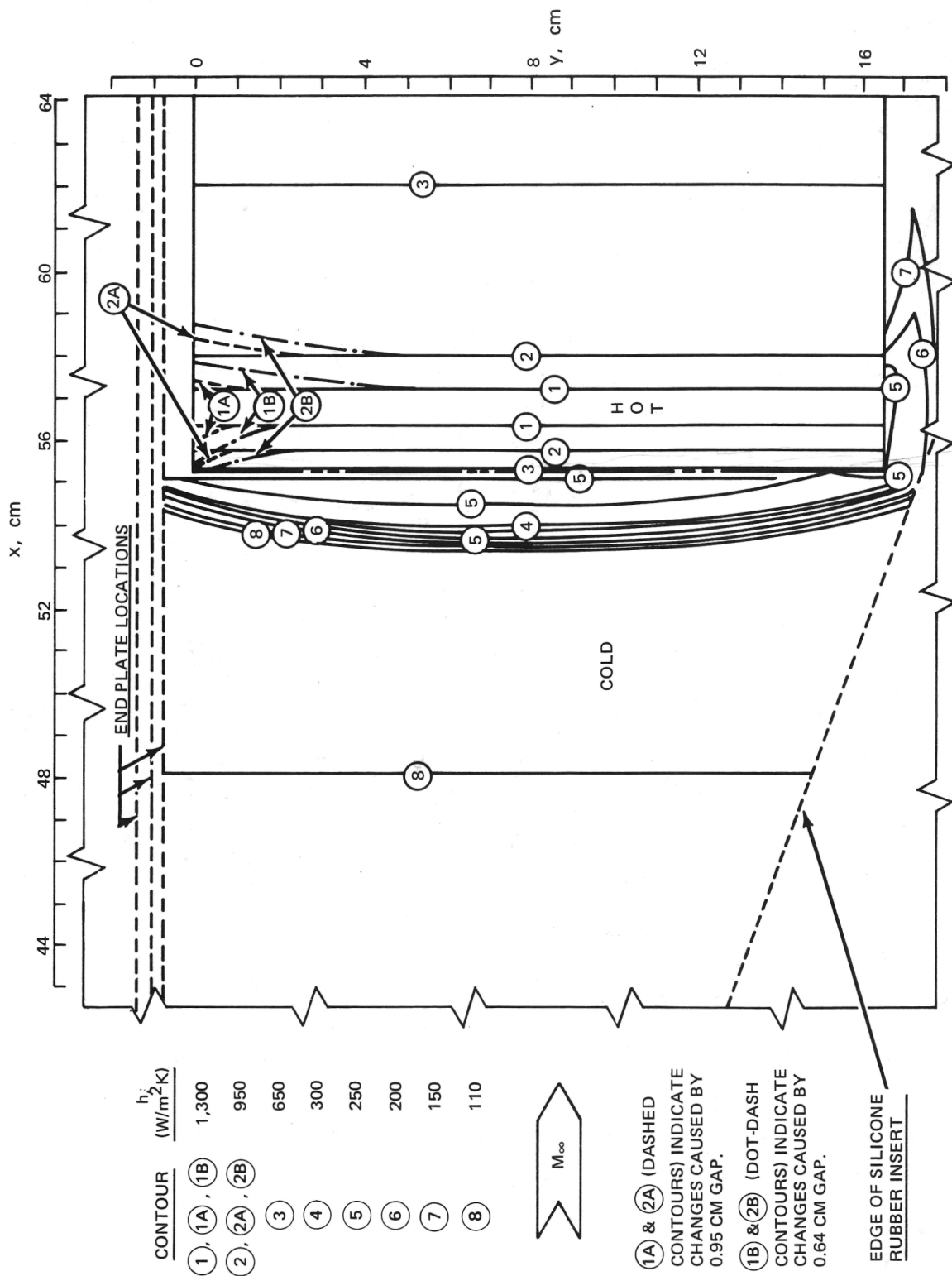


Figure 48.- Constant heat transfer coefficient contours on wing and elevon surfaces. $\epsilon = 30^\circ$; $\Lambda = 0^\circ$; end plate attached with $g = 0.64, 0.95$, or 1.27 cm.

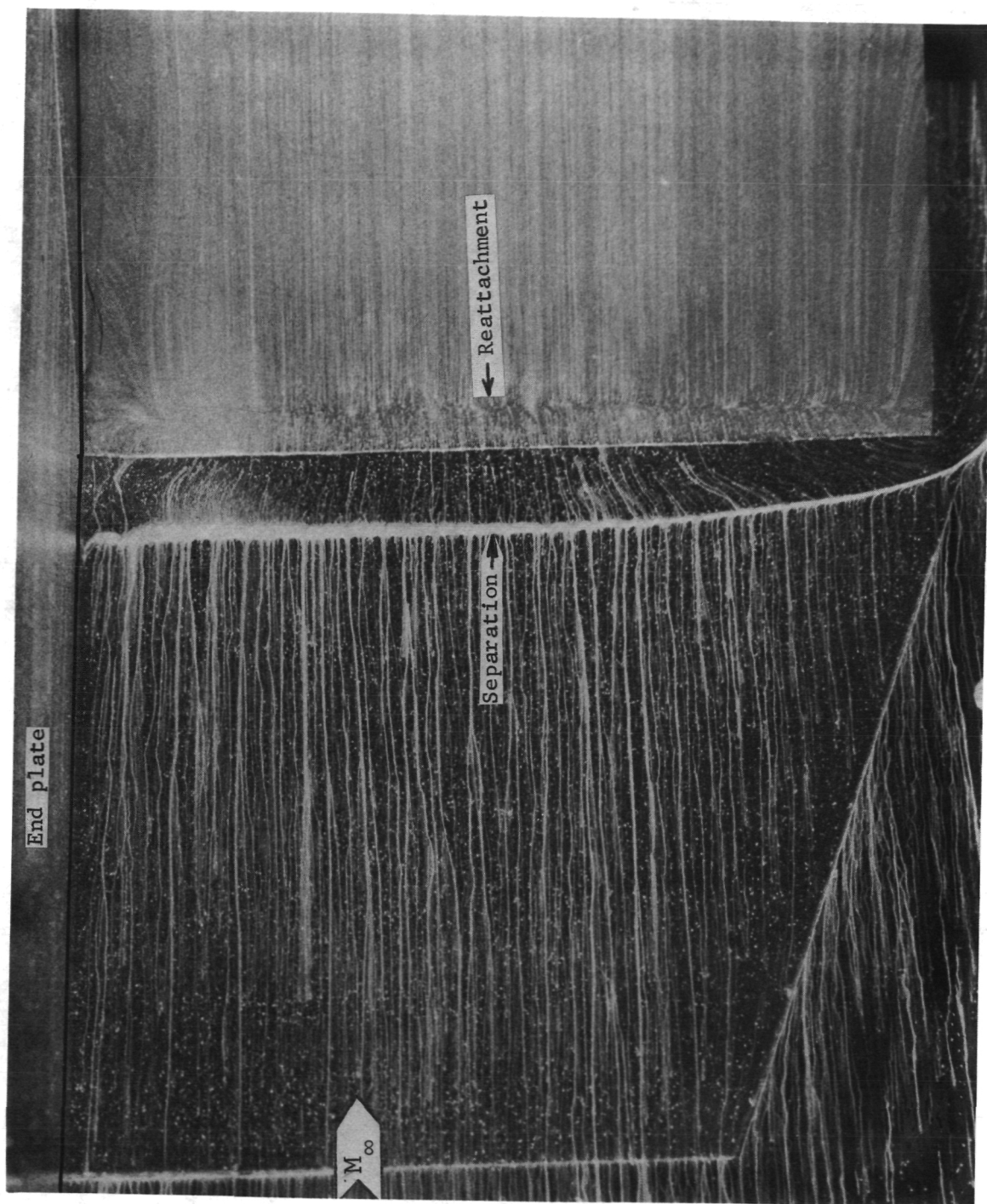


Figure 49.- Frame from planform oil film flow motion picture showing wing and elevon surfaces.
 $\epsilon = 30^\circ$; $\Lambda = 0^\circ$; end plate attached.

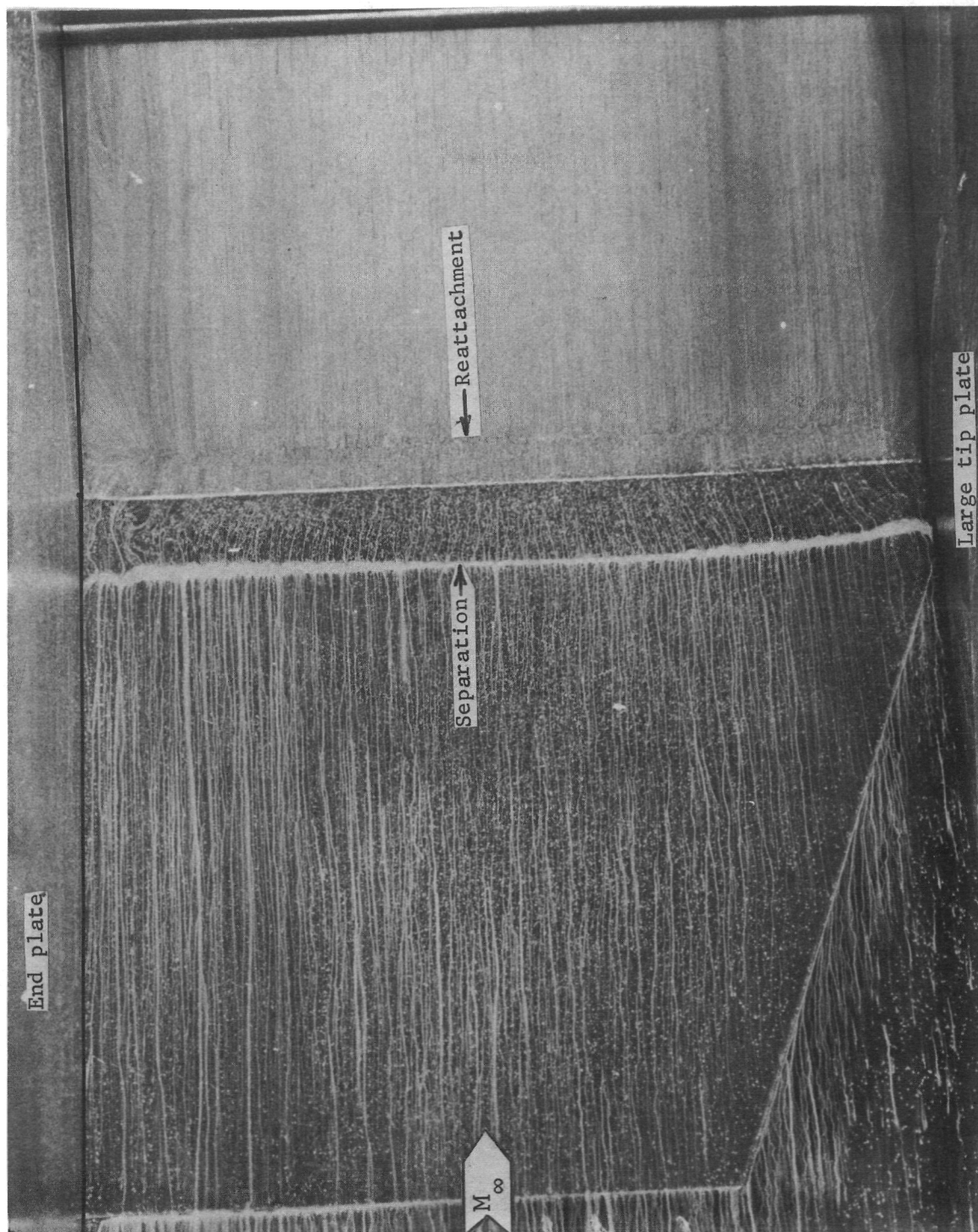


Figure 50.- Frame from planform oil film flow motion picture showing wing and elevon surfaces.
 $\epsilon = 30^\circ$; $\Lambda = 0^\circ$; end plate and large tip plate attached.

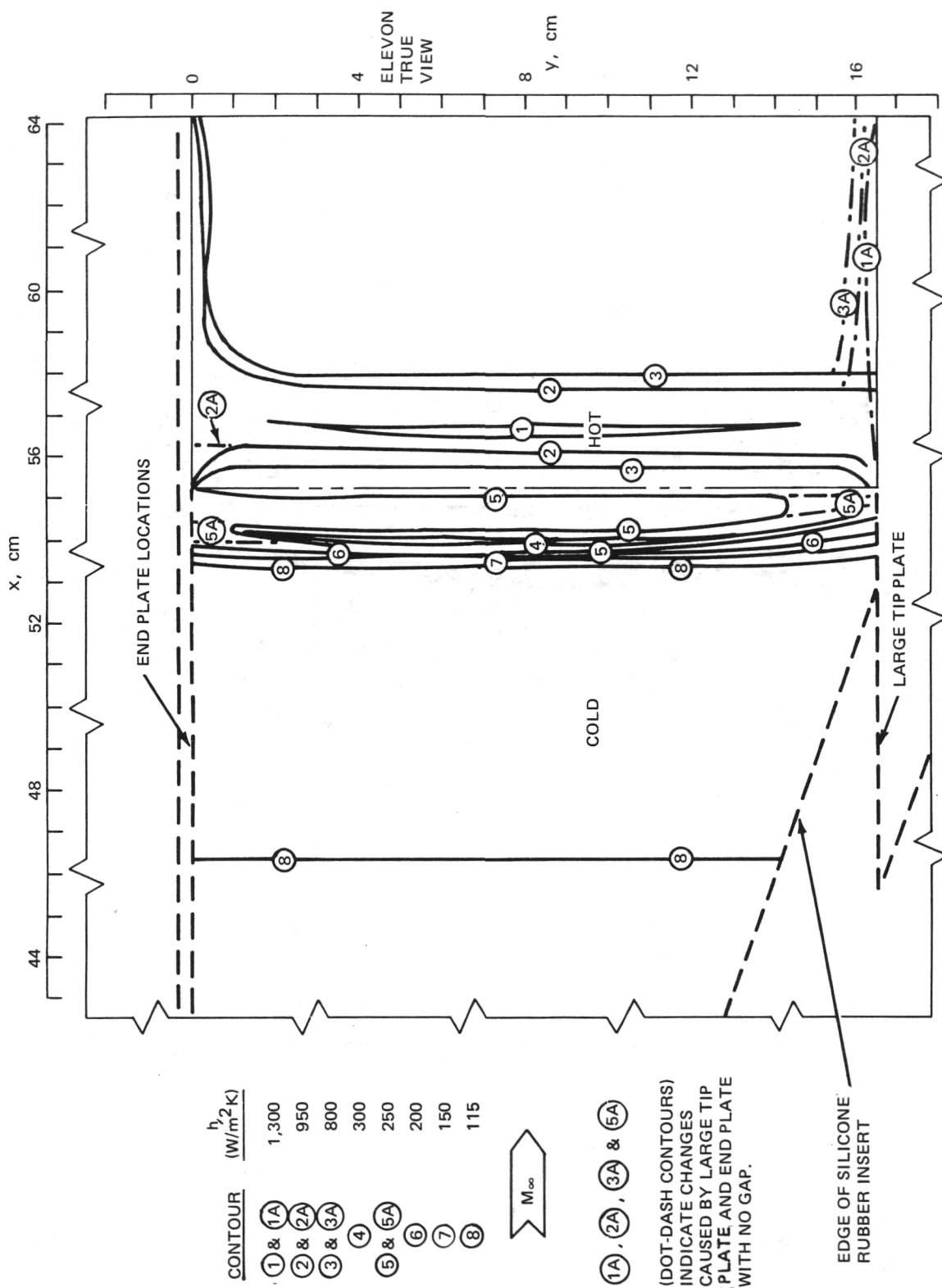


Figure 51.- Constant heat transfer coefficient contours on wing and elevon surfaces. $\epsilon = 30^\circ$; $\Lambda = 0^\circ$; and end plate attached. Contours shown for three configurations: end plate attached ($g = 0.32$ cm), end plate attached ($g = 0$ cm), and large tip plate attached.

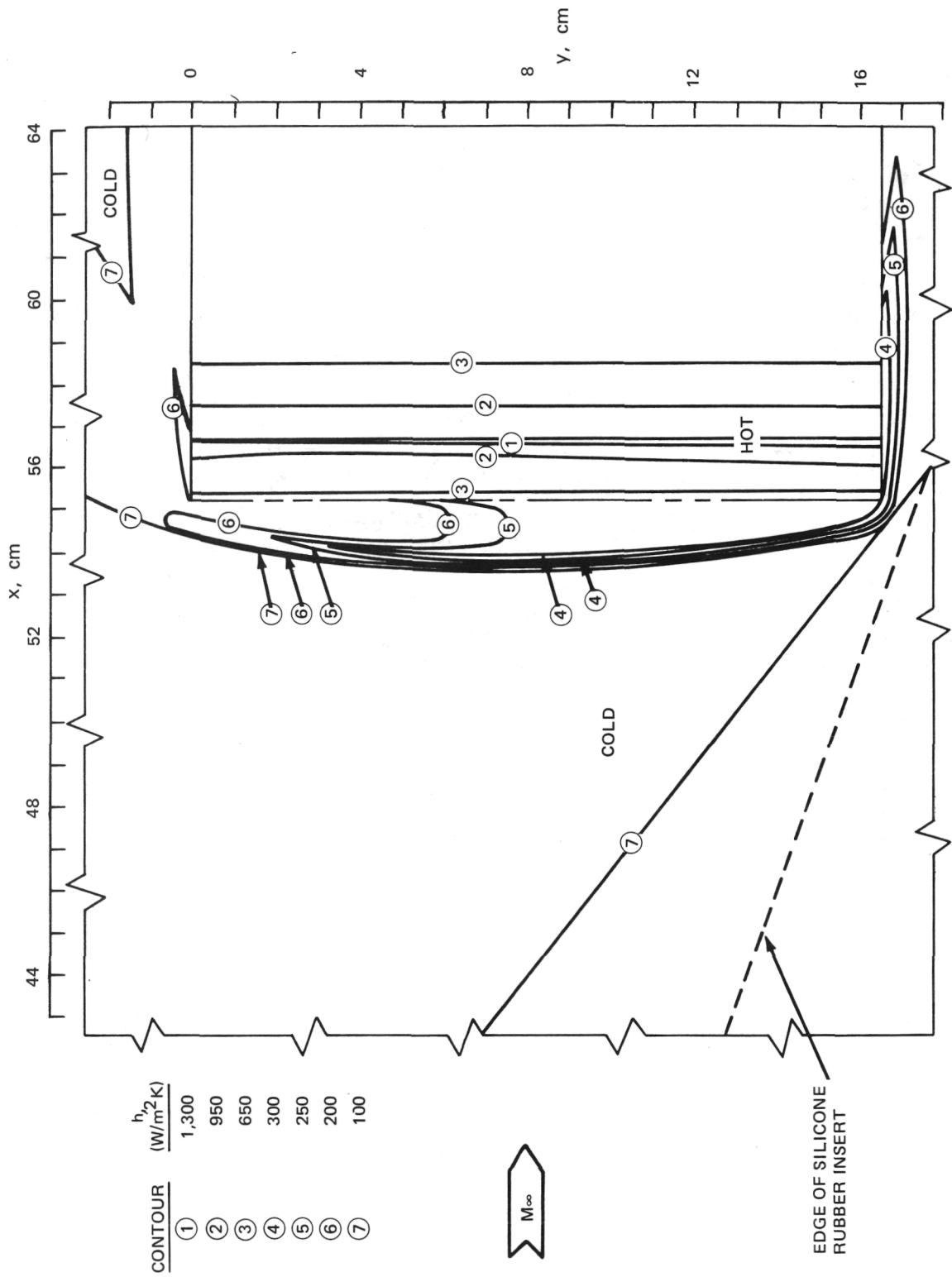


Figure 52.- Constant heat transfer coefficient contours on wing and elevon surfaces.
 $\epsilon = 30^\circ$ and $\Lambda = 50^\circ$.



Figure 53.- Frame from planform oil film flow motion picture showing wing and elevon surfaces.
 $\epsilon = 30^\circ$; $\Lambda = 50^\circ$; end plate attached.
 L-78-62

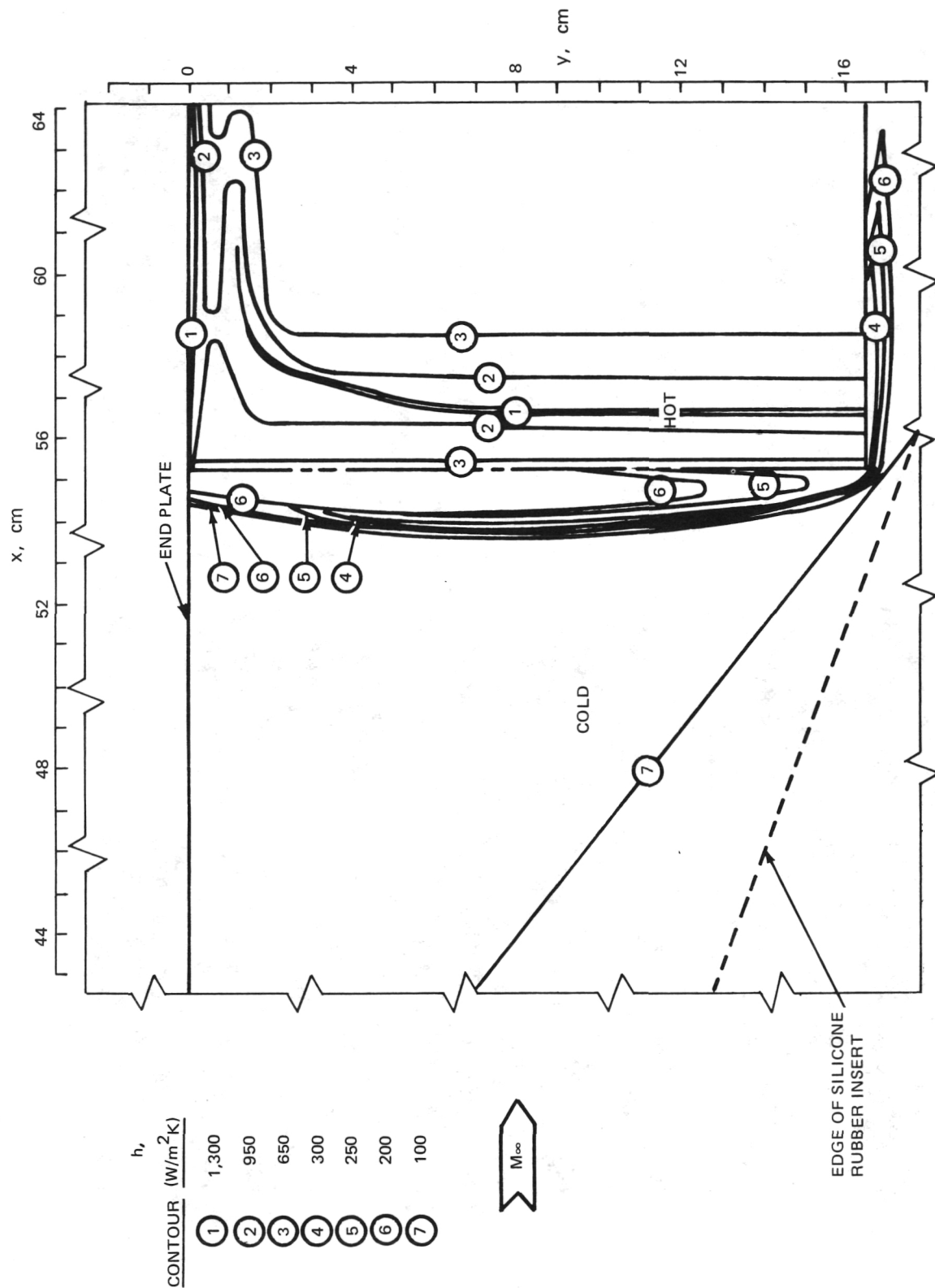


Figure 54.- Constant heat transfer coefficient contours on wing and elevon surfaces.
 $\epsilon = 30^\circ$; $\Lambda = 50^\circ$; end plate attached.

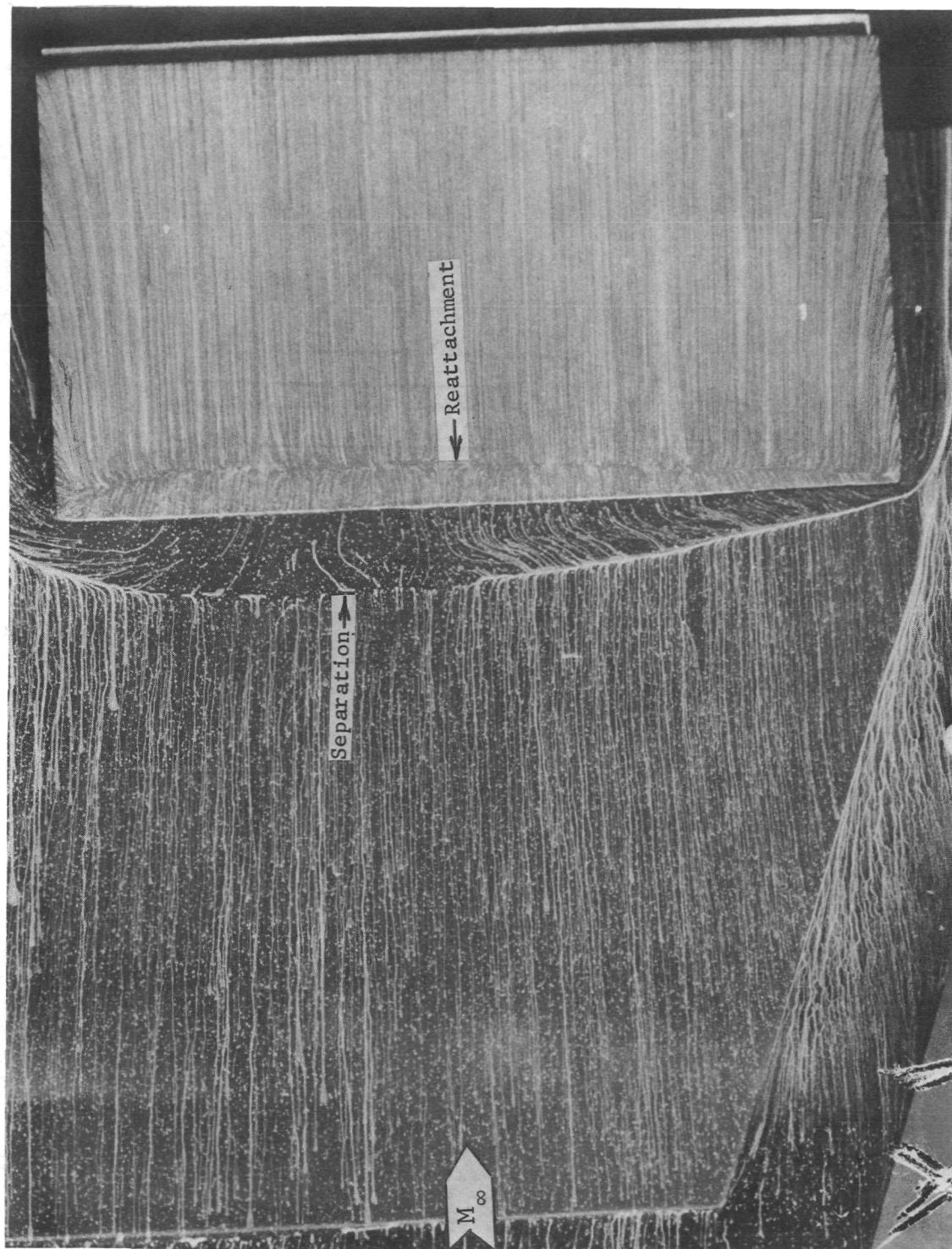


Figure 55.- Frame from planform oil film flow motion picture showing wing and elevon surfaces.
 $\epsilon = 30^\circ$ and $\Lambda = 70^\circ$.
 L-78-63

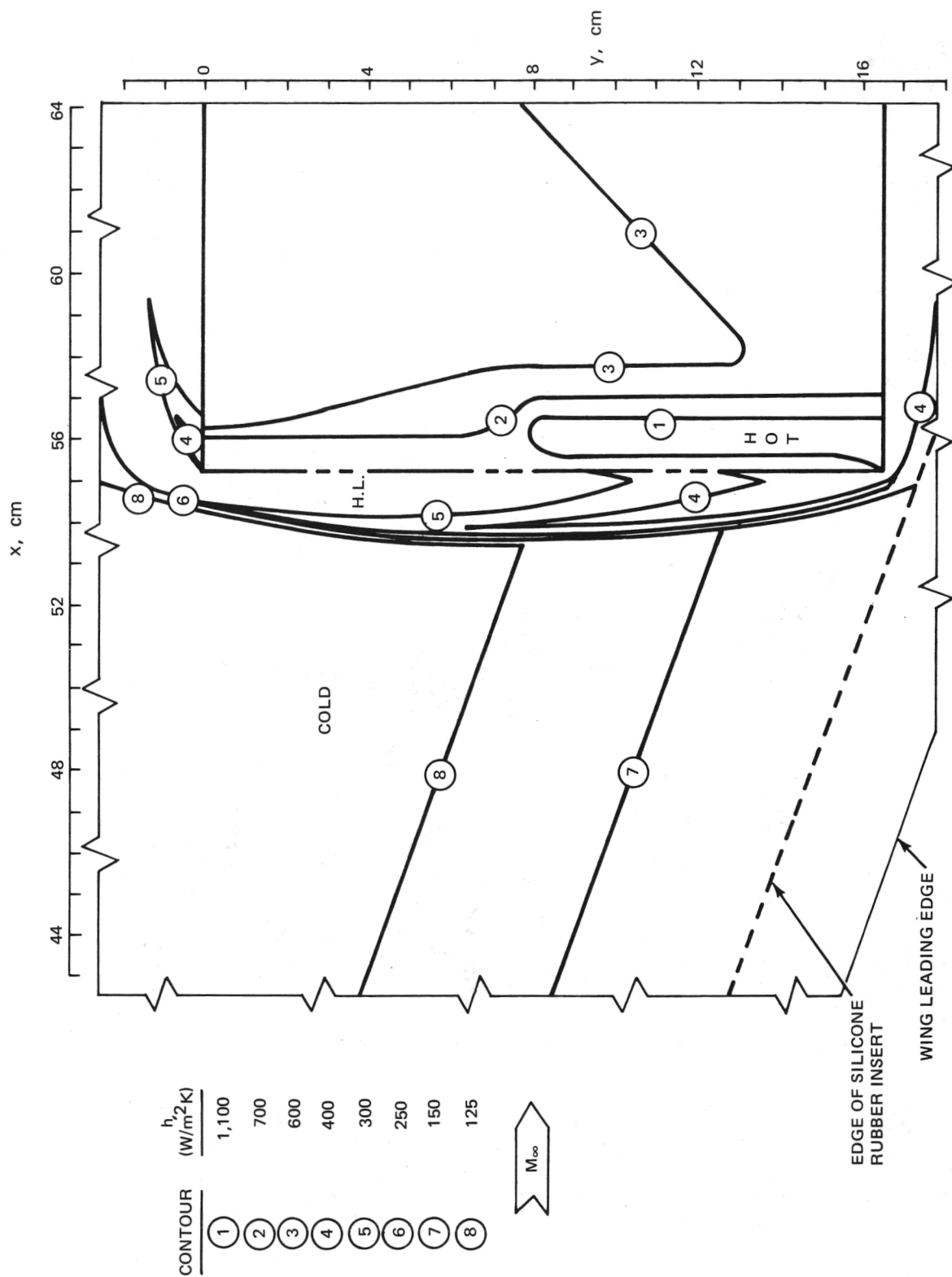


Figure 56.- Constant heat transfer coefficient contours on wing and elevator surfaces.
 $\epsilon = 30^\circ$ and $\Lambda = 70^\circ$.

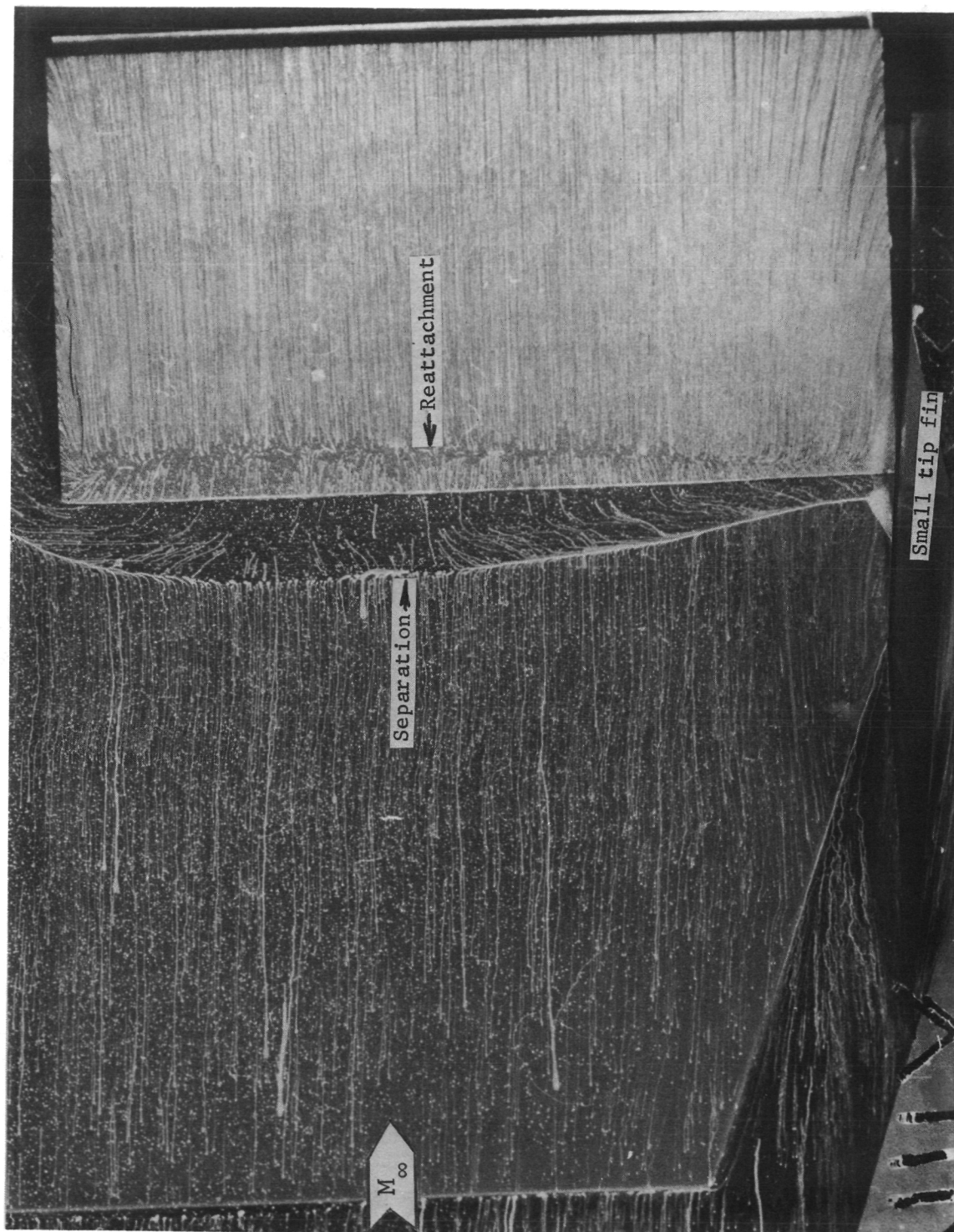


Figure 57.- Frame from planform oil film flow motion picture showing wing and elevon surfaces.
 $\epsilon = 30^\circ$; $\Lambda = 70^\circ$; small tip fin attached.

L-78-64

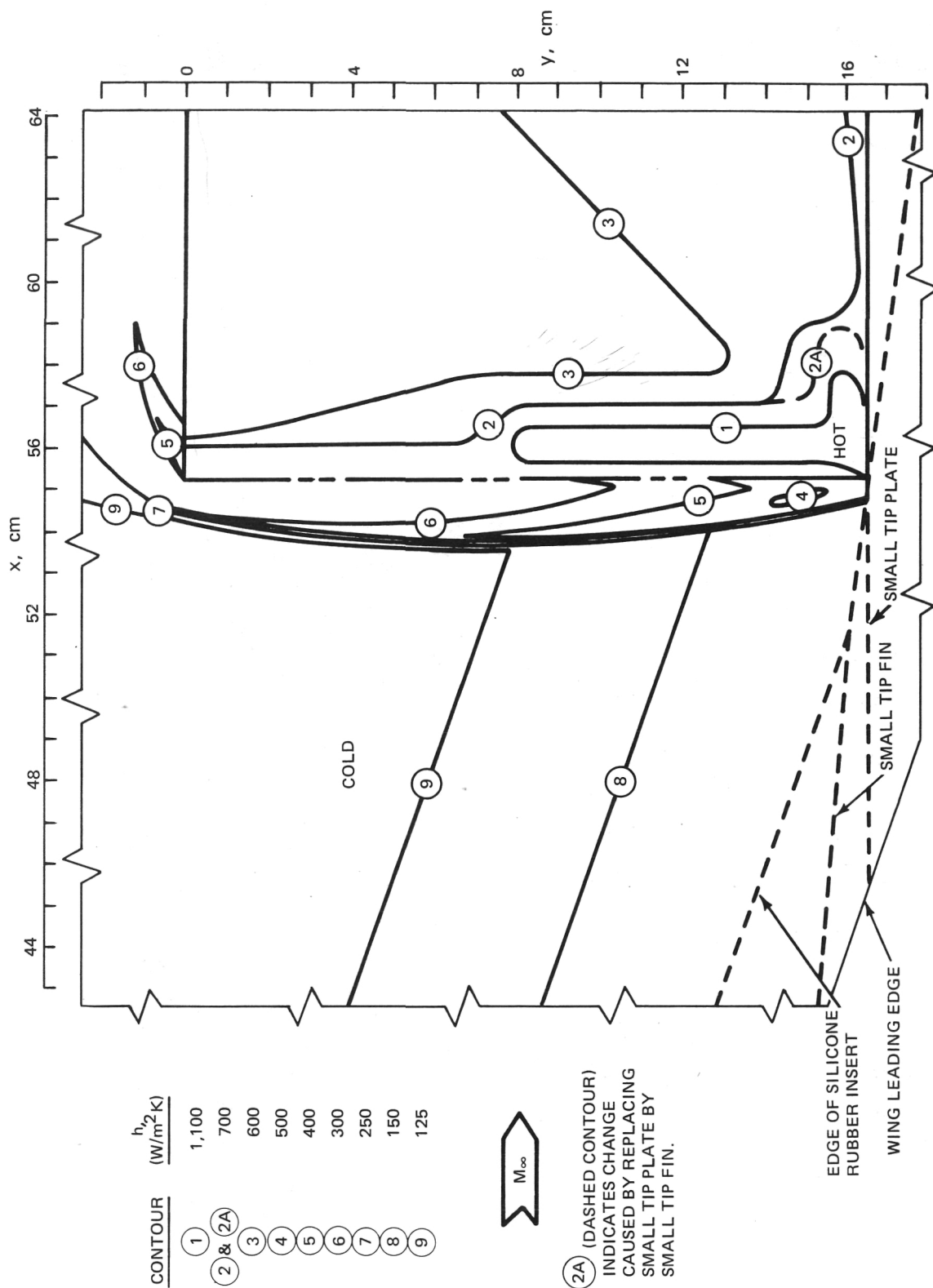


Figure 58.- Constant heat transfer coefficient contours on wing and elevon surfaces. $\epsilon = 30^\circ$; $\Lambda = 70^\circ$; and either small tip plate or small tip fin attached.

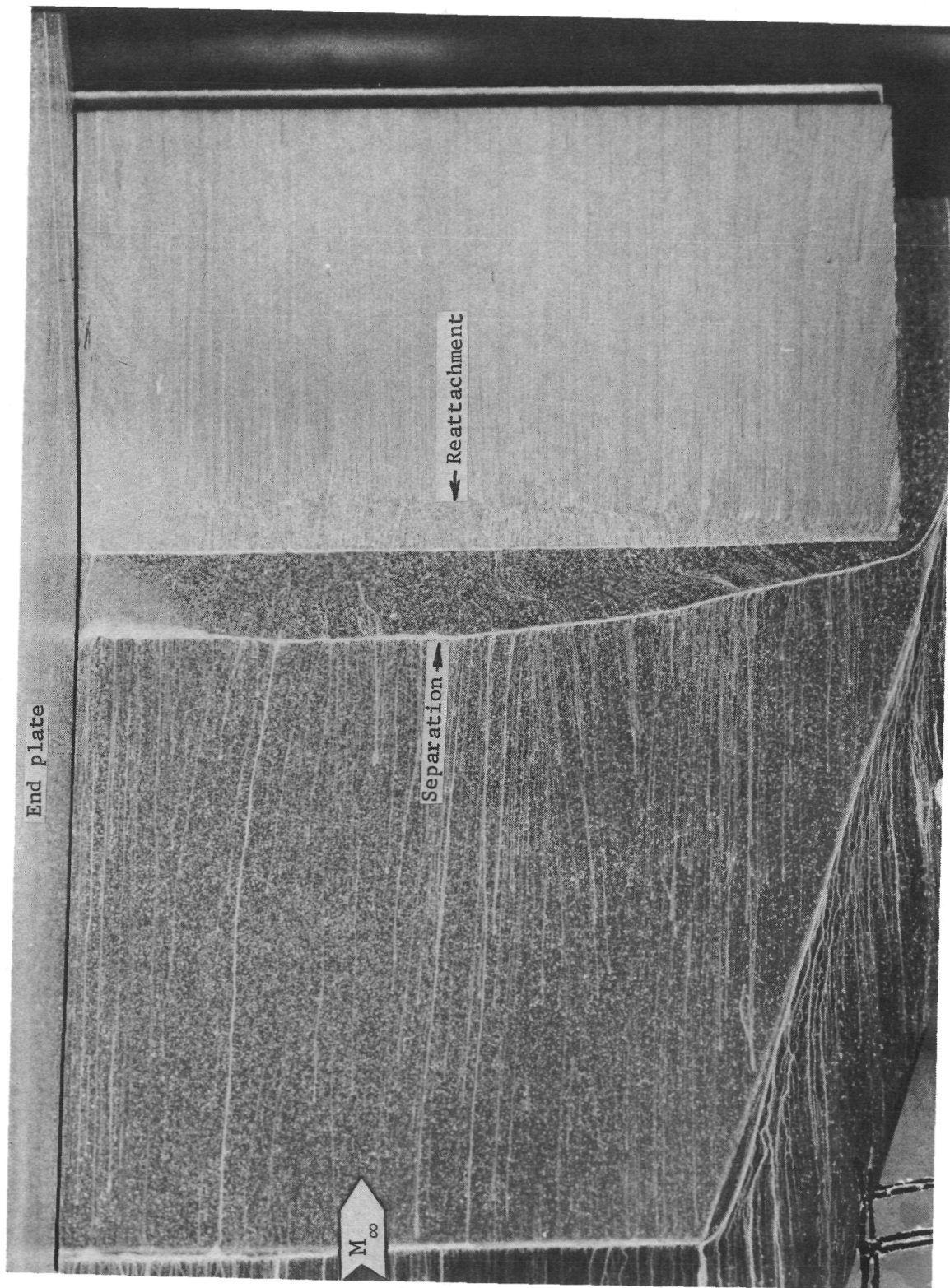


Figure 59.- Frame from planform oil film flow motion picture showing wing and elevon surfaces.
 $\epsilon = 30^\circ$; $\Lambda = 70^\circ$; end plate attached.

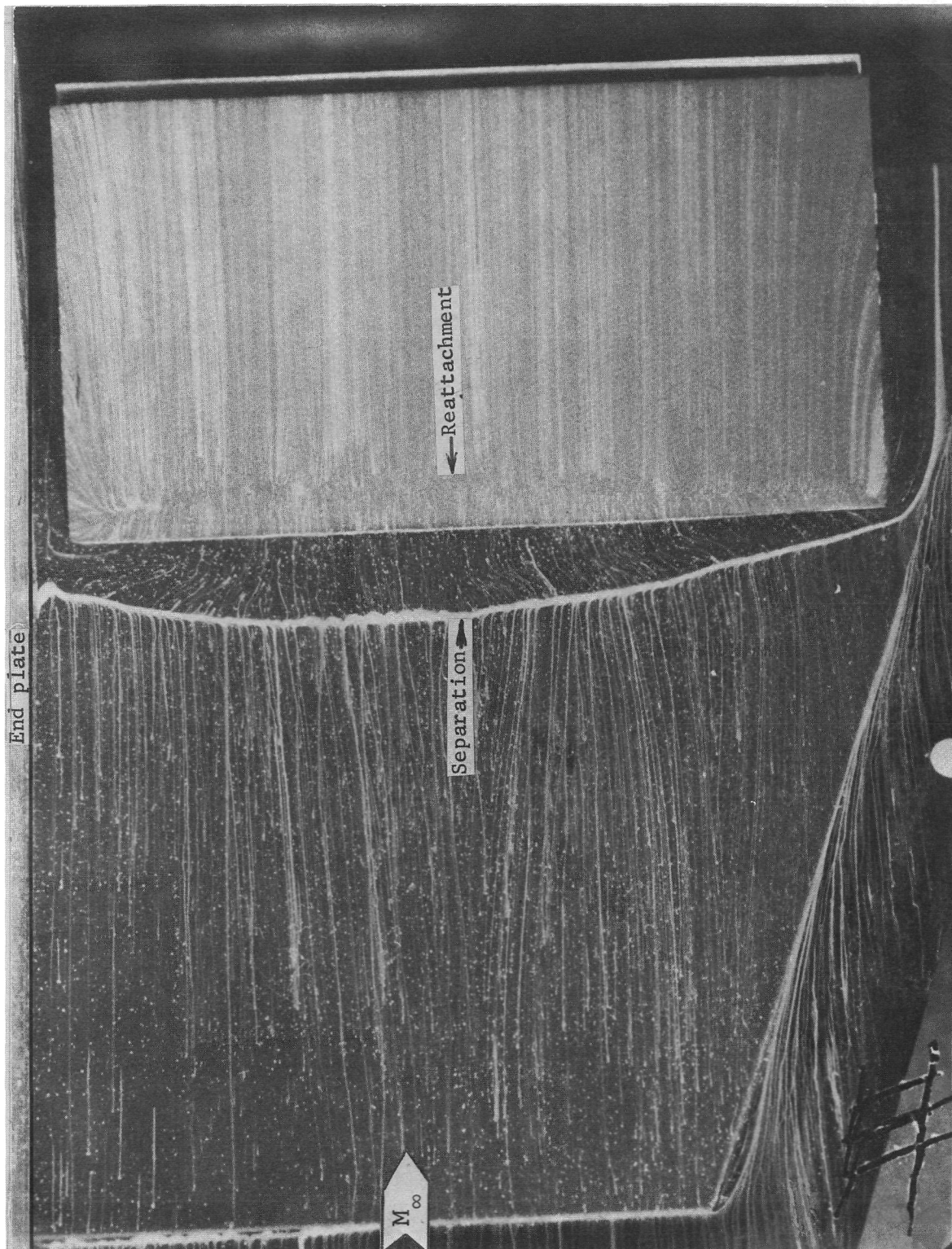


Figure 60.- Frame from planform oil film flow motion picture showing wing and elevon surfaces.
 $\epsilon = 30^\circ$; $\Lambda = 70^\circ$; end plate attached with 0.64-cm gap between end plate and elevon.

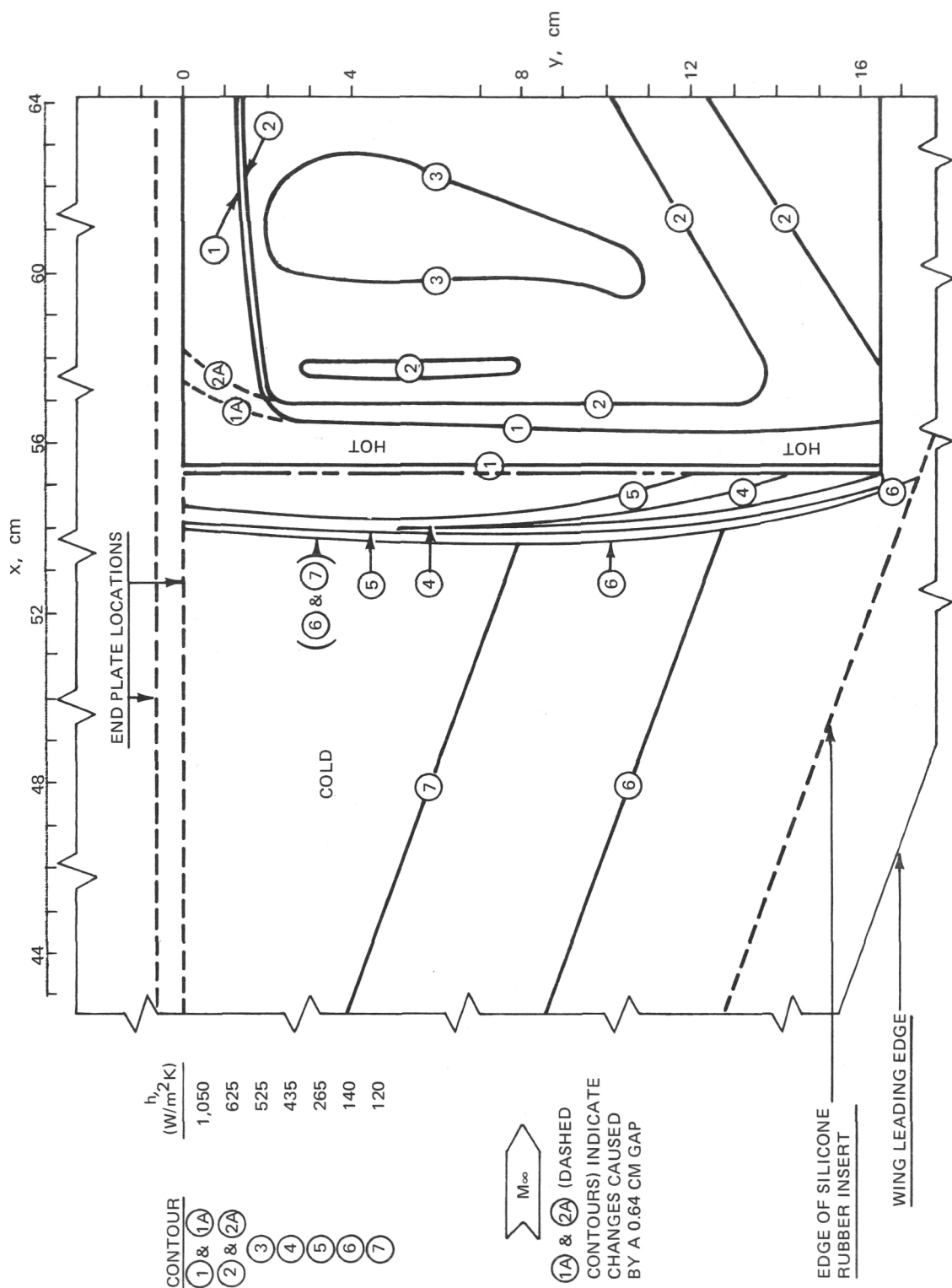


Figure 61.- Constant heat transfer coefficient contours on wing and elevon surfaces.
 $\varepsilon = 30^\circ$; $\Lambda = 70^\circ$; end plate attached with $g = 0$ or $g = 0.64$ cm.

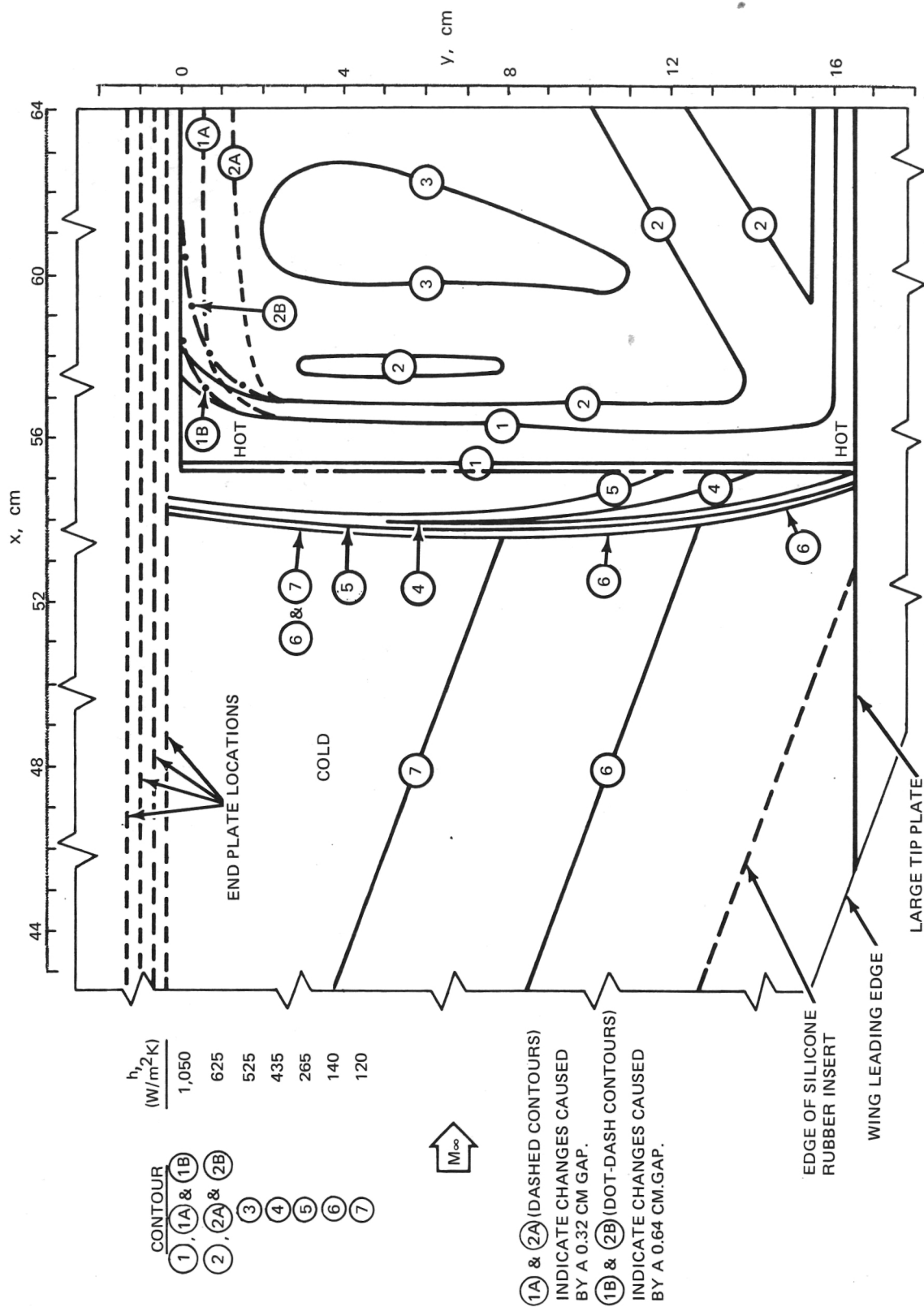


Figure 62.- Effects of end plate - elevon gap sizes on constant heat transfer coefficient contours on wing and elevon surfaces. $\epsilon = 30^\circ$; $\Lambda = 70^\circ$; large tip plate and end plate attached with $g = 1.27, 0.95, 0.64$, or 0.32 cm.



L-78-67

Figure 63.- Frame from planform oil film flow motion picture showing wing and elevon surfaces.
 $\epsilon = 30^\circ$; $\Lambda = 70^\circ$; end plate and large tip plate attached.

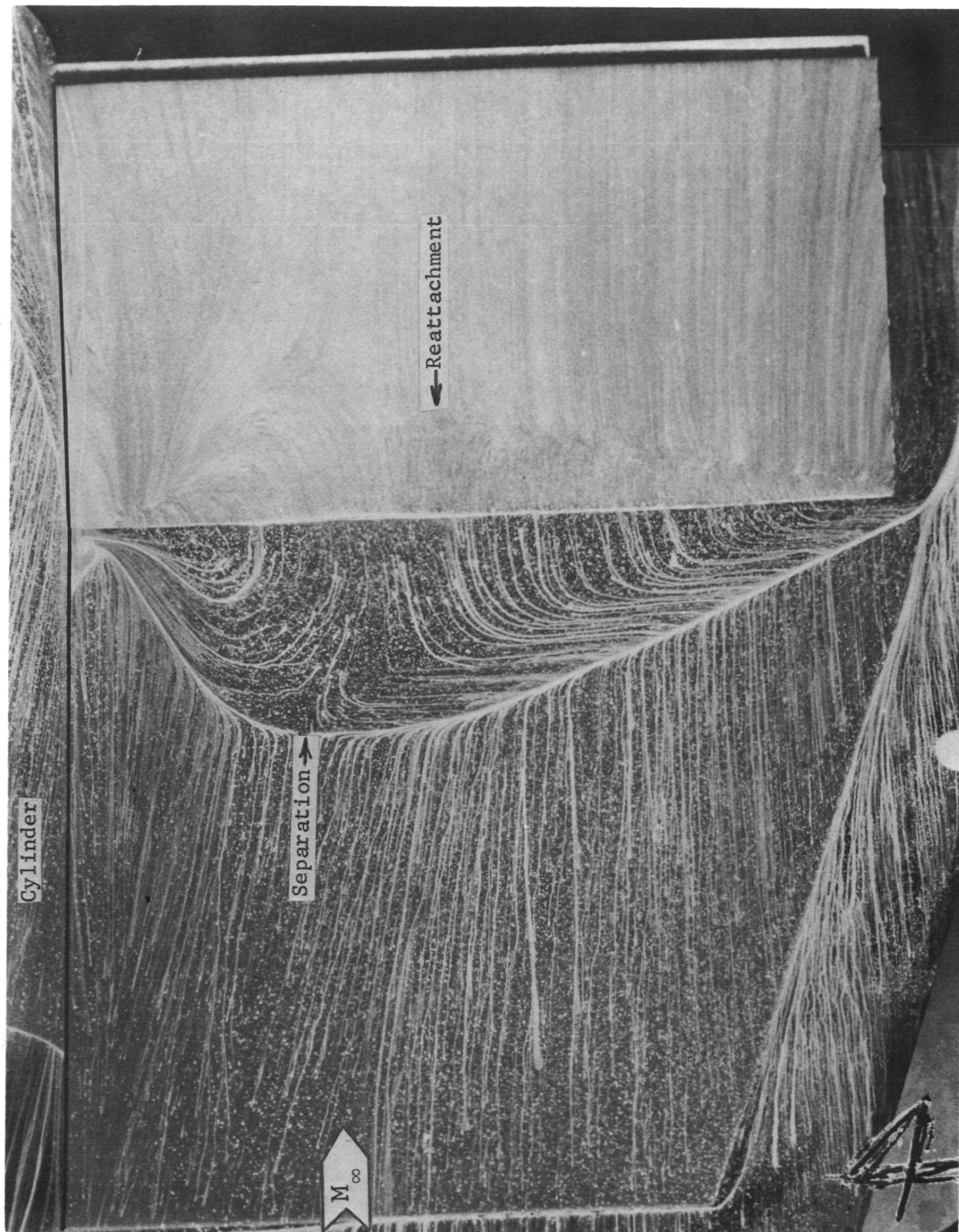


Figure 65.- Frame from planform oil film flow motion picture showing wing and elevon surfaces.
 $\epsilon = 30^\circ$; $\Lambda = 70^\circ$; cylindrical body attached.

L-78-68

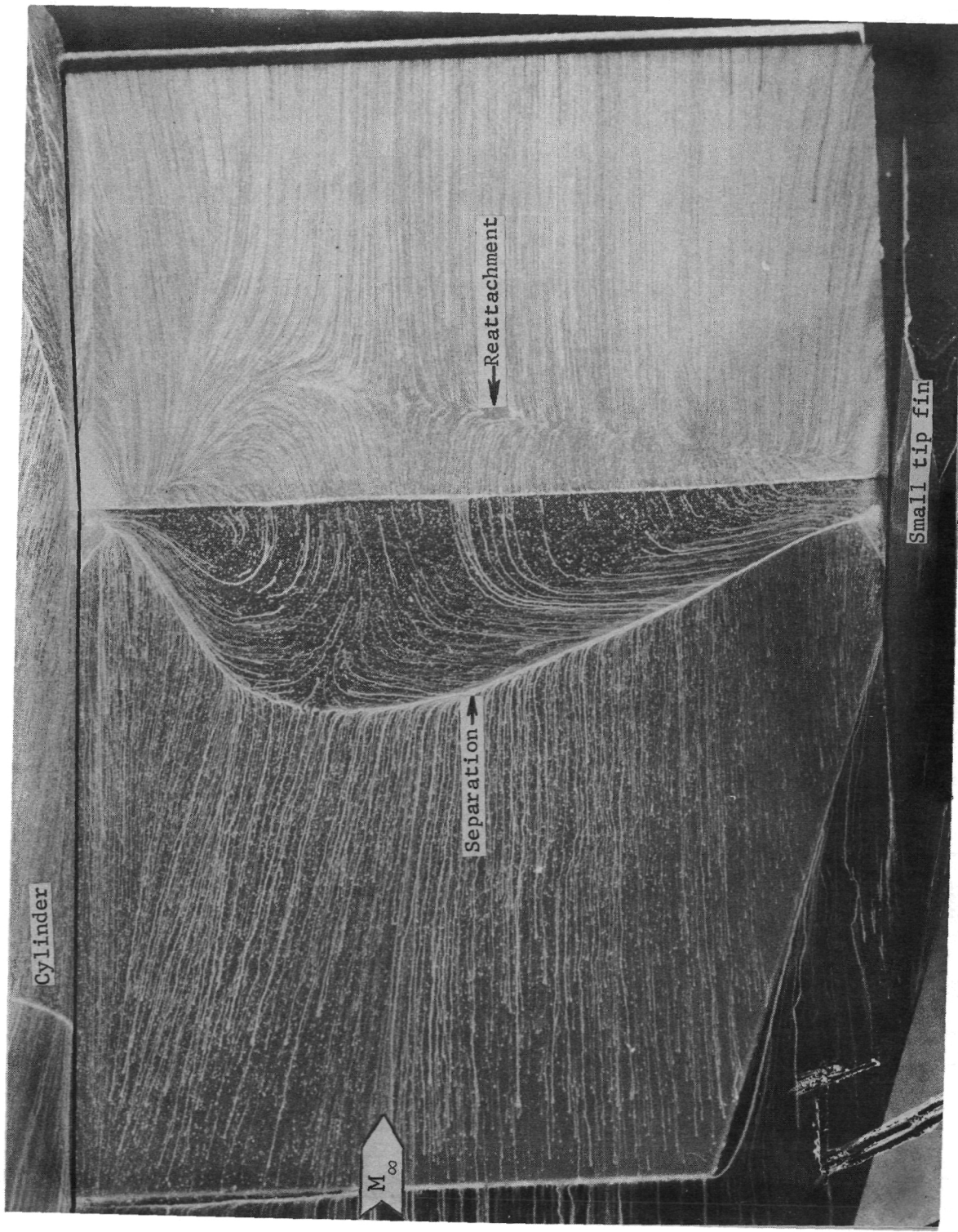


Figure 66.- Frame from planform oil film flow motion picture showing wing and elevon surfaces.
 $\epsilon = 30^\circ$; $\Lambda = 70^\circ$; cylindrical body and small tip fin attached.

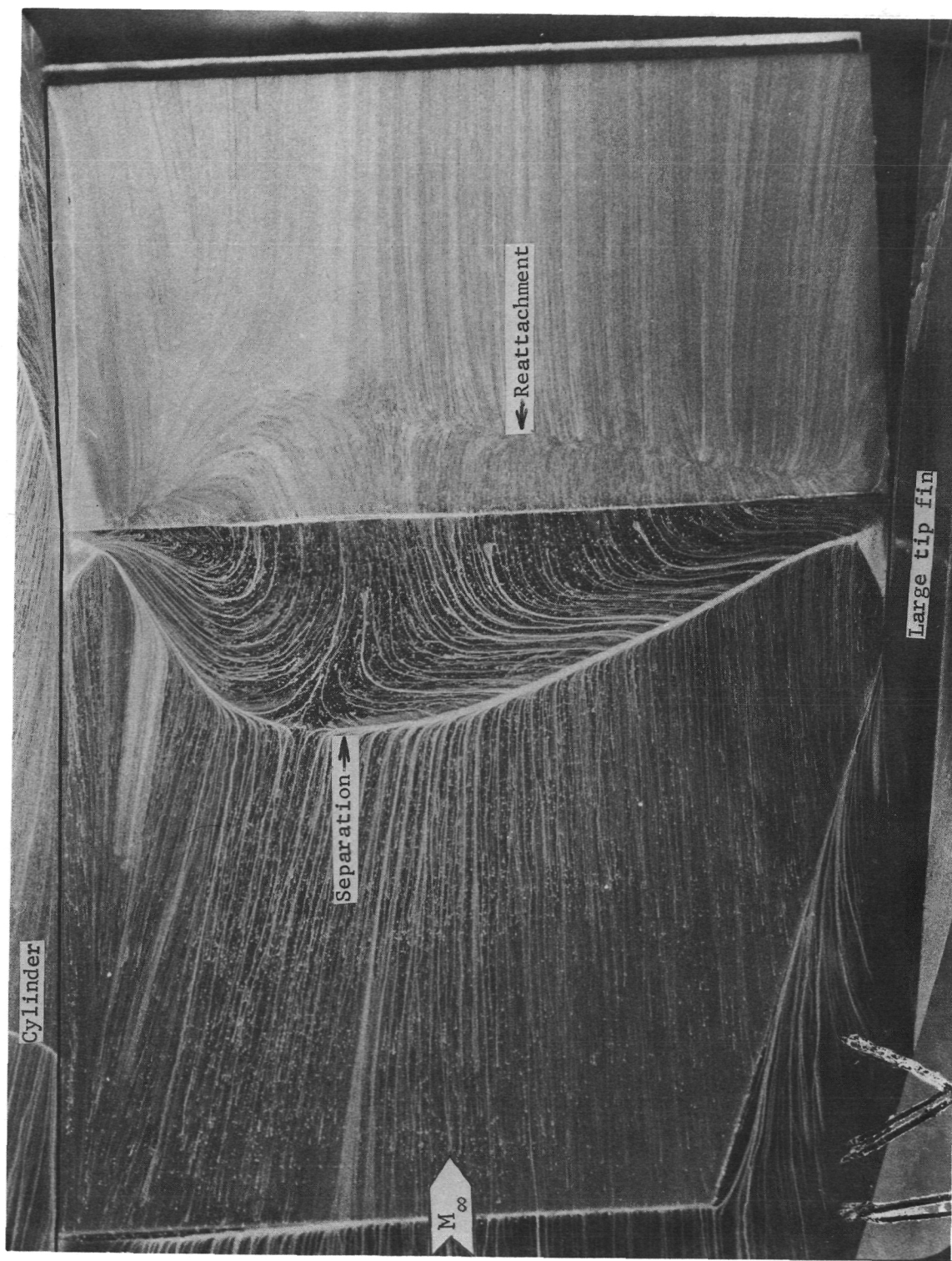


Figure 67.- Frame from planform oil film flow motion picture showing wing and elevon surfaces.
 $\epsilon = 30^\circ$; $\Lambda = 70^\circ$; cylindrical body and large tip fin attached.

L-78-70

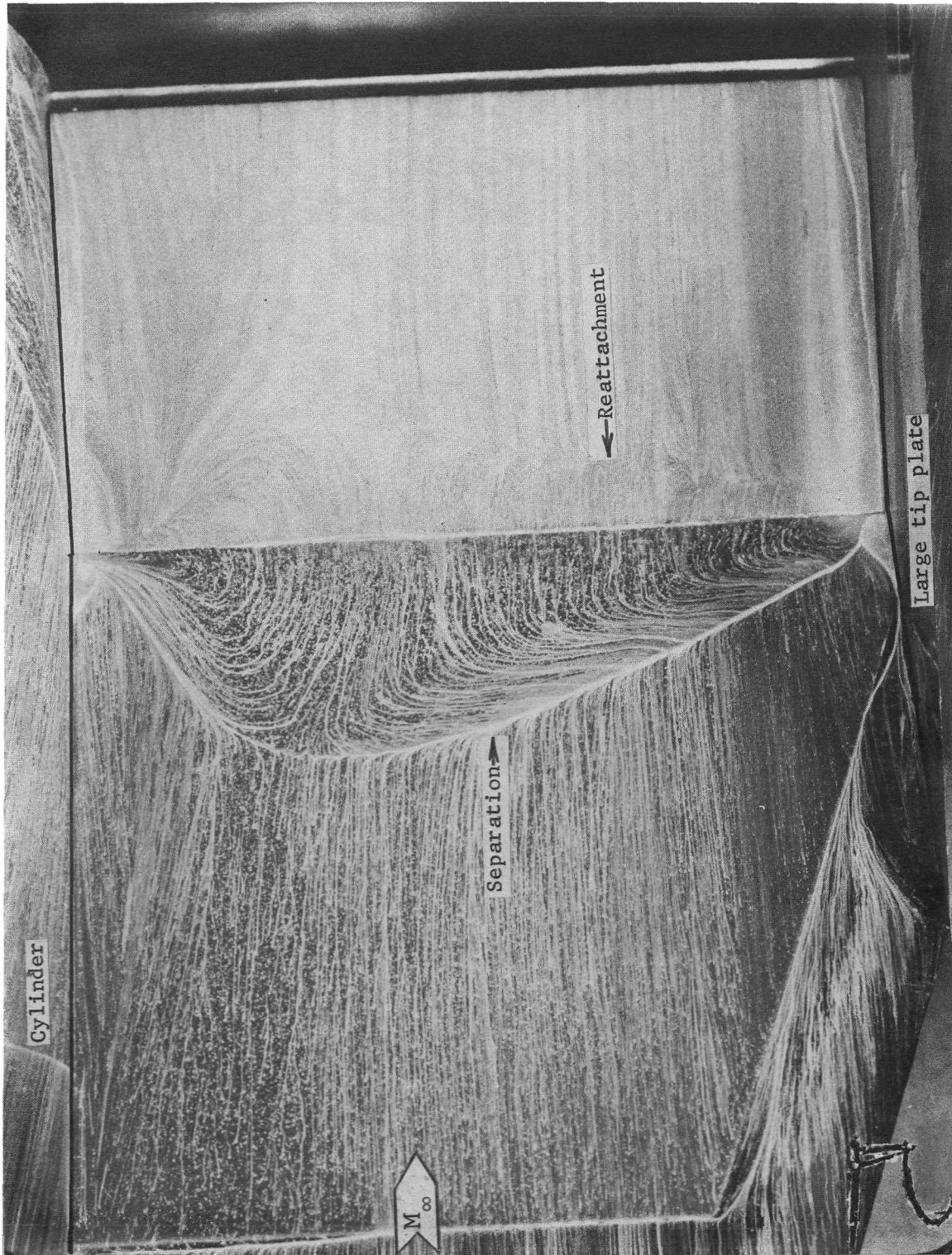


Figure 68.- Frame from planform oil film flow motion picture showing wing and elevon surfaces.
 $\epsilon = 30^\circ$; $\Lambda = 70^\circ$; cylindrical body and large tip plate attached.

L-78-71

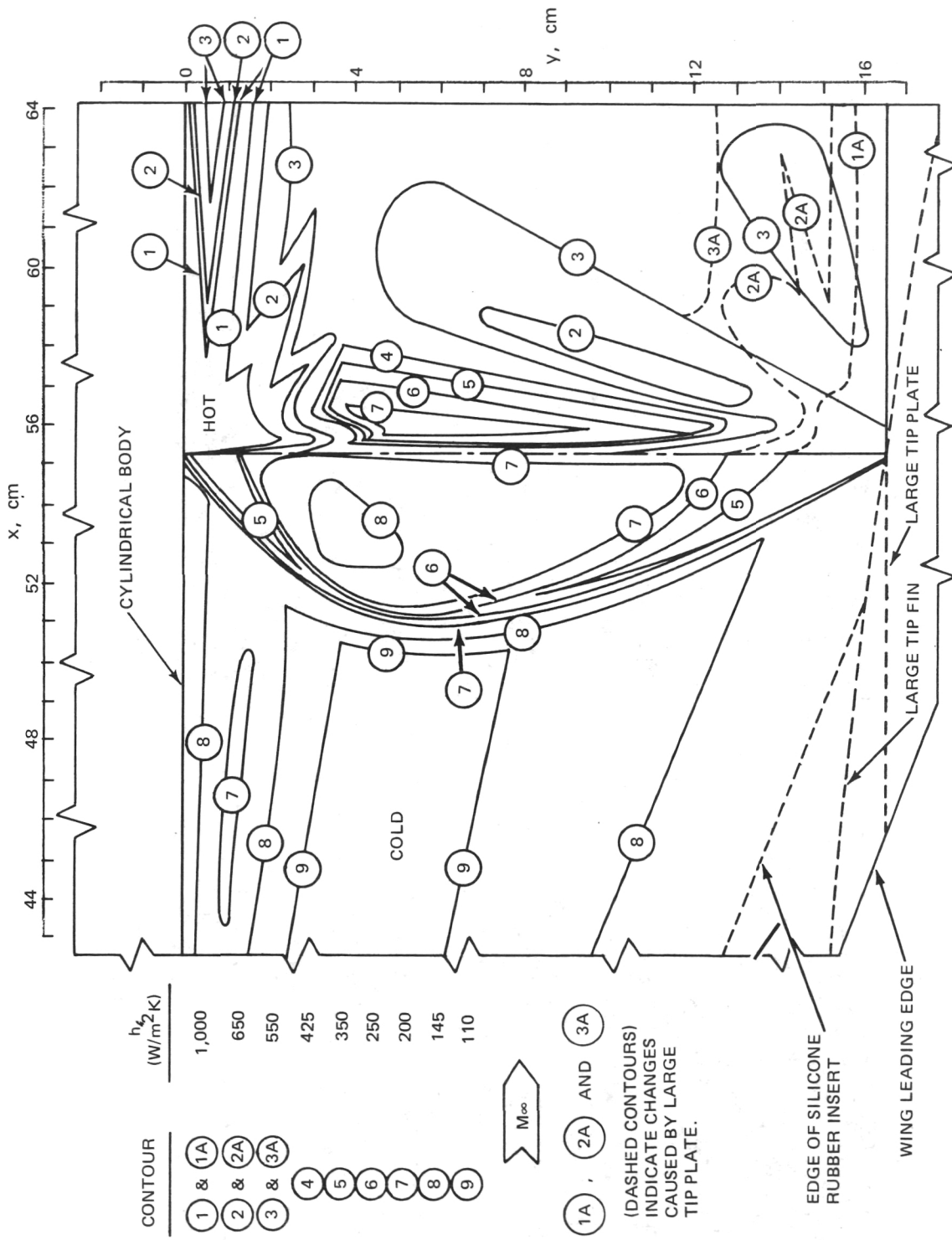


Figure 69.- Constant heat transfer coefficient contours on wing and elevon surfaces. $\epsilon = 30^\circ$; $\Lambda = 70^\circ$; cylindrical body attached. Contours shown for three configurations: with no tip attachment, with large tip plate, or with large tip fin.

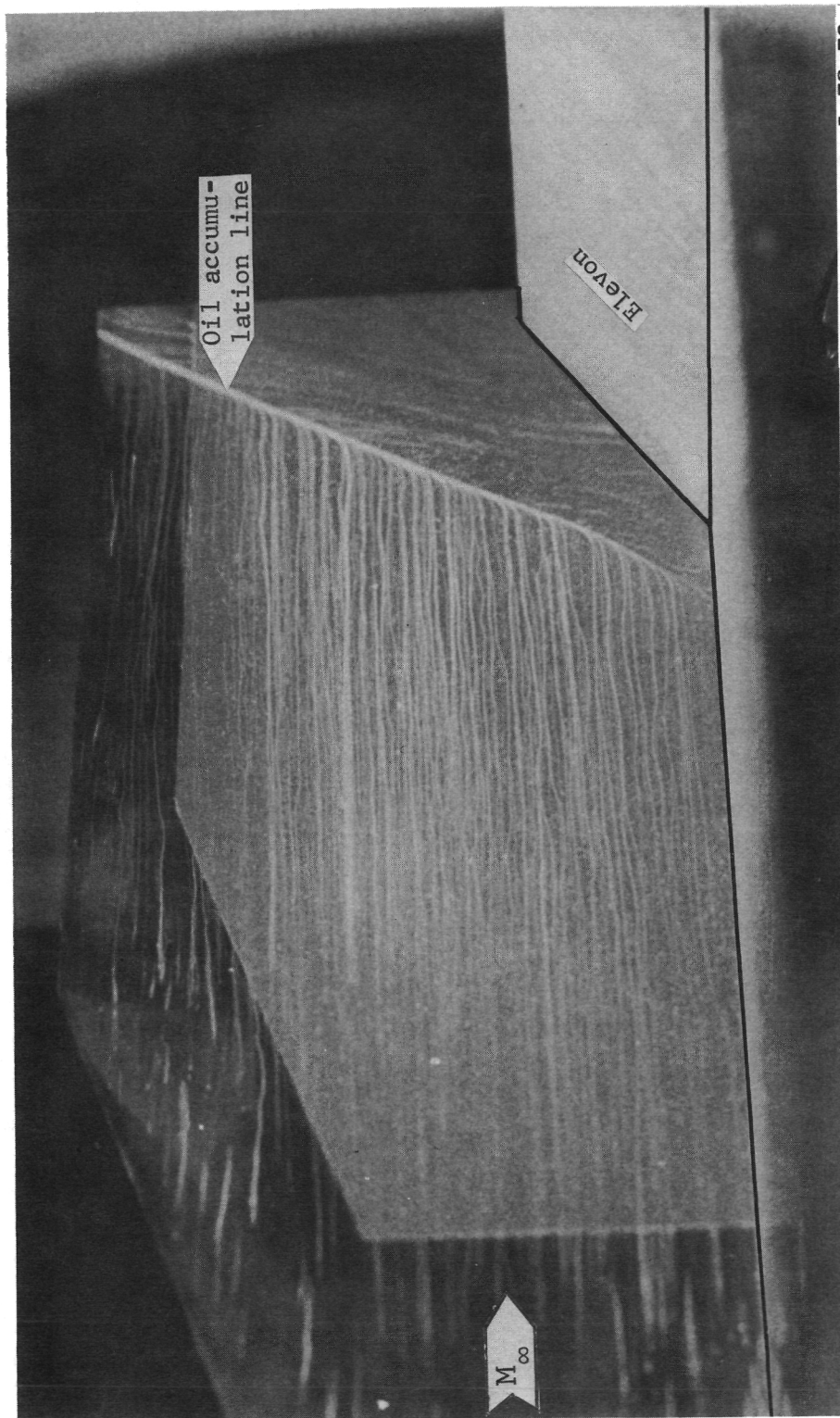
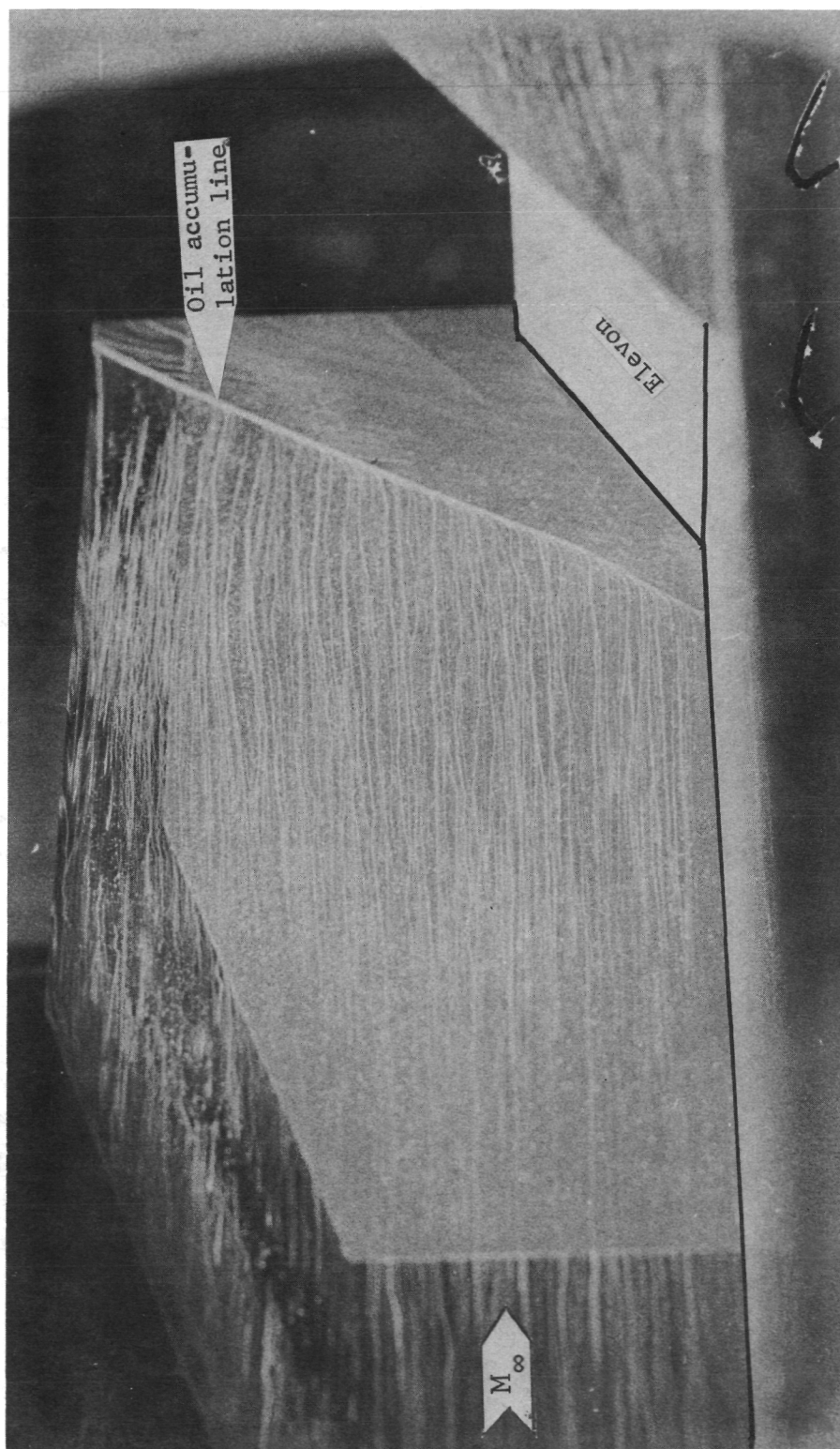


Figure 70.- Frame from profile oil film flow motion picture showing end plate surface.
 $\epsilon = 30^\circ$ and $\Lambda = 0^\circ$.
 L-78-72



L-78-73

Figure 71.- Frame from profile oil film flow motion picture showing end plate surface.
 $\epsilon = 30^\circ$; $\lambda = 0^\circ$; large tip plate attached.

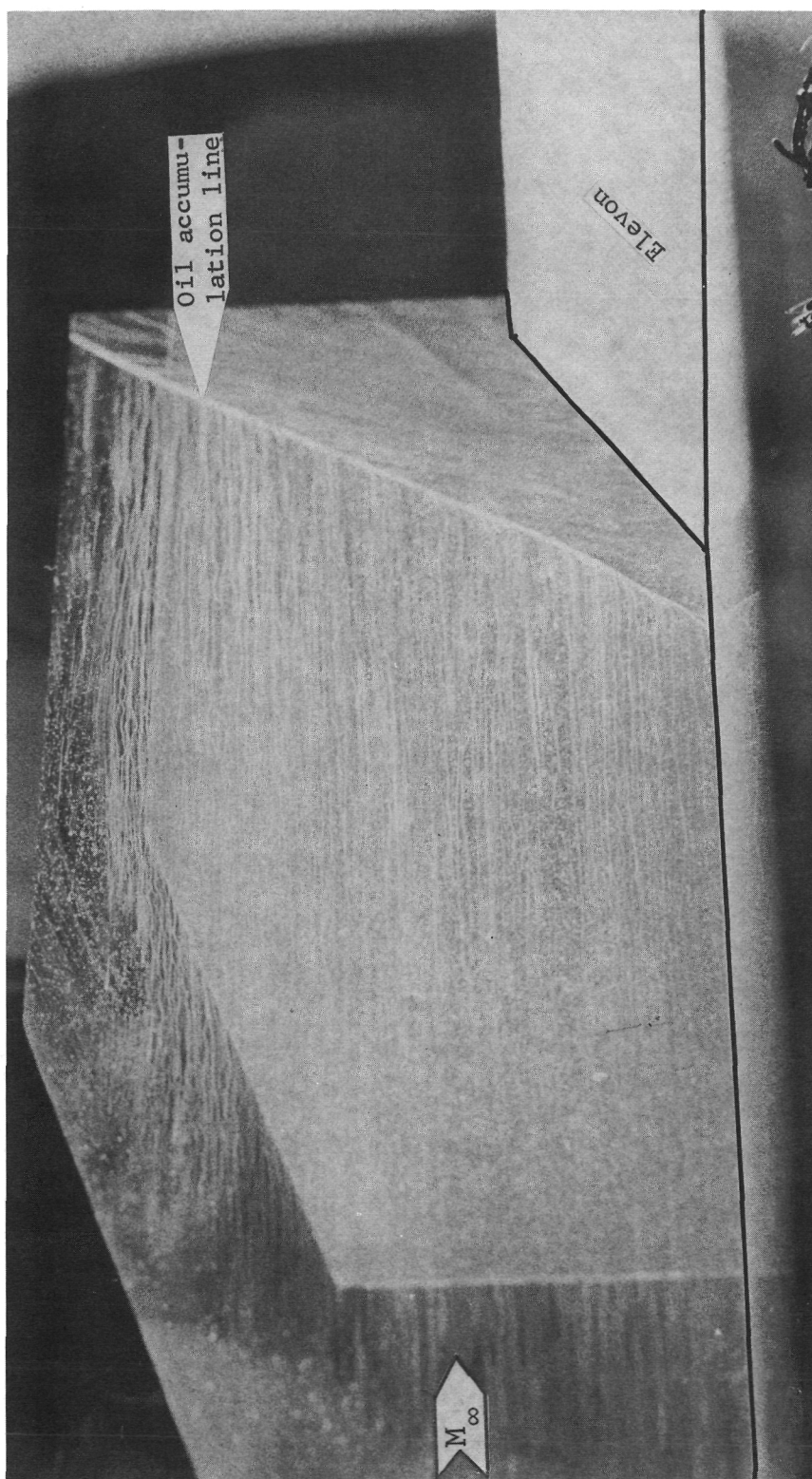


Figure 72.- Frame from profile oil film flow motion picture showing end plate surface.
 $\varepsilon = 30^\circ$ and $\Lambda = 50^\circ$.

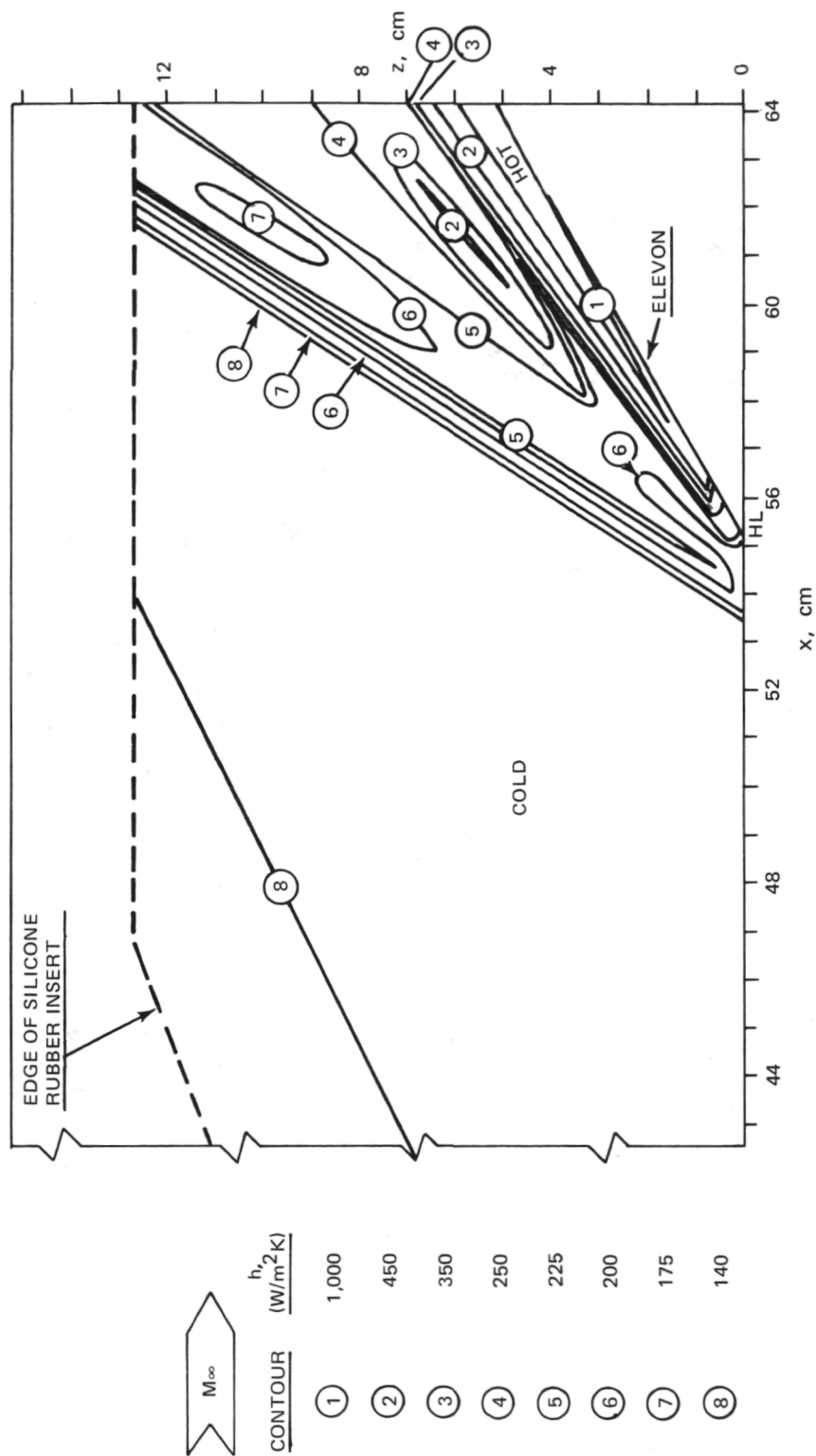


Figure 73.- Constant heat transfer coefficient contours on end plate surface. $\epsilon = 30^\circ$. Contours shown for five configurations: $\Lambda = 0^\circ$ with and without large tip plate, $\Lambda = 50^\circ$ without large tip plate, and $\Lambda = 70^\circ$ with and without large tip plate.

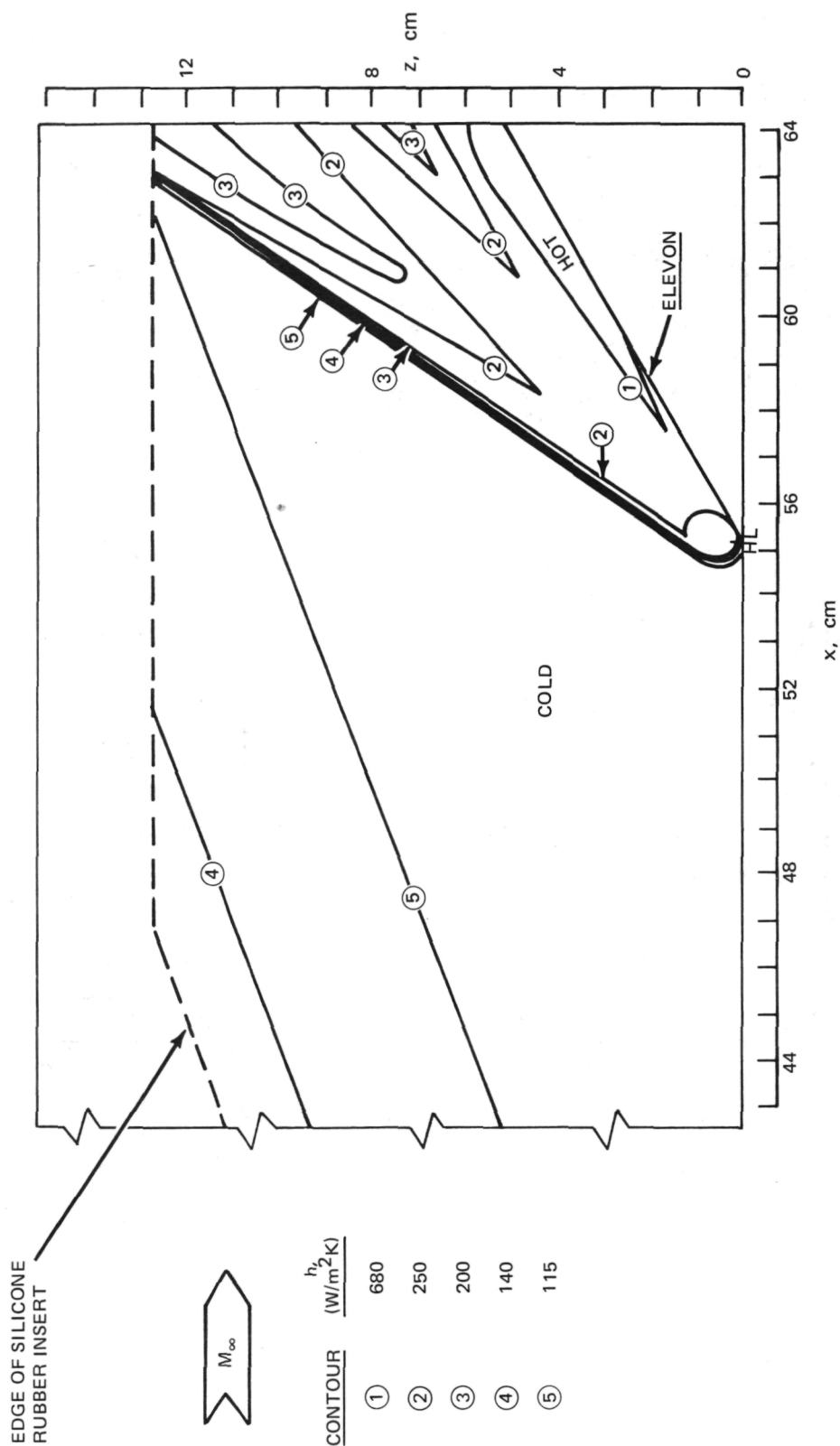


Figure 74.- Constant heat transfer coefficient contours on end plate surface. $\epsilon = 30^\circ$; 0.32-cm gap between end plate and elevon. Contours shown for two configurations: $\Lambda = 0^\circ$ with no tip attachment and $\Lambda = 70^\circ$ with large tip plate.

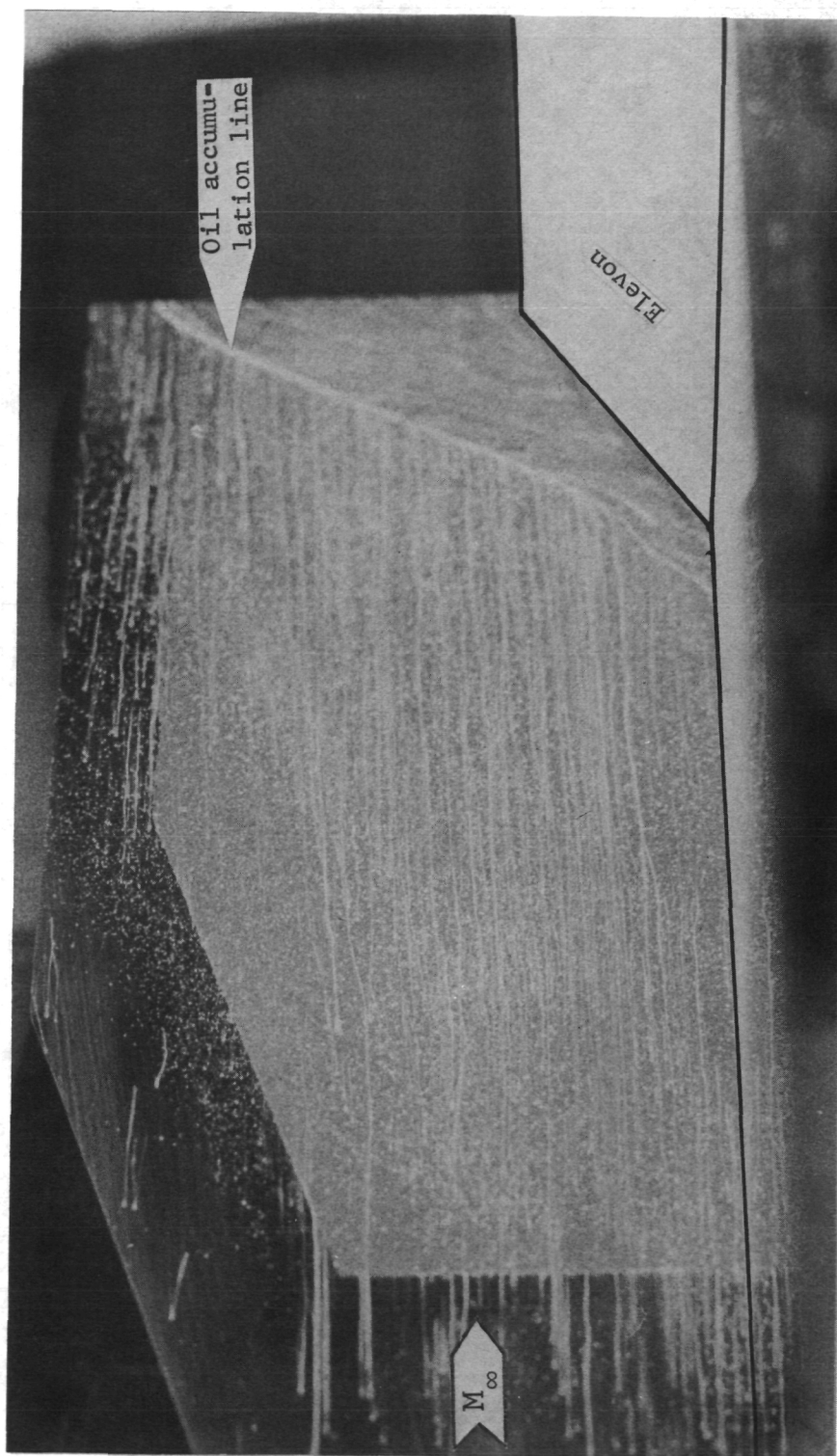
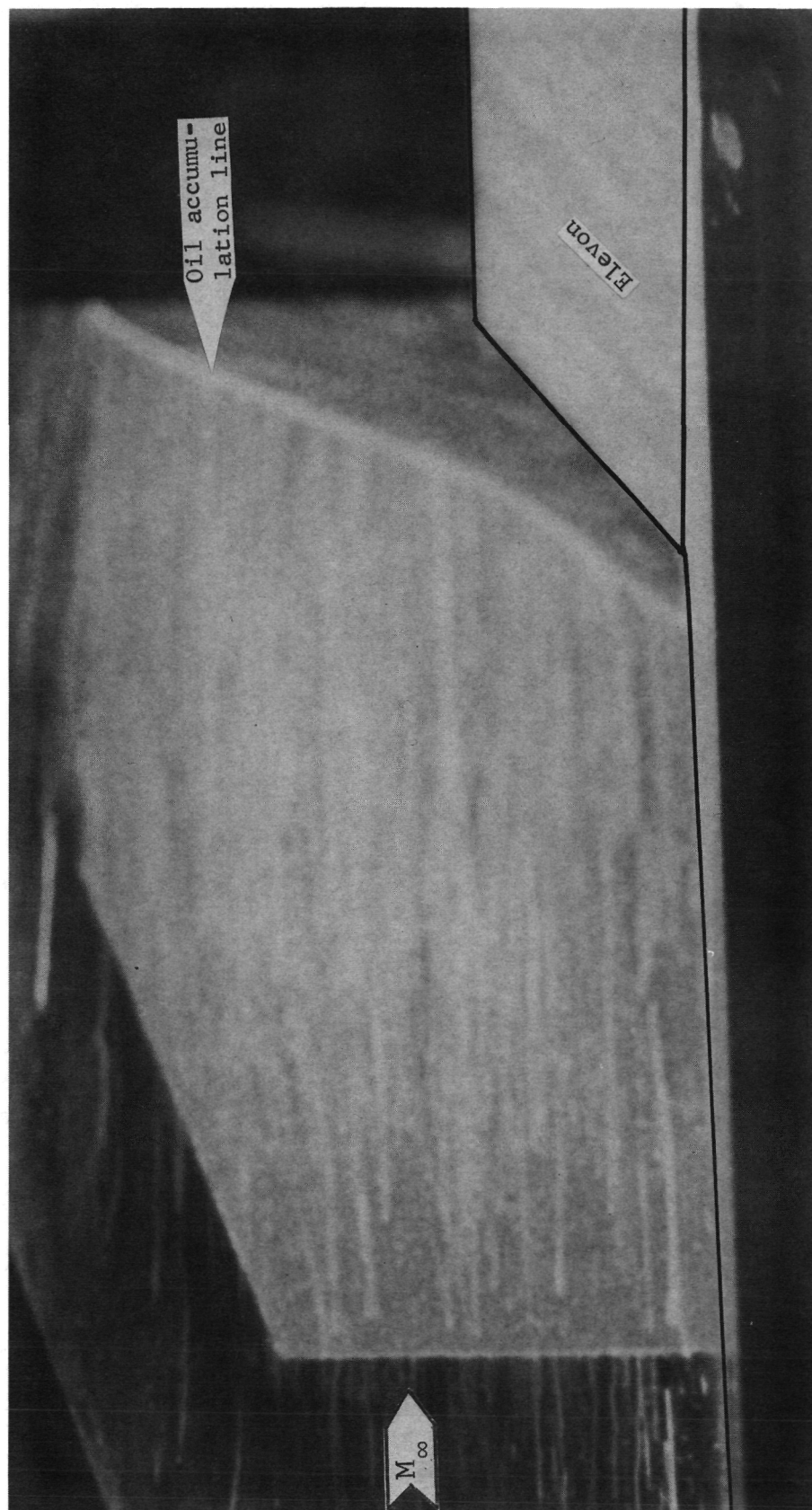


Figure 75.- Frame from profile oil film flow motion picture showing end plate surface.
 $\epsilon = 30^\circ$; $\Lambda = 0^\circ$; 0.64-cm gap between end plate and elevon.

L-78-75



L-78-76

Figure 76.- Frame from profile oil film flow motion picture showing end plate surface.
 $\epsilon = 30^\circ$; $\Lambda = 70^\circ$; 0.64-cm gap between end plate and elevon.

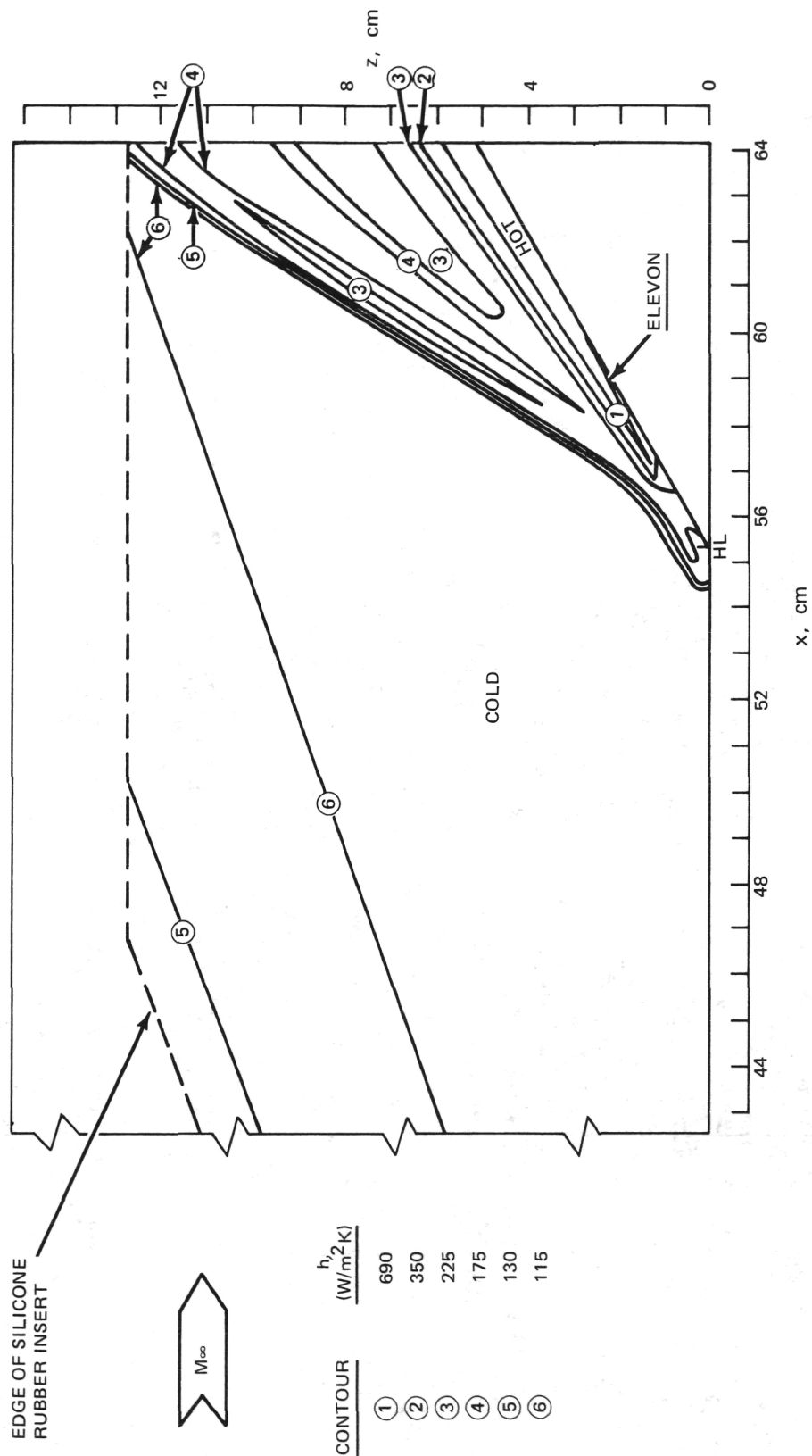


Figure 77.- Constant heat transfer coefficient contours on end plate surface. $\varepsilon = 30^\circ$; 0.64-cm gap between end plate and elevon. Contours shown for three configurations: $\Lambda = 0^\circ$ with no tip attachment and $\Lambda = 70^\circ$ with and without large tip plate.

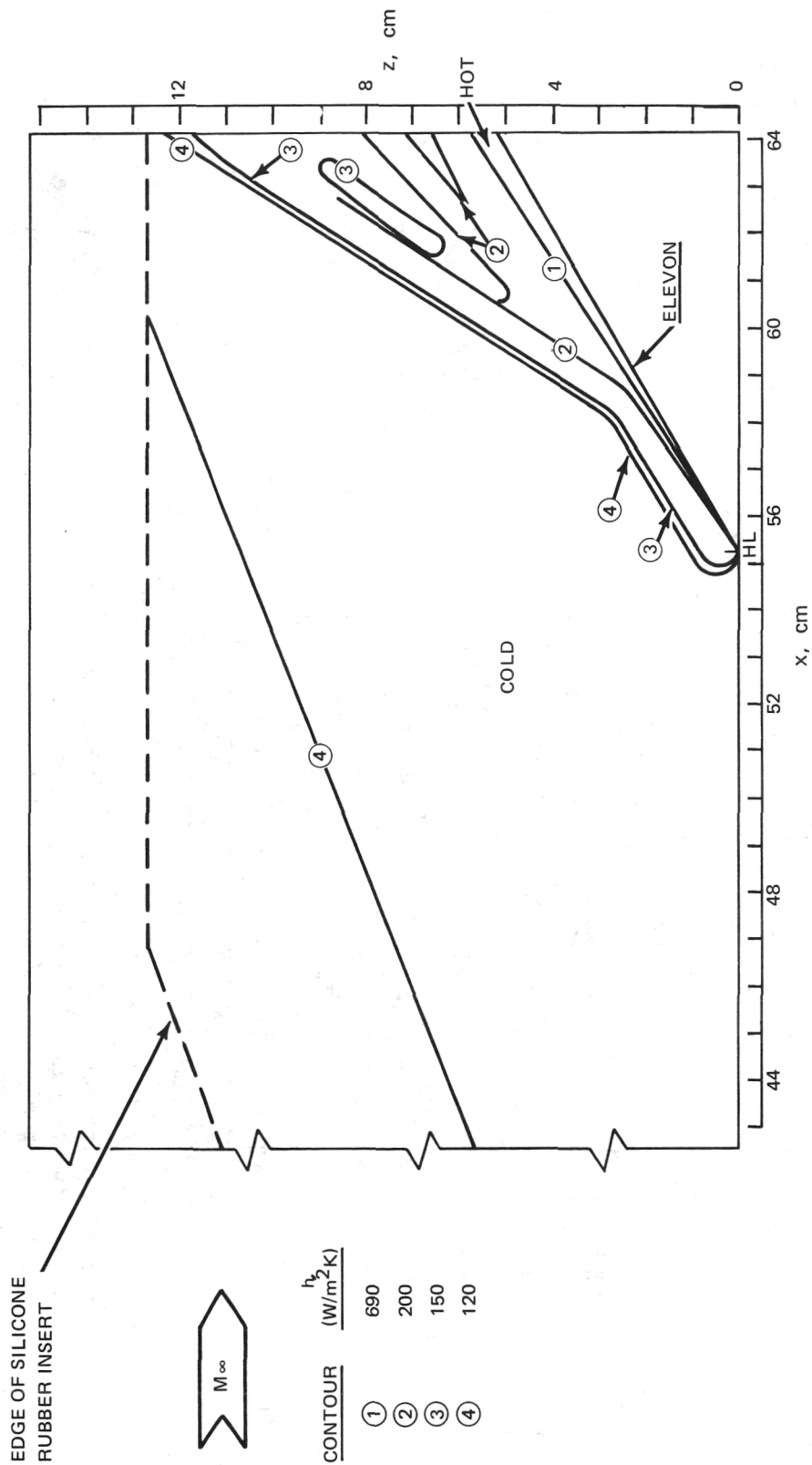


Figure 78.- Constant heat transfer coefficient contours on end plate surface. $\epsilon = 30^\circ$; 0.95-cm gap between end plate and elevon. Contours shown for two configurations: $\Lambda = 0^\circ$ with no tip attachment and $\Lambda = 70^\circ$ with large tip plate.

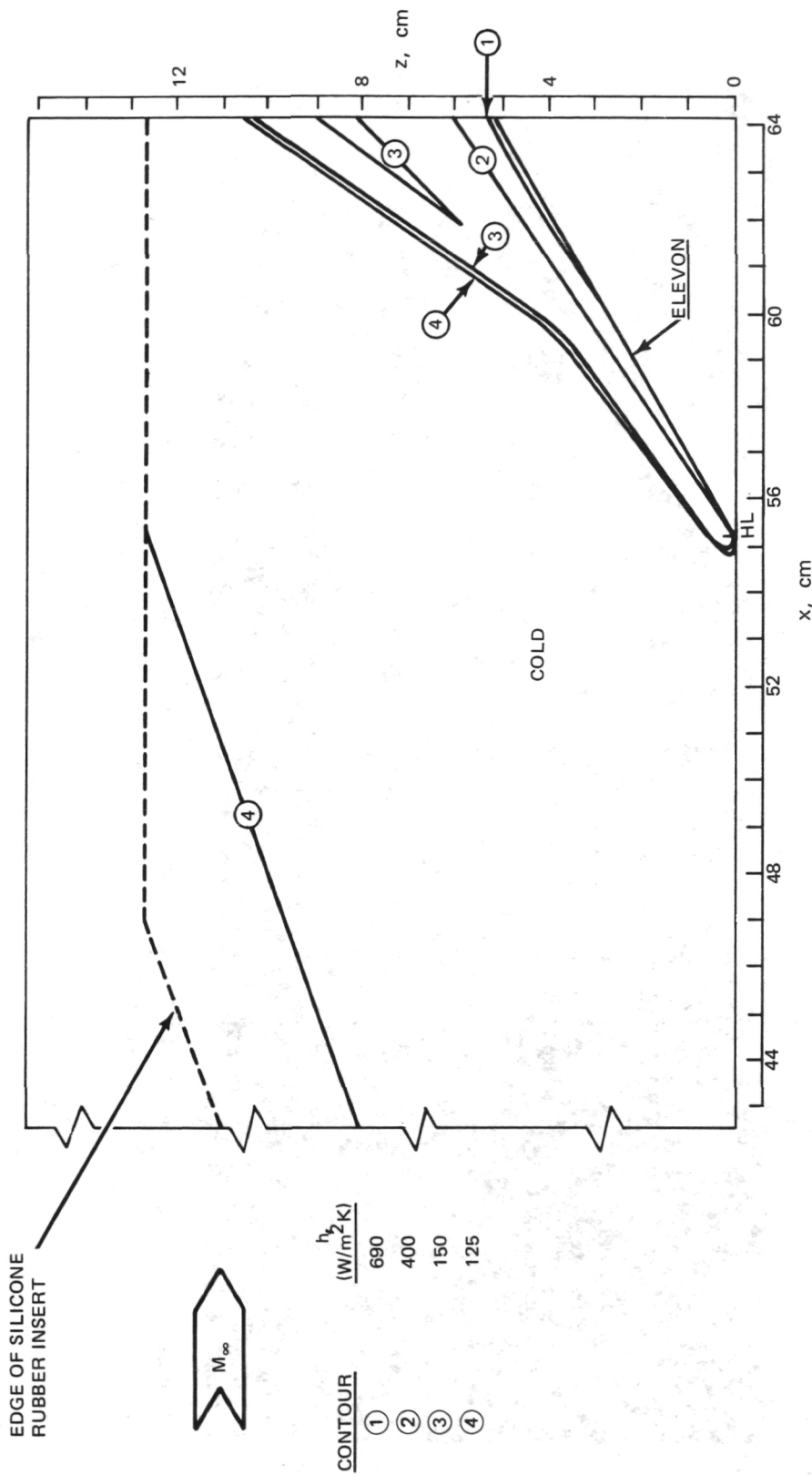
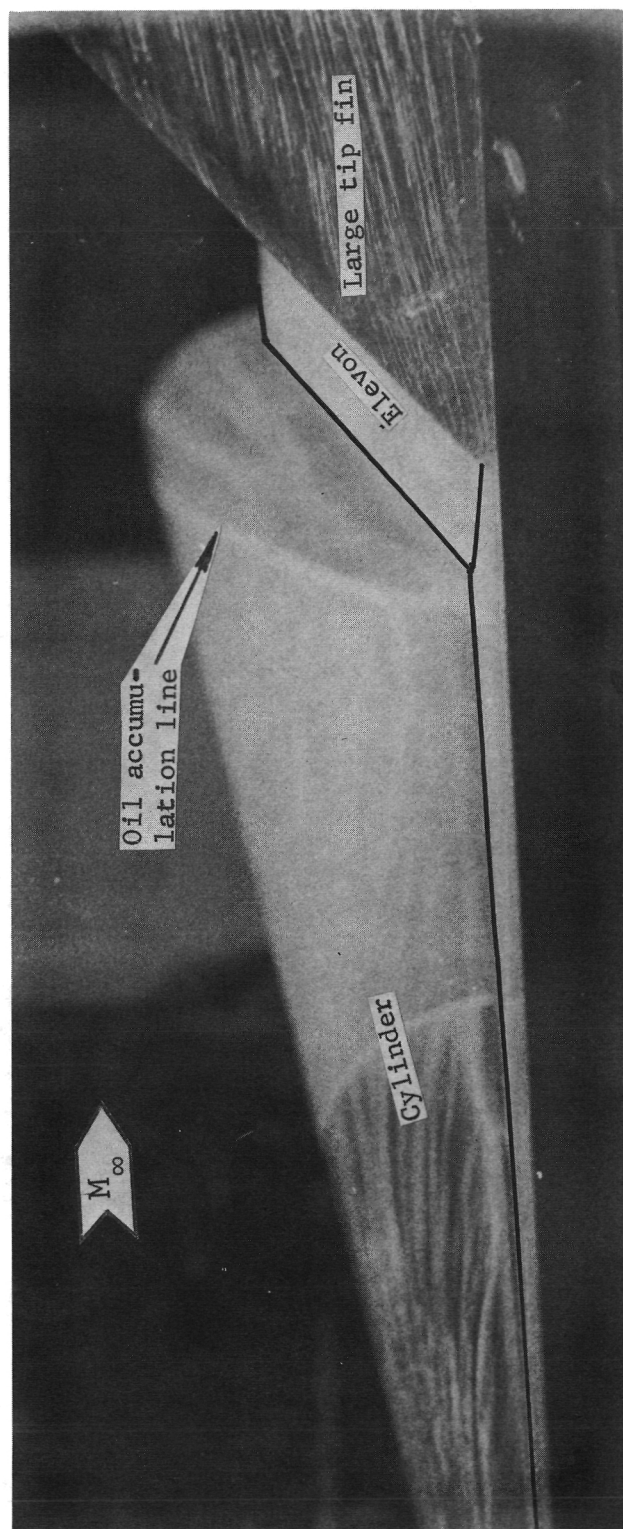


Figure 79.- Constant heat transfer coefficient contours on end plate surface.
 $\varepsilon = 30^\circ$; 1.27-cm gap between end plate and elevon. Contours shown for
 two configurations: $\Lambda = 0^\circ$ with no tip attachment and $\Lambda = 70^\circ$ with large
 tip plate.



L-78-77

Figure 80.- Frame from profile oil film flow motion picture showing cylindrical body surface.
 $\epsilon = 30^\circ$; $\Lambda = 70^\circ$; large tip fin attached.

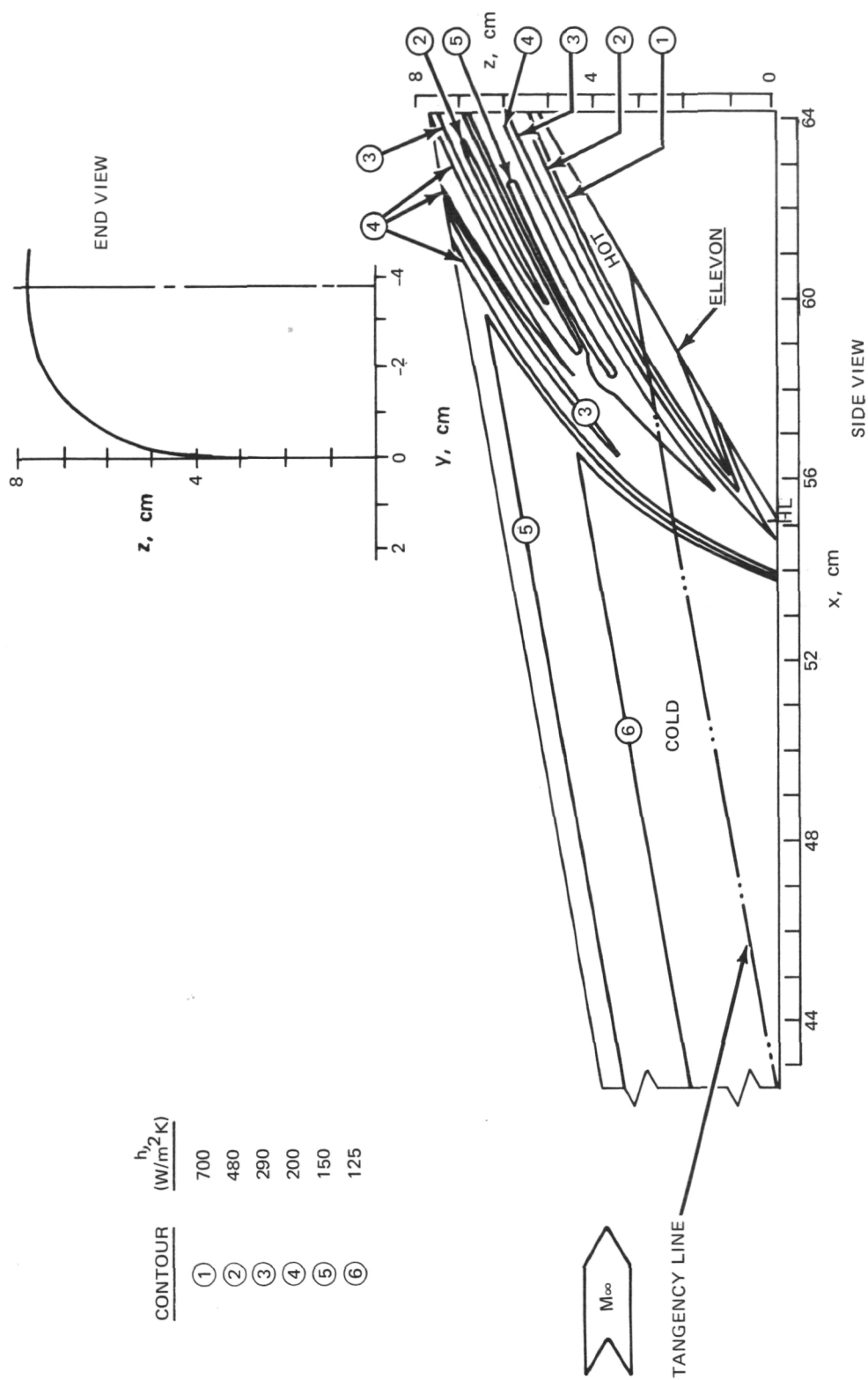


Figure 81.- Constant heat transfer coefficient contours on cylindrical body surface. $\epsilon = 30^\circ$ and $\lambda = 70^\circ$. Contours shown for three configurations: with no tip attachment, with large tip plate, or with large tip fin.

1. Report No. NASA TM-74045		2. Government Accession No.		3. Recipient's Catalog No.	
4. Title and Subtitle HEAT TRANSFER DISTRIBUTIONS INDUCED BY ELEVON DEFLECTIONS ON SWEEP WINGS AND ADJACENT SURFACES AT MACH 6				5. Report Date August 1978	
				6. Performing Organization Code	
7. Author(s) Charles B. Johnson and Louis G. Kaufman II				8. Performing Organization Report No. L-11461	
9. Performing Organization Name and Address NASA Langley Research Center Hampton, VA 23665				10. Work Unit No. 505-11-31-02	
				11. Contract or Grant No.	
12. Sponsoring Agency Name and Address National Aeronautics and Space Administration Washington, DC 20546				13. Type of Report and Period Covered Technical Memorandum	
				14. Army Project No.	
15. Supplementary Notes Charles B. Johnson: Langley Research Center, Hampton, Virginia. Louis G. Kaufman II: Grumman Aerospace Corporation, Bethpage, New York.					
16. Abstract Surface heat transfer distributions are presented for swept wing semispan models having trailing-edge elevon ramp angles of 0°, 10°, 20°, and 30°. The wing sweepback angles are 0°, 50°, and 70°. The models have attachable cylindrical and flat-plate center bodies and various attachable wing-tip fins. The data, obtained for a 0° angle of attack, a free-stream Mach number of 6, and a wing root chord Reynolds number of about 17×10^6 , reveal considerably larger regions of elevon-induced thermal loads on adjacent surfaces than would be suggested by fully attached flow analyses.					
17. Key Words (Suggested by Author(s)) Heat transfer Turbulent boundary layer Hypersonic flow Viscid-inviscid action Flow separation				18. Distribution Statement Unclassified - Unlimited Subject Category 34	
19. Security Classif. (of this report) Unclassified	20. Security Classif. (of this page) Unclassified	21. No. of Pages 103	22. Price* \$6.50		

National Aeronautics and
Space Administration

THIRD-CLASS BULK RATE

Postage and Fees Paid
National Aeronautics and
Space Administration
NASA-451



Washington, D.C.
20546

Official Business

Penalty for Private Use, \$300

13 2 10, D, 070778 S90844HU
MCDONNELL DOUGLAS CORP
ATTN: PUBLICATIONS GROUP PR 15246-A
P O BOX 516
ST LOUIS MO 63166

NASA

POSTMASTER:

If Undeliverable (Section 158
Postal Manual) Do Not Return

30 NOV1978B

J. E. Britt E242/106/ES/2846/

MAR

11 00 25 AUG 1978